Spiral Galaxies in Cosmological Zoom-Simulations

Adrian Bittner
Munich 2018

Spiral Galaxies in Cosmological Zoom-Simulations

Master Thesis

at the

Ludwig Maximilians University Munich

University Observatory Munich

submitted by

Adrian Bittner

born on February 15, 1994 in Kronach

supervised by
PD Dr. Klaus Dolag

and

Prof. Dr. Andreas Burkert, Dr. Rhea-Silvia Remus

Munich, March 09, 2018

Spiralgalaxien in Kosmologischen Zoom-Simulationen

Masterarbeit

an der

Ludwig Maximilians Universität München

Universitätssternwarte München

eingereicht von

Adrian Bittner

geboren am 15. Februar 1994 in Kronach

betreut von
PD Dr. Klaus Dolag

and

Prof. Dr. Andreas Burkert, Dr. Rhea-Silvia Remus

München, 09. März 2018

We feel that this stands as a symbol
of the insatiable curiosity of all mankind to
explore the unknown.

- Dr. Buzz Aldrin
  aboard Apollo 11, July 24th, 1969

Contents

Abstract

Cosmological Zoom-Simulations have proven to be a invaluable tool to study structures on all scales, from superclusters down to large elliptical galaxies. With this study, we aim at resimulating Milky-Way-like disc galaxies and thereby to finalize an existing set of Zoom-Simulations which then spans a range in mass from 10^{11} to $10^{15}\,\mathrm{M_\odot}$. To this end, we use a $1\,\mathrm{Gpc\,h^{-1}}$ sized cosmological box which allows to choose objects from a variety of cosmological ecosystems. For this purpose, significant improvements of the simulation setup are necessary. We revisit implementations of black hole merger processes, adapt the merger conditions, and conclude that black holes need to merge onto the black hole which resides deeper in the potential to assure the remnant black hole stays within the galaxy. A comprehensive parameter study of the AGN feedback model shows that best results are obtained if the feedback acts only on hot gas, regardless of the accretion mode of the AGN. Runs without AGN feedback do not result in realistic disc galaxies. Our final production runs yield galaxies which follow the relevant scaling relations. I emphasize the notably thin galactic discs and various morphological features in the galaxies, such as bars and spiral arms of different classes. The developed simulation setup allows diverse subsequent studies, which will benefit from even higher resolutions that are now feasible. Finally, I present the results of an observational study on spiral structure in disc galaxies and review the main features of an IFU data analysis pipeline, to complement the numerical investigations.

1. Introduction

1.1. Observations

Historical Overview   The first observations of "spiral nebulae" have been made in 1850 by Lord Rosse (Rosse, 1850, see also Fig. 1.1). He already observed first point sources in these spiral nebulae, indicating that these objects do not only consist of gas.

However, is was not clear if these nebulae are of galactic or extragalactic origin. This discussion peaked in the "Great Debate" of Curtis-Shapley in 1920, before this puzzle was solved by Hubble. He first measured the distances to M31 and M33 and confirmed that these objects are too far away to be located inside the Milky Way (Hubble, 1926a, 1929). This way he clarified that the observed objects are actually distinct galaxies and "spiral nebulae" became spiral galaxies (see also Dobbs and Baba, 2014).

Figure 1.1.: Sketch of the grand-design spiral galaxy M51 as observed by Rosse (1850) (Image taken from Dobbs and Baba (2014)).

The Hubble Sequence   Nowadays, we do not only know spiral galaxies, but a variety of different galaxy types with various morphologies which can all be arranged in the well known Hubble sequence (Hubble, 1926b, 1927). A modern version of the Hubble sequence, as advanced by other authors, is displayed in Fig. 1.2.
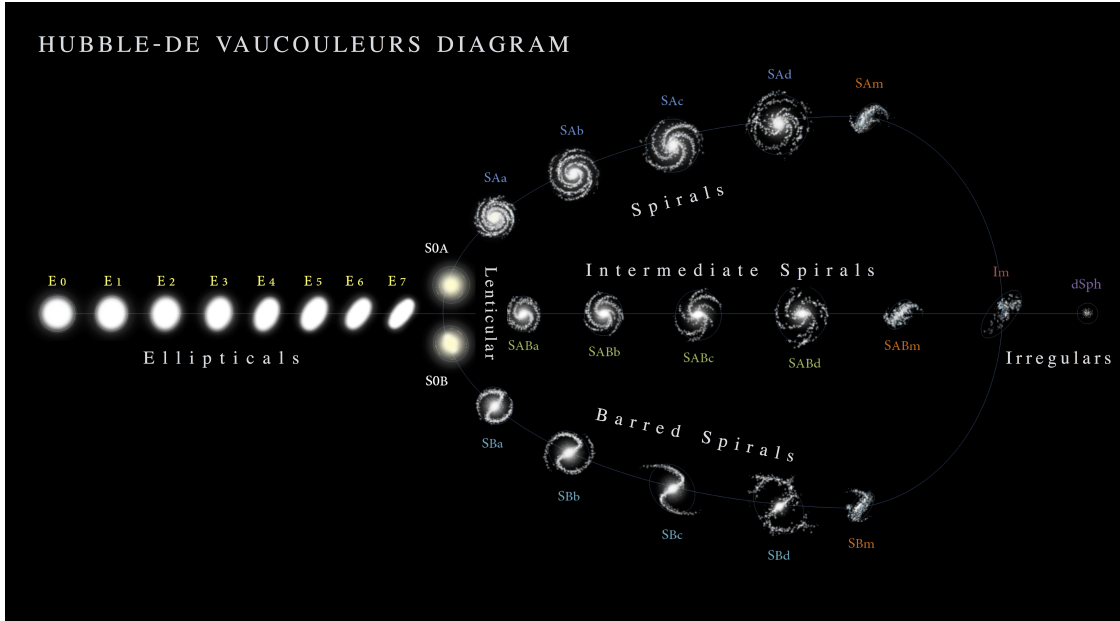
Figure 1.2.: Modern visualization of the Hubble-de Vaucouleurs Sequence (Image taken from `https://en.wikipedia.org/wiki/File:Hubble-Vaucouleurs.png`).

The original Hubble Sequence, as introduced by Hubble (1926b) does distinguish between elliptical, spiral and irregular galaxies. Elliptical galaxies, also referred to as early-type galaxies, are dynamically hot systems. In other words, these objects are mainly stabilized against gravitation by the velocity dispersion of their stars. In fact, elliptical galaxies do mostly consist of old stars while only little gas and barely ongoing star formation are observed. In the Hubble Sequence early-type galaxies are arranged according to their ellipticity $\epsilon = (a - b)/a$, with the semi-major axis a and the semi-minor axis b. By omitting the decimal place in the ellipticity, elliptical galaxies can be denoted E0 for circular shaped galaxies, up to E7 for strongly elliptical objects.

The second main galaxy type classified in the original Hubble Sequence is spiral galaxies, also denoted as late-type galaxies. These objects are dynamically cold and mainly supported by rotation. In contrast to elliptical galaxies, spiral galaxies contain a significant number of young stars, gas and usually show substantial ongoing star formation. Most disc galaxies are composed of a central spheroidal bulge, a gaseous and stellar disc, a bar and spiral arms. However, I note that not all disc galaxies contain these structural components and that these components themselves can show fundamental differences in their properties and formation histories. Spiral galaxies are arranged along the sequence according to their visual appearance: Galaxies denoted Sa have tighly wound spiral arms and massive bulges, while types Sc show more open spiral structure and faint bulges. The sequence of spirals is further divided into barred (SB) and non-barred (SA) galaxies.

Hubble (1926b) further distinguishes irregular galaxies of which the Magellanic Clouds are the most prominent examples. This class includes all dwarf galaxies and disturbed systems. For the sake of completeness (although not explicitly recognized by Hubble (1926b)), the transition from elliptical to disc galaxies is covered by so

called lenticular galaxies (denoted S0). These objects share properties with spiral galaxies, such as their disc-like structure, but also with ellipticals, for instance the low amount gas and star formation.

As observational methods advanced, this classification scheme was also further refined. For instance, the Comprehensive de Vaucouleurs revised Hubble-Sandage (CVRHS) systems allows the classification of various morphological features, such as lenses, rings and pseudorings, bars, bar ansae and barlenses, box/peanut and X-pattern structures, etc. (see e.g. Buta, 2013; Buta et al., 2015). I further highlight recent advances concerning elliptical galaxies, in particular the discovery of the fast- and slow-rotating subgroups (Emsellem et al., 2007).

Spiral Arm Classes The spiral structure in disc galaxies does show a range of different appearances, varying in their amplitudes, geometrical properties and levels of symmetry. Therefore, disc galaxies can be classified by their spiral arm classes in flocculent, multi-armed and grand-design galaxies (see e.g. Elmegreen et al., 1982; Elmegreen and Elmegreen, 1984; Elmegreen et al., 2011).
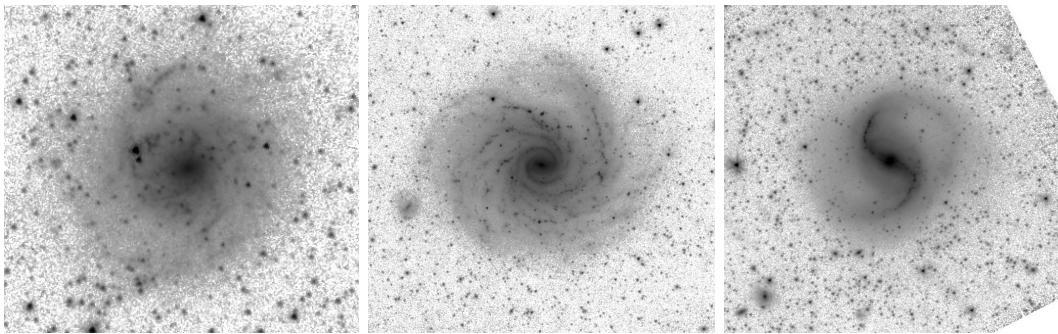
Figure 1.3.: Illustration of the three spiral arm classes: Flocculent (left panel, NGC 5668), multi-armed (central panel, NGC 1232) and grand-design (right panel, NGC 986) galaxies (Sheth et al., 2010).

Flocculent galaxies are characterized by short and patchy spiral arms with a low degree of symmetry (see left panel in Fig. 1.3). Thus, the spiral arms in flocculent galaxies are presumable triggered by local gravitational instabilities and not by a underlying density wave.

In contrast, spiral arms in grand-design galaxies have large amplitudes and show a high level of symmetry on global scales (see right panel in Fig. 1.3). Thus, this spiral structure may be caused by standing spiral density waves (see Lindblad 1959; Lin and Shu 1964; Toomre 1969 for the theoretical framework, Saha and Elmegreen 2016 and Bittner et al. 2017 for recent numerical and observational results).

The third spiral arm class, multi-armed galaxies, share properties with both flocculent and grand-design galaxies (see central panel in Fig. 1.3). In particular, the inner parts of many multi-armed galaxies are two-armed and symmetric whereas the outer parts are more irregular. Thus, multi-armed galaxies have been though to

be an intermediate case, although recent observational results propose multi-armed galaxies to be a variation of grand-designs (Bittner et al., 2017).

For a more detailed review of spiral structure in galaxies, their observational properties and proposed theories see Athanassoula (1984) or Dobbs and Baba (2014).

Internal and External Evolution of Disc Galaxies　Spiral galaxies show substantial evidence for both internal and external evolution. Internal evolution, in the context of galaxies also named secular evolution, is evident in a variety of processes and the resulting changes in the involved structural components. The most illustrative example is the influence of strong bars on their host galaxies. In fact, bars might be able to trigger spiral structure and are known for generating a gas inflow to the central parts of galaxies, this way establishing nuclear rings. But also inner and outer rings are thought to be predominantly triggered by bars. Bars are also responsible for the buildup of pseudo-bulges which may in turn, if the bulge becomes massive enough, destroy the bar.

But also external, cosmological influences are capable of influencing the evolution of a galaxy significantly. This includes common processes such as the accretion of gas or small satellites, triggering of bars or spiral structure by companions, or environmental processes as starvation, harassment and ram pressure stripping. Most importantly, major mergers can easily change the entire morphology of a galaxy and transform a disc to an elliptical.

It is matter of debate in how far the evolution of galaxies, in particular disc galaxies, is governed by secular or cosmological evolution and to what extent this depends on environment and redshift of the objects. In this study we aim at developing a setup of cosmological Zoom-Simulations to pave the way to address these questions by providing sufficiently resolved galaxies which formed self-consistently in a large-scale cosmological environment.

1.2. Numerical Simulations

1.2.1. Technical Aspects

Numerical simulations are a very powerful tool with a large range of applications, not only in physics, chemistry and biology but also in fields like engineering, economics and many more. They are also an invaluable resource in astrophysics with applications on all scales, ranging from planet formation in protostellar discs to the evolution of the large-scale structure in the Universe. When simulations are used to reproduce a large, cosmological environment, two main components need to be implemented: dark and baryonic matter. Due to their distinct physical behaviour, it is advantageous to implement these two components in different ways. Cold dark matter can be treated as a collisionless, perfect, non-relativistic fluid.

This description is justified because the typical collision timescale is longer than the age of the Universe. The same assumption is true for all stars that form later in the simulation. In contrast, baryonic gas is usually modelled as an ideal fluid and therefore the hydrodynamical equations need to be solved. In addition, many advanced physical processes such as gas cooling, star formation and feedback take place in the baryonic component. In the following I present the basic ideas of the implementation of these two components in numerical simulations, as presented by Dolag et al. (2008).

Dark Matter A collisionless fluid can be sampled by a set of individual particles, which should be understood as one possible Monte-Carlo realisation of the mass distribution of the system. Thus, to compute the evolution of dark matter in the Universe, one has to solve a gravitational N-body problem. The most straightforward idea to calculate the gravitational forces between the particles is the direct sum approach. The overall gravitational potential is computed by summing up the individual contributions of all particles,

$$\mathbf{\Phi}(\mathbf{r}) = -G \sum_j \frac{m_j}{(|\mathbf{r} - \mathbf{r_j}|^2 + \varepsilon^2)^{1/2}} \tag{1.1}$$

with the gravitational constant G, the particle mass m_j and position $\mathbf{r}_j$, and the gravitational softening ε. Since this method calculates the exact Newtonian potential, it produces the most accurate results. However, the number of necessary calculations scales with $\propto N^2$, resulting in compareably high computational costs. Thus, it is not suitable to conduct simulations with very large particle numbers, such as e.g. cosmological boxes. As close encounters between particles are unphysical and may cause unreasonably high forces and accelerations, the gravitational force is smoothed at small distances. To this end, the gravitational softening factor ε is introduced which has typical values of 1/20 to 1/50 of the mean inter-particle separation.

The direct sum approach can be implemented more efficiently by grouping distant particles. At large distances, many particles contribute similarly to the overall potential and large-scale forces become more important than the forces from particular substructures. Thus it is feasible to group these particles by making use of a so called tree algorithm. The code then handles these groups as individual massive particles, instead of calculating the force to all particles separately. Thus, the number of operations can be reduced to $\propto N \log N$, at least under optimal conditions. Naturally, the resulting force is only an approximation, but the error can easily be controlled. This is usually done by defining a maximum angular size of the groups, as seen from the particle of interest.

A third possible method is the so called Particle-Mesh method. Instead of directly calculating forces between particles, it treats the force as a field quantity. To do so, the method defines a mesh and determines the density at each mesh point according to the particle positions. Then the Poisson equation is solved in Fourier space and by using Green's method the potential field is computed. Finally, the potential is interpolated to the particle positions and the force applied. The advantage of this

method is its good performance. However, in high density regions a large number of particles can be assigned to a single mesh cell so that high density regions are not properly resolved.

Finally, the tree algorithm and the particle-mesh method can be combined to, e.g., a TreePM method. This procedure splits the potential in a short and long range part. The short range force is calculated by the tree algorithm whereas the long range part is handled by the particle-mesh method. This hybrid design has multiple advantages: It not only preserves the advantages of the tree method and provides a considerable performance improvement, but also strongly increases the accuracy in the long range part.

Baryonic Matter   In contrast to the dark matter component, baryonic matter can be modelled as an ideal fluid and therefore its evolution is governed by the basic hydrodynamical equations, to be specific the Euler equation, continuity equation and the first law of thermodynamics:

$$\frac{\mathrm{d}\mathbf{v}}{\mathrm{d}t} = -\frac{\nabla P}{\rho} - \nabla \Phi \tag{1.2}$$

$$0 = \frac{\mathrm{d}\rho}{\mathrm{d}t} + \rho \nabla \mathbf{v} \tag{1.3}$$

$$\frac{\mathrm{d}u}{\mathrm{d}t} = -\frac{P}{\rho}\nabla \mathbf{v} - \frac{\Lambda(u,\rho)}{\rho}. \tag{1.4}$$

Based on the two formulations of hydrodynamics, there are two main methods to solve these equations numerically.

The Eulerian approach discretises space by introducing a spatially fixed mesh in the simulation volume. The hydrodynamical equations are then solved for each grid point and interpolated to cover the entire volume smoothly. As mentioned before, the downside of grid based methods is the limited resolution in high density regions. However, the adaptive mesh refinement technique avoids this problem as it increases the spatial resolution of the grid where needed (see e.g. Teyssier, 2002).

Following the Lagrangian formulation of hydrodynamics, the so called Smoothed Particle Hydrodynamics (SPH) method discretises the fluid in individual mass elements (see e.g. Monaghan, 1992; Price, 2012). To obtain continuous quantities, a smoothing kernel method averages over the nearest neighbours. Thereupon the hydrodynamical equations can be solved. An important advantage of the SPH method, as compared to grid methods, is the fact that the dynamical range is not constrained by a grid. In high density regions the mean particle separation is smaller and thus the spatial resolution naturally increased. In addition, individual particles can be identified in the simulation at all times and thus be traced. This allows to easily follow the evolution of certain components through cosmic time. Moreover, it is helpful when determining the resimulation volume in cosmological Zoom-simulations (see Sect. 2.2). A weakness of SPH codes lies in the modelling of shock regions. They cannot be reproduced without introducing an (unphysical)

artificial viscosity, in order to prevent SPH-particles from penetrating the shock.

1.2.2. Simulations of disc galaxies

Simulations are an invaluable tool to study structure and evolution of disc galaxies. Up to now, there are two main approaches to simulate galaxies: Self-consistently within cosmological simulations or as artificially constructed, individual galaxies in high-resolution boxes. I review the main advantages and disadvantages of the two approaches below and then introduce the concept of cosmological Zoom-simulations.

Large cosmological simulations are a useful tool to study the evolution of the Universe. It is possible to test different cosmological models and their parameters, and to follow the hierarchical clustering of objects. This includes the large-scale structure, voids and filaments, clusters of galaxies and even individual galaxies. Thus, all galaxies form self-consistently within a realistic cosmological environment. This also includes the influence of this cosmological environment on the evolution of the galaxies themselves. Relevant external processes may include e.g. major or minor mergers, simple tidal interactions as well as quenching and starvation and are expected to significantly influence the fate of disc galaxies. In addition, cosmological boxes contain a large number of galaxies and thus provide a statistically significant sample of galaxy populations in different environments. Nonetheless, the simulations cannot properly resolve individual galaxies and, in particular, their internal structure. However, these internal processes play an important role for structure and evolution of disc galaxies as well.

Thus, in an alternative approach, individual galaxies are simulated in extremely high resolutions what allows a detailed study of their internal structure and the related secular evolution processes. In fact, these simulations helped significantly to investigate secular evolution, including e.g. the formation and evolution of bars, the growth of pseudo-bulges and the development of spiral structure. However, these simulations also have important disadvantages. Firstly, the disc galaxies do not form self-consistently. Instead, they are artificially constructed models which may introduce significant errors, especially since secular evolution processes are susceptible for small disturbances. Secondly, such simulations do not consider the cosmological ecosystem at all. Thus, they can neither reproduce effects that are solely triggered by environmental influences nor quantify the level of dominance of internal or external processes.

To advance numerical studies of disc galaxies, it is inevitable to simulate galaxies in sufficient resolutions to resolve their internal structure and processes while maintaining their cosmological ecosystem and their self-consistent formation therein. As discussed above, cosmological simulations cannot properly resolve small disc galaxies in the necessary resolution. Thus, we make use of so called cosmological Zoom-simulations in order to highly increase the resolution in a certain region of the cosmological box while the large-scale environment is preserved. This tech-

nique allows a substantial increase of resolution, while the computational expenses are kept reasonable. During the last years, Zoom-simulations have been used to study objects such as clusters of galaxies and even large elliptical galaxies. In this study, we attempt to extend the resolvable mass range down to Milky-Way-like disc galaxies and even beyond.

2. Cosmological Zoom-Simulations

Cosmological simulations provide a valuable tool to study large volumes of self-consistent cosmological environments. In particular, the evolution of the large scale structure of the Universe and clusters of galaxies can be studied in great detail. However, to keep computational expenses at a reasonable level, the simulations can only reach moderate spatial and mass resolutions. Thus, individual galaxies, especially those with small masses, can neither be properly resolved nor their internal processes been studied. As discussed in Sect. 1.2.2, there are many advantages of conducting simulations of individual galaxies in sufficiently high resolution to resolve their internal structure, while maintaining their cosmological ecosystem. Thus, we conduct cosmological Zoom-Simulations and resimulate small volumes from a cosmological box in high resolutions.

This chapter is structured in the following way: In Sect. 2.1 I describe the parent simulation and the selection of suitable resimulation targets. Section 2.2 illustrates the setup of Zoom-Simulations, including the generation of Zoomed-Initial-Conditions and the conducted resimulation runs.

2.1. Sample Selection

The objective of this project is to resimulate Milky-Way-like disc galaxies in sufficient resolution to resolve their structure and internal evolution while maintaining the cosmological environment. Thus, it is necessary to identify halos in the parent simulation which are presumably disc galaxies.

2.1.1. Parent Simulation

The parent simulation of this study is the cosmological box DIANOGA. This dark matter only simulation was conducted with the TreeSPH code GADGET-3, a subsequent version of GADGET-2 (see Springel et al., 2001; Springel, 2005). The box has a comoving size of $L_{Box} = 1\,\mathrm{Gpc\,h^{-1}}$, a total number of $N_{Box} = 1024^3$ particles and a dark matter mass resolution of $m_{\mathrm{DM}} = 6.2 \times 10^{10}\,\mathrm{M_\odot\,h^{-1}}$. The simulation makes use of a Λ cold dark matter (ΛCDM) cosmological model. The corresponding parameters are presented in Table 2.1.

Name	Symbol	Value
Dark energy density parameter	Ω_Λ	0.76
Matter density parameter	Ω_m	0.24
Baryon density parameter	Ω_b	0.04
RMS matter fluctuation	σ_8	0.8
Spectral power-law index	n_s	0.96
Hubble parameter	h	0.72
Hubble constant	H_0	$100\,h\,\mathrm{km\,s^{-1}\,Mpc^{-1}}$

Table 2.1.: Overview of the cosmological parameters of the ΛCDM model used in the simulations.

2.1.2. Halo Selection

In order to find a Milky-Way-like galaxy within the parent simulation, we consider galaxies in a mass range of $0.93 - 1.00 \times 10^{12}\,\mathrm{M_\odot\,h^{-1}}$ which is similar to an observed Milky Way mass of $1.26 \pm 0.24 \times 10^{12}\,\mathrm{M_\odot}$ (McMillan, 2011). Because of the comparably large size of the parent simulation, it samples a large portion of the observable Universe. This implies that the cosmological box contains large scale structures, e.g. filaments, clusters of galaxies but also voids which may not be sampled by smaller boxes. The availability of low density regions has two main advantages for this project. Firstly, the probability of violent interactions between galaxies, like major mergers, is significantly lower in voids. Thus, selecting halos from low density regions increases the likelihood to find a disc galaxy. In addition, secular evolution processes are expected to play a more dominant role in these cosmological environments. Secondly, it is cheaper to resimulate galaxies in voids since the resimulation volume is presumably smaller for isolated objects as compared to objects in dense environments. Therefore it is not only possible to save computational expenses, but also to increase the number of resimulated galaxies.

To identify halos in the parent simulation, I use the halo-finder SUBFIND, which applies the friends-of-friends algorithm to detect virialized particle groups in the simulation. It further applies a density constraint to find locally overdense regions and identify the saddle point of the density field as border of the substructure. Moreover, a gravitational unbinding procedure is applied to recover the self-bound part of the structure (see Dolag et al., 2009, for a more detailed description).

For the detection of isolated halos I adapt the technique of Schlachtberger (2014). For every halo within the selected mass range I calculate the distance, d_{Cluster}, to the next massive object with $M > 1 \times 10^{13}\,\mathrm{M_\odot\,h^{-1}}$ as well as the distance to the next neighbour, $d_{\mathrm{Neighbour}}$. To account for comparably massive neighbours with a strong influence on their environment, $d_{\mathrm{Neighbour}}$ is renormalized with respect to the virial radii of the halo of interest, R_{vir}, and the neighbouring halo, $R_{\mathrm{vir,Neighbour}}$, so that

$$d_{\mathrm{eff}} = d_{\mathrm{Neigbour}} / \left(R_{\mathrm{vir}} + R_{\mathrm{vir,Neighbour}} \right). \qquad (2.1)$$

Figure 2.1 displays the distance to the next massive object, d_{Cluster}, as a function
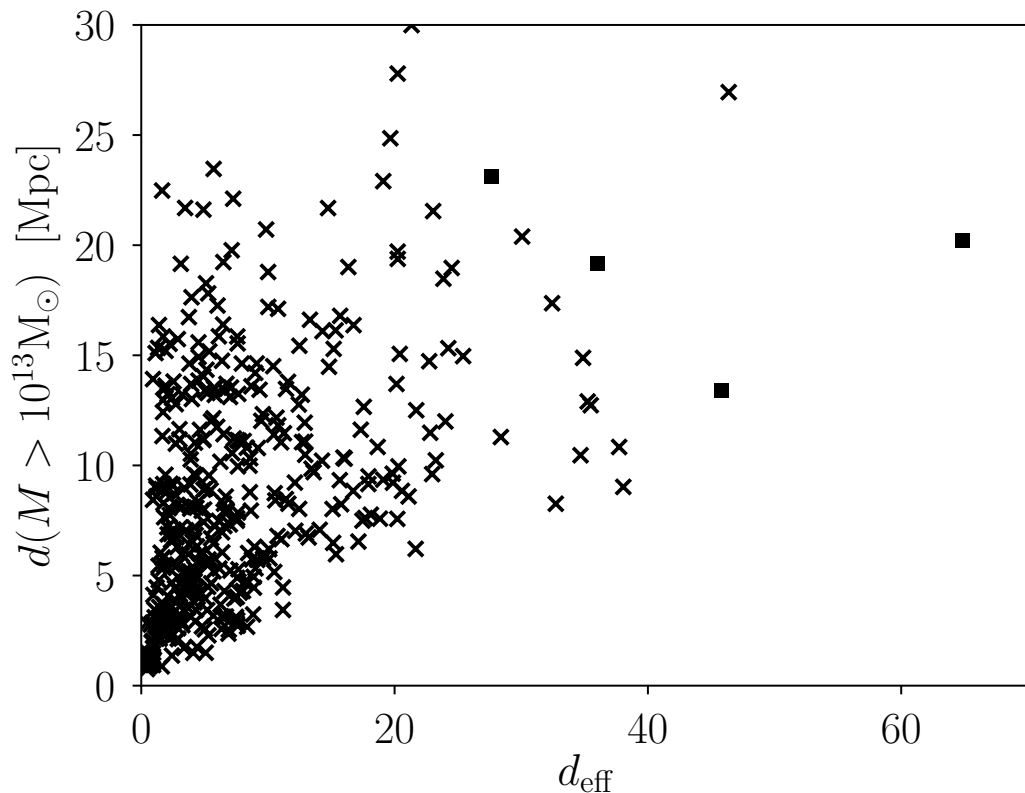
Figure 2.1.: Cluster distance, d_{Cluster}, as a function of the effective distance, d_{eff} for halos within the selected mass range. Selected halos are marked with squares.

of the distance to the next neighbour, d_{eff}. The environments of objects with high values of d_{Cluster} and d_{eff} are inspected visually, in order to select the most promising candidates. In fact, high values of the effective distance seem to be a more significant indicator of isolated galaxies than high values of the cluster distance. The visual inspections are done by plotting orthogonal projections of the environment within spheres of radius $20\,\mathrm{Mpc}\,\mathrm{h}^{-1}$ around the halo of interest (see Fig. 2.2). The halo of interest is marked with a diamond while the corresponding circle displays 20 times the virial radius. Other objects are displayed by circles with their virial radius. In the lower right panel radii scale with the virial mass of the halos in such a way that a radius of $1\,\mathrm{Mpc}\,\mathrm{h}^{-1}$ corresponds to a mass of $1 \times 10^{13}\,\mathrm{M}_{\odot}\,\mathrm{h}^{-1}$. Based on these plots, I conclude that the selected objects are sufficiently isolated to consider them for resimulation.

In addition, Fig. 2.3 displays a radial density profile of the object SIN out to radii above $5\,\mathrm{Mpc}$. The dashed horizontal line marks a mean density in the cosmological box of $\overline{\varrho} \simeq 32.7\,\mathrm{M}_{\odot}/\mathrm{kpc}^{3}$. The high central density of the selected halo is clearly visible at small radii. However, at large radii the density becomes similar to the average density of the Universe, or even falls slightly below this mean density. This indicates that the selection criteria assure that the selected halos are located in a low or average density environment.
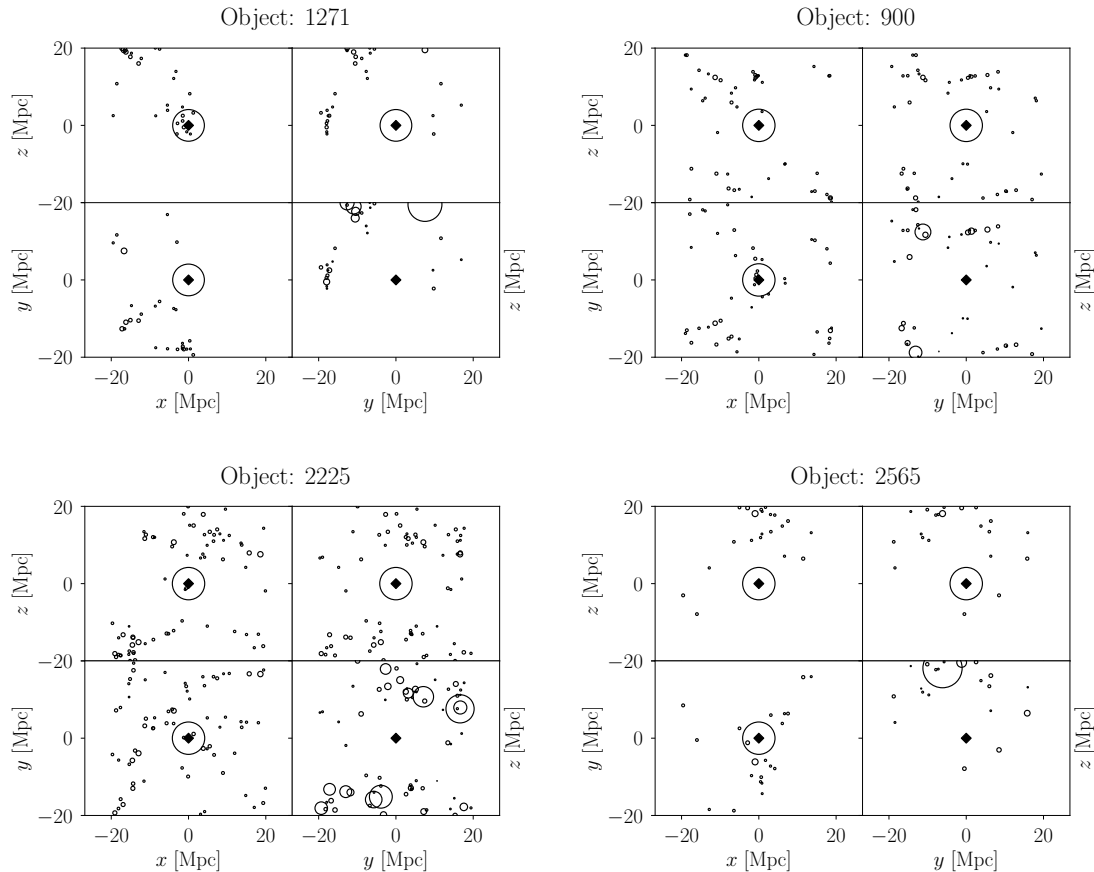
Figure 2.2.: Orthogonal projections of the close environment of the selected halos. The halo of interest is marked with a diamond while the corresponding circle displays 20 times the virial radius. In the lower right panel, radii scale with the virial mass of the halo so that $1\,\mathrm{Mpc\,h^{-1}}$ corresponds to a virial mass of $1 \times 10^{13}\,\mathrm{M_\odot\,h^{-1}}$.

I emphasize that, due to the low mass resolution in the parent simulation, a typical Milky-Way-mass galaxy consists of only 15 to 16 low resolution dark matter particles. In fact, these galaxies are not resolved at all which makes the selection of objects a very difficult task. In addition, the usage of characterising parameters, such as e.g. the spin parameter λ (Peebles, 1969, 1971) or the b-value (Teklu et al., 2015), is difficult since these parameters are presumably not converged in the low resolution parent simulation. Thus, high resolution runs are essential to detect if the objects are in fact disc galaxies and suitable for this study.

In Table 2.2 I provide an overview of the conducted resimulation runs at the *1x* resolution level. It displays the virial mass M_{vir} and radius R_{vir}, the radius which is cleaned of low resolution particles R_{clean}, the coordinates of the halo in the respective box (x_{coord}, y_{coord}, z_{coord}), as well as the number of high resolution dark matter particles n_{DM} in this run. I highlight that the list provides an overview of the most prominent and presumably most interesting halos in the box. However, as the properties of these objects are not clearly determineable at low resolution levels, objects might have to be added/removed as the simulations are advanced to higher resolutions. In particular, this might be the case for low-mass halos. In the rest of this study we concentrate on the numerical modelling of black hole merger and
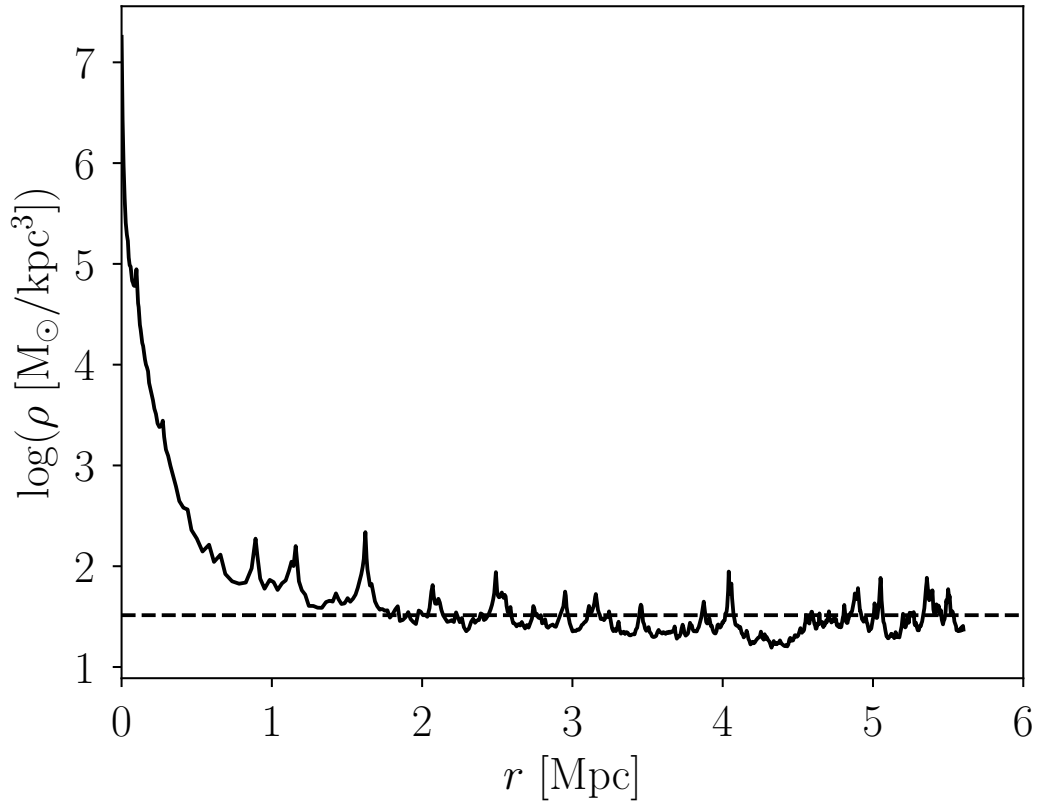
Figure 2.3.: Radial density profile of object SIN out to 5 Mpc. The dashed horizontal line displays the mean density in the cosmological box.

AGN-feedback processes. To this end, all simulation runs in the following chapter are conducted on object SIN. However, I point out that the other halos will be valuable targets for subsequent studies.

Run		M_{vir} $[\,\mathrm{M}_\odot\,\mathrm{h}^{-1}]$	R_{vir} $[\,\mathrm{kpc}\,\mathrm{h}^{-1}]$	R_{clean} $[\,\mathrm{Mpc}\,\mathrm{h}^{-1}]$	x_{coord} $[\,\mathrm{kpc}\,\mathrm{h}^{-1}]$	y_{coord} $[\,\mathrm{kpc}\,\mathrm{h}^{-1}]$	z_{coord} $[\,\mathrm{kpc}\,\mathrm{h}^{-1}]$	n_{DM}
SIN	a	1.07×10^{12}	214.8	4.57	6327.72	-2111.62	-7575.72	48×10^3
HADAD	a	1.21×10^{12}	224.1	3.85	507.81	2021.56	2666.25	47×10^3
	b	1.02×10^{12}	211.2	3.51	-193.84	2143.94	2137.19	47×10^3
ANU	a	1.78×10^{12}	254.6	4.45	-8792.69	-2261.09	-6284.84	28×10^3
	b	4.99×10^{11}	166.7	3.68	-7505.22	-1214.19	-6121.44	28×10^3
	c	2.19×10^{11}	126.6	2.69	-7351.06	-2827.28	-5351.38	28×10^3
MARDUK	a	1.76×10^{12}	253.6	3.93	-5392.69	-2916.06	-2136.81	38×10^3
	b	8.16×10^{11}	196.3	3.65	-3640.22	-3625.53	-148.97	38×10^3

Table 2.2.: Overview of the conducted resimulation runs and particularly interesting objects at the *1x* resolution level. Displayed are the virial mass M_{vir} and radius R_{vir}, the radius which is cleaned of low resolution particles R_{clean}, the coordinates of the halo in the respective box (x_{coord}, y_{coord}, z_{coord}), as well as the number of high resolution dark matter particles n_{DM}.

2.2. **Zoom-Simulations**
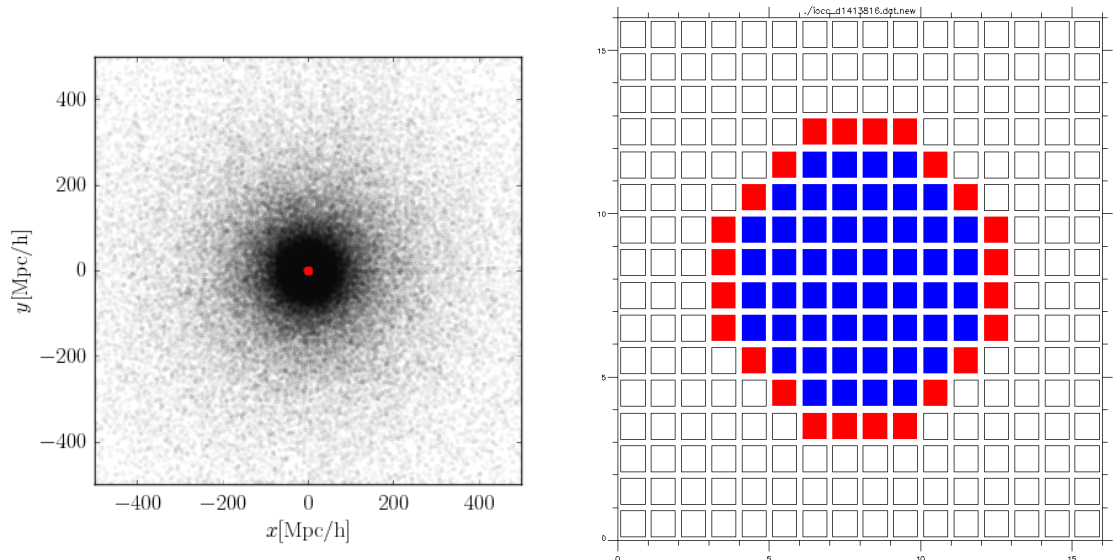
2.2.1. **Zoomed Initial Conditions**

Figure 2.4.: Left: Visualization of the zoomed initial conditions of the entire cosmological box. This box is centred on the high resolution region (red) which is surrounded by a buffer region with the same mass resolution as the original cosmological box. Large scale forces are reproduced by background particles with masses increasing with distance from the high resolution region (black). Right: Visualization of the Lagrangian volume within the high resolution box. Blue cells are occupied by high resolution particles, white cells by low resolution buffer particles, red cells represent a border volume. This box has a size of $15.6\,\mathrm{Mpc}\,\mathrm{h}^{-1}$.

We use the Zoomed Initial Conditions ZIC technique (Tormen et al., 1997) to produce initial conditions with increased mass resolution. The zoomed initial conditions consist of three main parts: A high-resolution region, a buffer region and a low-resolution, background region. Within the high-resolution region, as defined by a Lagrangian volume, the original particles are replaced with a larger number of particles with lower masses, so that the intended resolution level is reached. The new particles are initially put on a regular grid. In order to replicate local tidal forces, the high-resolution region is enclosed by a buffer region which is sampled with the same mass resolution as the parent simulation. In this study we use approximately 1×10^5 buffer particles with $M = 6.2 \times 10^{10}\,\mathrm{M_\odot}\,\mathrm{h}^{-1}$. The density and velocity field on the largest scales is resampled on a spherical grid with a constant angular resolution of $d\theta = 1.5°$. The radial length of each cell $dr = rd\theta$ is chosen in such a way that all cells are approximately cubic. This procedure minimizes the number of required background particles while properly reproducing the large-scale properties of the original cosmological box. With increasing distance from the high-resolution volume, the radial length of the cells increases as well and, thus, the mass of the low-resolution particles. Our Zoom-Simulations include roughly 2×10^6 low-resolution particles with masses ranging from $6.2 \times 10^{10} - 6.8 \times 10^{14}\,\mathrm{M_\odot}\,\mathrm{h}^{-1}$.

Moreover, the overall simulation volume of the parent simulation, $(1\,\mathrm{Gpc}\,\mathrm{h}^{-1})^3$, is adopted for the Zoom-Simulations. This guarantees that the large-scale structure is fully reproduced and that any large structure in the resimulation has a physical counterpart in the original cosmological box (Schlachtberger, 2014).

The high resolution particles occupy an arbitrarily shaped Lagrangian volume in those initial conditions and are embedded in a cubical-shaped box. This cube represents the high resolution box of the resimulation and has a typical size of $1/128 - 1/64\ L_{\mathrm{Box}} = 7.8 - 15.6\,\mathrm{Mpc}\,\mathrm{h}^{-1}$ with L_{Box} being the size of the original cosmological box. Since the Zoomed Initial Condition Generator ZIC requires a minimum box size of $1/64\ L_{\mathrm{Box}}$, all boxes with smaller size are artificially enlarged (see Sect. 2.2.3). Figure 2.4 displays the resulting Lagrangian volume within the resimulation box using a 16^3 grid. Blue cells are occupied by high-resolution particles, white cells by low-resolution particles and red cells represent an additional border volume to the high-resolution region. All resulting high resolution boxes are inspected visually. However, in some cases the volume is not compact or consists of multiple separated parts. It makes no sense to place low-resolution particles within the high-resolution volume, in particular since low-resolution intruders must be avoided. Thus, the volume is edited manually to create a compact high-resolution region whenever necessary (Schlachtberger, 2014).

2.2.2. The Iterative Approach

An overview about the procedure to generate gasified zoomed initial conditions for a halo in a cosmological box is shown in Fig. 2.5. This flowchart displays the main programs (dark grey), relevant input and output files (light grey) and the final initial conditions (blue, lower right). All steps are described in greater detail below.

In the first step, we select all particles in a volume around the halo of interest in the cosmological box. These particles are traced back to their positions in the initial conditions of the original box by using the routine TRACK (see Sect. 2.2.4). Based on this, a high resolution Lagrangian volume is constructed which is then used by the ZIC technique (Tormen et al., 1997) to generate a first guess on the Zoomed Initial Conditions (see Sect. 2.2.1 and 2.2.3). These dark matter only initial conditions are then evolved to redshift zero using GADGET (see Sect. 2.2.5).

However, it is possible that low resolution particles enter the high resolution region. This is problematic, as the low resolution particles represent unphysical potential minima and may trigger the formation of unphysical structures. If this is the case, the Lagrangian volume is manually enlarged to include the contaminating particles in the high resolution volume. The procedure of generating Zoomed Initial Conditions and evolving them to redshift zero is then repeated.

Once the halo at redshift zero is cleaned from low-resolution intruders, one has obtained the final initial conditions for this resolution step. One can now further
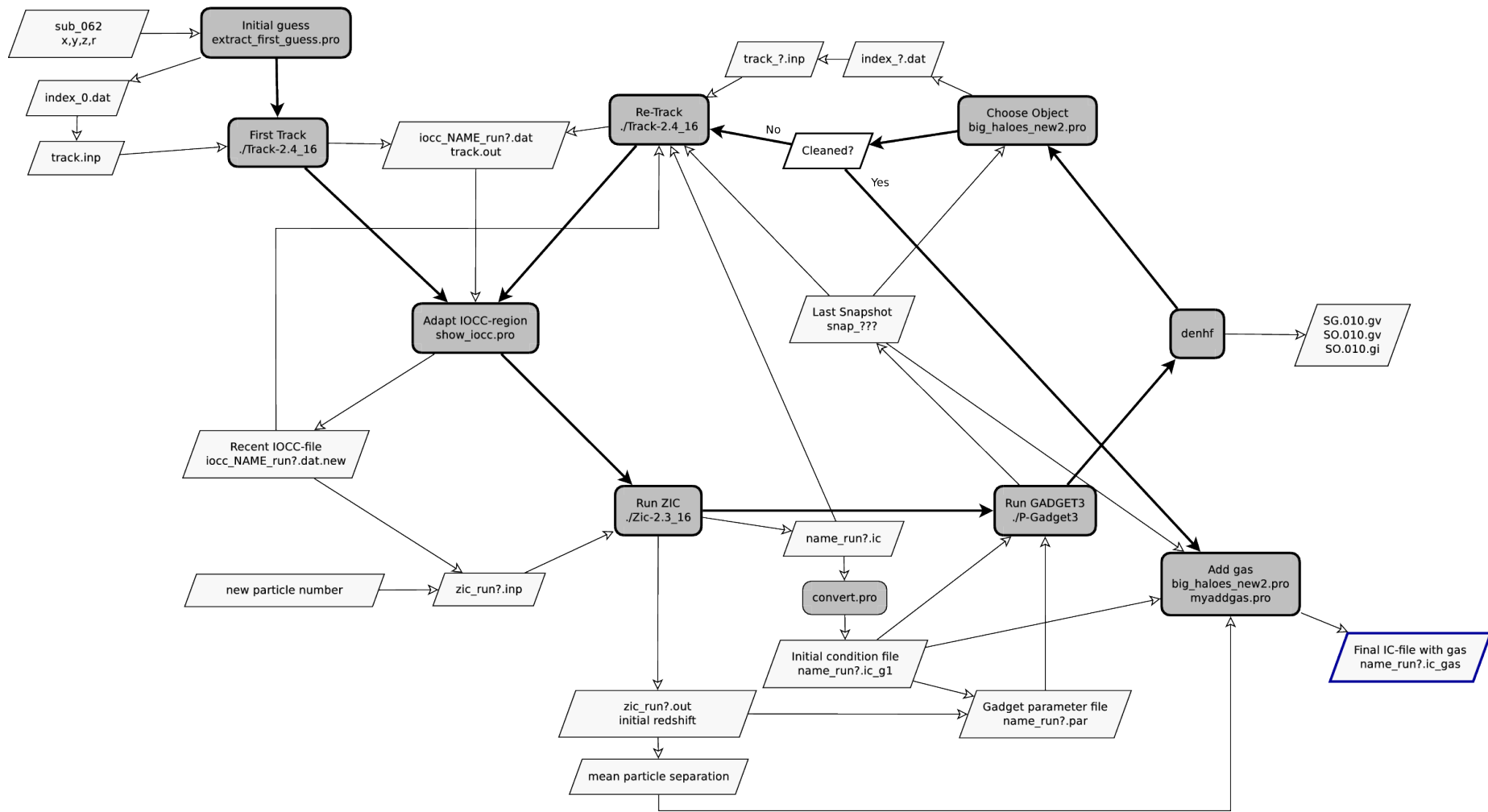
Figure 2.5.: Flowchart of the resimulation procedure, including the main programs (dark grey) as well as the important input and output files (light grey).

increase the resolution and repeat the procedure (see Sect. 2.2.6), or gasify the ICs to conduct a baryonic simulation run (see Sect. 2.2.7).
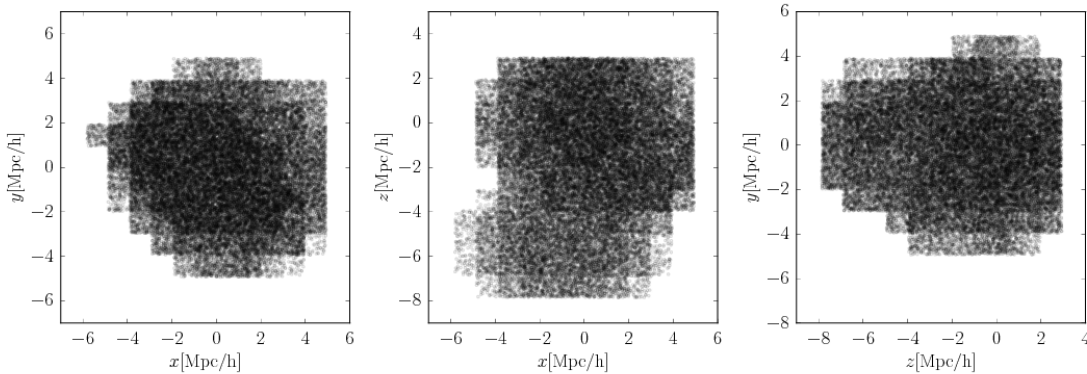
2.2.3. Generation of Zoomed Initial Conditions

Figure 2.6.: Orthogonal projections of high-resolution dark matter particles in the zoomed initial conditions. The plot points out the peculiar shape of the Lagrangian volume due to manual edits to avoid contamination with low-resolution particles.

In order to perturb the high-resolution particles, we make use of the power spectrum of the parent simulation, including its amplitudes and phases. However, the original power spectrum does not sample sufficiently large wavenumbers to resolve the smallest perturbations in the resimulations. Thus, Schlachtberger (2014) reproduced the original power spectrum while extending its range to large wavenumbers. A comparison between the reproduced and original power spectrum did not indicate any significant differences. The finally implemented power spectrum uses the reproduced power spectrum at large wavenumbers while keeping the original version for small wavenumbers. This implementation is chosen to ensure maximum consistency with the parent simulation (Schlachtberger, 2014).

In order to create consistent small scale perturbations in the high-resolution region, the power spectra of the high and low-resolution regions need to be connected. The matching of both power spectra naturally requires that the largest wavelength in the high-resolution region is significantly larger than the smallest wavelength in the low-resolution region. To this end, Tormen et al. (1997) has introduced the constraint

$$\frac{L_{\mathrm{HR}}}{\lambda_{\mathrm{Box,min}}} \geq 4 \qquad (2.2)$$

with the minimum size of the high-resolution box L_{HR} and the smallest wavelength in the parent simulation $\lambda_{\mathrm{Box,min}}$. For latter he chooses

$$\lambda_{\mathrm{Box,min}} = n_{\mathrm{safe}}\lambda_{\mathrm{Box,Ny}} = 2n_{\mathrm{safe}}\Delta_{\mathrm{Box}} \qquad (2.3)$$

with the Nyquist frequency $\lambda_{\mathrm{Box,Ny}}$, a safety factor $n_{\mathrm{safe}} = 2$ and the spatial resolution of the parent simulation Δ_{Box}. With $\Delta_{\mathrm{Box}} = L_{\mathrm{Box}}/1024$ we yield for the minimum size of the of the high-resolution box

$$L_{\mathrm{HR}} \geq 8 n_{\mathrm{safe}} \Delta_{\mathrm{Box}} = 1/64 \, L_{\mathrm{Box}} \simeq 15.6 \, \mathrm{Mpc} \, \mathrm{h}^{-1} \qquad (2.4)$$

For some target objects a box size of $1/128 \, L_{\mathrm{Box}}$ would have been sufficient to encompass the selected galaxy and its environment. However, due to the constraint discussed here, the corresponding high-resolution boxes have been artificially enlarged (Schlachtberger, 2014).

2.2.4. First Guess

For the initial setup of the resimulation, we select all particles within a sphere of radius $3 - 6 \, \mathrm{Mpc} \, \mathrm{h}^{-1}$ around the halo of interest, based on the original cosmological box at redshift zero. The radius of this sphere should be kept as small as possible, in order to reduce the computational expenses of the individual resimulations. Since we attempt to resimulate multiple galaxies at very high mass resolutions, this is needs to be considered carefully. Nonetheless, the radius of the sphere needs to be sufficiently large to avoid contamination of the target halo with low-resolution particles.

We use the routine TRACK (Tormen et al., 1997) to identify the previously selected particles according to their IDs in the initial conditions of the cosmological box DIANOGA. This is then used to generate the zoomed initial conditions with the ZIC technique (Tormen et al., 1997).

2.2.5. Dark Matter Only Runs

Initially, the Zoom-Simulations are conducted as dark matter only runs. Based on the previously generated initial conditions, the simulation is evolved to redshift zero using the code GADGET-3 which is the same code used for the parent simulation.

As mentioned above, it is of vital importance to avoid that low-resolution boundary particles enter the high-resolution region. Due to their higher masses, these would represent spurious potential minima and might trigger the formation of unphysical structures. Thus, we check the simulation for any intruding particles within $7R_{\mathrm{vir}}$ at redshift zero in order to ensure that the galaxy and its direct environment are not influenced. This is illustrated in Fig. 2.7 which shows the output of the routine `big_haloes` for the run SIN in the *250x* resolution level. Displayed are three orthogonal projections of the high resolution region with dark matter particles in black and larger halos marked in red. Blue circles display the cleaned regions around each halo. This figure illustrates that the main halo in the centre of the high resolution region is cleaned out to sufficiently large radii.
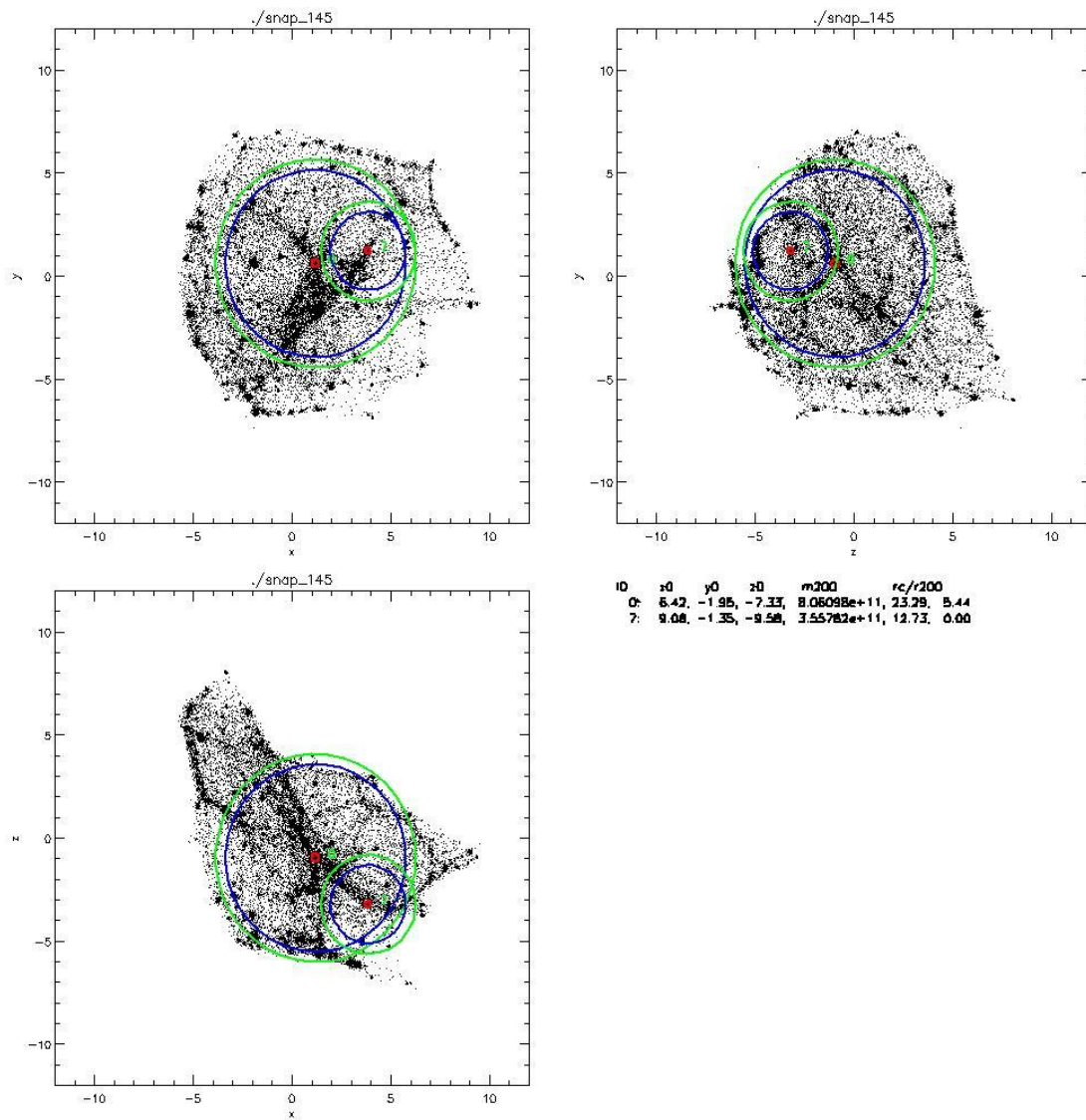
Figure 2.7.: Three orthogonal projections of the high resolution region in the run SIN in the *250x* resolution level. High resolution particles are displayed in black, larger halos in red while blue circles mark the cleaned regions around the halos.

	1x	10x	25x	250x	2500x
$M_{DM}^{part}\,[\,\mathrm{M_\odot\,h^{-1}}]$	1×10^9	1×10^8	4×10^7	4×10^6	4×10^5
$M_{Bar}^{part}\,[\,\mathrm{M_\odot\,h^{-1}}]$	1.6×10^8	1.6×10^7	6.2×10^6	6.2×10^5	6.2×10^4
$\varepsilon_{stars}\,[\,\mathrm{kpc\,h^{-1}}]$	2.0	0.7	0.5	0.24	0.11
$\varepsilon_{gas}\,[\,\mathrm{kpc\,h^{-1}}]$	3.75	1.4	1.0	0.48	0.22

Table 2.3.: Overview of the main simulation parameters.

If intruding particles are found close to the halo of interest, the Lagrangian volume (see Fig. 2.4b) is inspected and enlarged manually to include these low-resolution particles in the high-resolution region. In some cases it is also possible to reduce the size of the Lagrangian volume so that computational expenses are lowered. Eventually, new initial conditions are generated and the simulation run conducted again. This procedure is repeated until the halo of interest is cleaned and the corresponding Lagrangian volume minimized. This way, one obtains the final, dark matter only initial conditions for the resolution level (Schlachtberger, 2014).

2.2.6. Increase Resolution

The resolution can then be increased by applying the ZIC technique again and placing more particles in the high resolution region. The initial conditions are evolved to redshift zero to check for intruding particles again. I note that once the halo is cleaned at low resolution levels, usually no intruders are found at higher resolution levels anymore. This process of increasing the resolution level and checking for intruding particles is repeated until the desired resolution is reached.

We introduce five different resolution levels, denoted *1x*, *10x*, *25x*, *250x* and *2500x*. The main simulation parameters at these resolution levels, including e.g. the mass resolution and gravitational softening factors, are presented in Table 2.3. I further emphasize that the resolution levels *1x* and *25x* coincide with the Magneticum resolution levels denoted *HR* ("high resolution") and *UHR* ("ultra high resolution"), respectively.

As long as cosmological perturbations on the smallest resolved scales are governed by linear, non-chaotic processes, their evolution can be approximated analytically. Once the evolution is dominated by non-linear processes, it becomes necessary to follow the evolution of structures using numerical simulations. Thus, we start our simulation at the redshift of transition between these two regimes. However, with increasing resolution we resolve perturbations on smaller scales which enter the non-linear regime earlier in cosmic history. To ensure the validity of the Zeldovich approximation, the initial redshift of the simulation increases from $z = 60$ in the *1x* runs up to $z = 310$ in the *250x* runs (Schlachtberger, 2014).

2.2.7. Baryonic Runs

Finally, the dark matter only simulations are gasified. To this end, all high-resolution dark matter particles within $5R_{\rm vir}$ of the halo of interest are split into gas and dark matter particles. The particles are displaced by the mean inter-particle separation, while conserving the centre of mass, total mass and momentum. The mass ratio between dark matter and baryonic matter is the cosmic baryon fraction of 15%. Figure 2.8 displays the resulting gasified initial conditions.
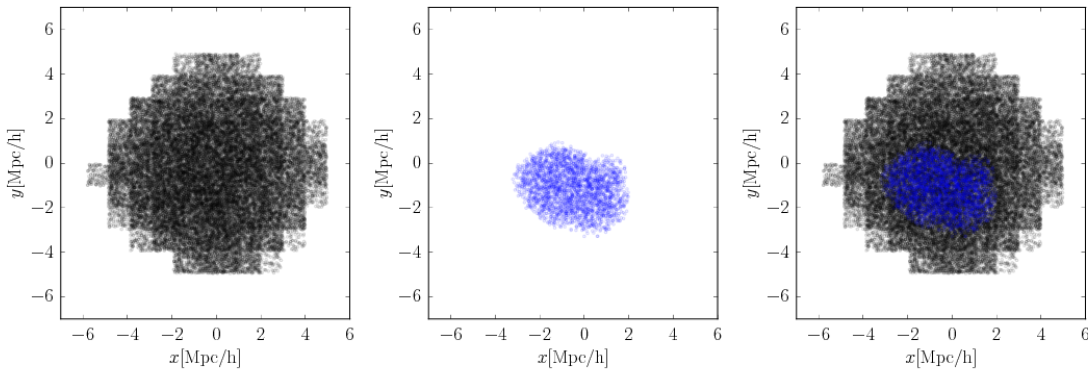

Figure 2.8.: Projection of the gasified initial conditions displaying dark matter particles (left), gas particles (centre) and both particle types together (right).

Only the innermost part of the high resolution region which encloses the halo of interest is gasified. This saves computational expenses, as the number of SPH-particles is minimized. It further introduces an additional border region consisting of high resolution dark matter particles between the gasified region and the low resolution part of the box. This is further illustrated by Fig. 2.8 in which dark matter particles are displayed in black (left panel) and gas particles in blue (central panel) (Schlachtberger, 2014).

The hydrodynamics of the gas are calculated by the smoothed particle hydrodynamics method (see e.g. Monaghan, 1992; Price, 2012) in an entropy conserving formulation (Springel and Hernquist, 2002). The implementation includes higher-order Wendland kernel functions (Dehnen and Aly, 2012) and a time dependent artificial viscosity scheme (Dolag et al., 2005; Donnert et al., 2013). In addition, the simulation includes many advanced physical processes such as multi-phase star formation (Springel and Hernquist, 2003), isotropic thermal conduction (Dolag et al., 2004), stellar evolution and feedback as well as metal enrichment (Tornatore et al., 2003, 2007), a metal-dependent cooling function (Wiersma et al., 2009) and an advanced AGN feedback model (Steinborn et al., 2015).

3. Black Hole Model

Today it is well known that almost every galaxy contains a black hole in its centre. These black holes are much more massive than those that are formed in common supernova explosions. Thus, these black holes are denoted "Super Massive Black Holes" (SMBH) and have masses from 10^6 to $10^9\,\mathrm{M_\odot}$ (e.g. Narayan and Quataert, 2005).

In General Relativity black holes are fully described by only two parameters, namely mass and spin (neglecting their electric charge, as black holes in a astrophysical context are expected to be neutral (Narayan and Quataert, 2005)). However, in the context of galaxies and cosmological simulations SMBHs are much more complicated objects. If a SMBH accretes matter, it is referred to as an Active Galactic Nucleus (AGN) which can reach luminosities up to $10^{48}\,\mathrm{erg\,s^{-1}}$. In fact, these objects alone might outshine the rest of their host galaxy (Narayan and Quataert, 2005). This way, AGNs are capable of influencing entire galaxies, clusters of galaxies and the intra cluster medium within them. This highlights the relevance of AGN for the evolution of structures on all scales (Kaiser and Binney, 2003; Fabian et al., 2003).

In the following I shortly review those aspects of AGN feedback and accretion that are most relevant for our study. I further mention ways of implementing these in cosmological simulations by following the discussion of Steinborn et al. (2015).

Bondi Accretion   Bondi (1952) assumed a steady gas flow from an isotropic and isothermal sphere of gas to estimate the accretion rate of black holes. With these assumptions he found for the accretion rate

$$\dot{M}_{\mathrm{B}} = \frac{4\pi G^2 M_\bullet^2 \rho_\infty}{\left(c_s^2 + v^2\right)^{3/2}} \tag{3.1}$$

with the gravitational constant G, the black hole mass $M_\bullet$, the density ρ, the sound speed in the gas c_s and the relative velocity of gas and black hole v (Bondi, 1952; Shima et al., 1985). Implementing this equation in cosmological simulations is not simple. Springel (2005) uses the formulation

$$\dot{M}_{\mathrm{B}} = \frac{4\pi \alpha G^2 M_\bullet^2 \langle\rho\rangle}{\left(\langle c_s\rangle^2 + \langle v\rangle^2\right)^{3/2}} \tag{3.2}$$

where the used averages are calculated via SPH kernel estimations. As the computed values for $\langle\rho\rangle$, $\langle c_s\rangle$ and $\langle v\rangle$ depend on the used kernel and the considered number of

neighbours, other authors proposed different implementations of the Bondi accretion model (see e.g. Choi et al., 2012).

The Boost Factor   The factor α in equation 3.2 is introduced as an boost factor to account for the limited resolution in numerical simulations. Steinborn et al. (2015) argues that due to this limited resolution, the density in the proximity of the black hole may be underestimated while the sound speed may be overestimated resulting in systematically to low accretion rates. However, defining a suitable value of the boost factor α is difficult.

Booth and Schaye (2009) parametrize the boost factor based on the density while Vogelsberger et al. (2013) try to use an equilibrium between feedback and cooling to estimate α (see also Sect. 5.2.6). For instance, Springel (2005) use $\alpha = 100$, whereas Steinborn et al. (2015) use $\alpha = 100$ for cold and $\alpha = 10$ for hot gas. The influence of the boost factor α and its different parametrizations on disc galaxies in our Zoom-Simulations will be tested in Sect. 5.2.5 and 5.2.6.

In the AGN model of Steinborn et al. (2015) the Eddington accretion rate, which describes an equilibrium between AGN feedback and gas cooling, is used as an upper limit to the accretion rate. The Eddington accretion rate is given through

$$\dot{M}_{\mathrm{Edd}} = \frac{4\pi G M_{\bullet} m_{\mathrm{p}}}{\eta_{\mathrm{Edd}} \sigma_{\mathrm{T}} c} \tag{3.3}$$

with the proton mass m_{p}, the Thompson scattering cross section σ_{T}, and the feedback efficiency η_{Edd}. Furthermore, the model explicitly distinguishes between the accretion of hot and cold gas. To differentiate between the two gas phases, a threshold of $T = 5 \times 10^5 \mathrm{K}$ is introduced. Steinborn et al. (2015) argues that when calculating the accretion rate for cold gas only, a higher accretion rate is found than for both gas phases together. As a result of this, black holes grow faster in quasar-mode and allowing an accretion rate above the Eddington limit (as used in other simulations) is not necessary (see Steinborn et al., 2015, for a more detailed discussion).

AGN Accretion Modes   Various studies have shown that there are two different modes of accretion onto and feedback from AGNs: radio-mode (also denoted as jet-mode) and quasar-mode. Black holes themselves grow primarily in quasar-mode. In this state, an accretion disc forms around the black hole which allows high accretion rates, up to the Eddington accretion rate. This accretion disc can be observed as blue bump in the spectra of Seyfert galaxies or quasars (see e.g. Elvis et al., 1994; Prieto et al., 2010). Accretion in the quasar-mode continues until the gas cooling and the feedback balance each other. Once feedback and cooling are in equilibrium, black holes reach the $M_{\mathrm{BH}} - M_{\mathrm{stellar}}$ relation (Churazov et al., 2005; Steinborn et al., 2015). At the same time, the accretion rate is lowered and the AGN moves from the quasar-mode to the radio-/jet-mode. Now black holes evolve along the $M_{\mathrm{BH}} - M_{\mathrm{stellar}}$ relation, while its feedback is dominated by large jets (Russell et al., 2013; Mezcua and Prieto, 2014). Steinborn et al. (2015) uses a threshold of $\dot{M}_{\bullet}/M_{\mathrm{Edd}} = 0.05$ to

distinguish between radio- and quasar-mode while taking into account a continuous transition between the feedback processes in both modes.

Radius of Feedback Influence   In the implementation used in this study, the AGN interacts with its host galaxy only within a limited range. The radius of this sphere of influence corresponds to the radius "infinity" in the original formulation of the Bondi model. In other words, accretion onto and feedback from the AGN do influence their environment only up to a limiting radius, which we denote "interaction radius" in the rest of this study.

Black Hole Physics   As also commonly used in other studies, the black holes themselves are implemented as collisionless sink particles which incorporate all relevant properties, such as their true mass, dynamical mass, interaction radius, accretion rate, etc.

In our implementation the black holes are allowed to move freely. In other studies, the black holes are tied to the most bound particles of the subhalo in order to assure all black holes stay in the centre of their host galaxies. As a result of this, black holes spuriously jump from galaxy to galaxy in the context of mergers. Thus, allowing black holes to move freely but having them reside in the centre of their host galaxies self-consistently represents a significant advantage. However, this also adds a substantial amount of complexity Steinborn et al. (2015).

In fact, conservation of momentum in the accretion of gas onto the black hole does play an important role, as it might influence the position of the black hole particle relative to the galaxy centre. It is relevant in how far momentum is strictly conserved, or the momentum transfer modelled in a certain way, and when the momentum is transferred. Similarly, one might consider not to use any momentum conservation in the context of AGN accretion. The relevancy of this is further discussed and tested in Sect. 4.4.

Moreover, it may be unclear how to decide which black hole should be swallowed by another black hole in the context of a merger. In previous versions of GADGET this was implemented in such a way that the swallowed black hole was selected by particle ID. Naturally, this implementation does not have a physical justification. In the most recent code version used in this study, the more massive black hole swallows the less massive black hole. Implications of this implementation and possible improvements are discussed in Sect. 4.3.

For a more detailed discussion of the processes mentioned above, see Fabjan et al. (2010); Hirschmann et al. (2014); Steinborn et al. (2015).

4. Black Hole Merger

In the framework of hierarchical structure formation, small objects continuously merge and eventually form larger and larger structures. In this context, mergers of individual galaxies are a common event. In general, the merging of two galaxies also implies the merging of their central SMBHs. In fact, it is of great importance to model this process correctly regardless of redshift or mass ratio of the two merging galaxies. Thus, we revisit the implementation of black hole merger processes in this chapter.

4.1. Black Holes in Galaxy Mergers

Massive black holes usually reside in the centre of their host galaxies. However, shortly after a galaxy merger the SMBHs are not necessarily located at the centre of the remnant galaxy. Instead, while the black holes are orbiting within the remnant, they loose energy due to dynamical friction. As a result, they sink towards the centre and eventually form a binary black hole system. If this system is tightly bound, the system looses further energy by gravitational radiation and eventually the two black holes merge (see also Binney and Tremaine, 2008).

Binney and Tremaine (2008) derive an estimate for the timescale of the decay of black hole orbits in galaxies due to dynamical friction. They conclude that a black hole on a circular orbit in a typical initial configuration ($r_i = 5\,\mathrm{kpc}$, $M = 10^8\,\mathrm{M_\odot}$, $v_i = 200\,\mathrm{km\,s^{-1}}$) has a inspiral time into the centre of only $\sim 3\,\mathrm{Gyr}$. In fact, black holes on strongly eccentric orbits are expected to have a shorter inspiral timescale as they pass through high density regions.

Unfortunately, this process cannot be resolved in cosmological simulations in its entire complexity. Instead, the process is modelled in a simplified way which reproduces the physical events. To this end, the code has to decide if and when two black holes merge and subsequently determine which black hole will be swallowed by the other one. At the same time a realistic black hole merger timescale has to be reproduced. In fact, both steps are of crucial importance in order to obtain a realistic merger remnant. Thus, I revisit the implementation of the two steps and develop improvements in the following.

4.2. Black Hole Merger Conditions

If two SMBHs experience a relevant close encounter, the code evaluates three conditions in order to determine if the black holes merge. These three conditions are:

- Relative velocity: $v_{\rm rel} < $ CSND_FRAC_BH_MERGE $\cdot\ c_s$

- Relative distance: $r_{\rm rel} < 2 \cdot$ KD_BH_MAX_DIST

- Relative binding energy: $b_{\rm rel} < $ CSND_FRAC_BH_MERGE $\cdot\ c_s^2$

The terms CSND_FRAC_BH_MERGE and KD_BH_MAX_DIST are constants with default values of 0.5 and $5\,[\,{\rm kpc}\,{\rm h}^{-1}]$ in our simulation setup. These conditions are chosen to ensure that the merging black holes have an appropriate relative distance as well as relative velocity, and that both black holes are sufficiently bound within the same potential. Eventually, the two black holes merge if the binding energy criterion and at least one of the distance and velocity criteria are fulfilled.

Figure 4.1 illustrates the three criteria based on an example from the run *Thermal-JetModeFeedback* (see Sect. 5.2.3). The upper panels show distributions of relative velocities in internal units and CSND_FRAC_BH_MERGE $\cdot\ c_s$, the central panels display distributions of relative distances and $2 \cdot$ KD_BH_MAX_DIST, and the lower panels show distributions of the relative binding energy and CSND_FRAC_BH_MERGE $\cdot\ c_s^2$. Moreover, the panels are split in three distinct time bins for which the time is measured from the first relevant close encounter between the two black holes.

The figure clearly indicates that only the relative distance criterion is fulfilled. The other two criteria are not fulfilled in any time bin. Therefore, the two black holes in this example do not merge within $3\,{\rm Gyr}$ which is arguably a unreasonable long period of time. Thus, we highlight that it is in general necessary to adjust the values of these two constants in order to obtain realistic black hole merging timescales. For this study, we conclude to use CSND_FRAC_BH_MERGE $= 1$ to achieve shorter and more sensible merger timescales.

4.3. Black Hole Swallowing

In the last phase before a real black hole merger, both black holes are tightly bound to each other and located in the centre of their host galaxy (as discussed above). However, due to the merger conditions introduced in Sect. 4.2, we expect the merging black holes in our simulation to have a typical separation in the order of magnitude of KD_BH_MAX_DIST, which is set to $5\,{\rm kpc}\,{\rm h}^{-1}$. As we aim to resimulate Milky-Way-like disc galaxies, this relative distance is large compared to the size of the galaxy itself. Thus, it is of crucial importance to model correctly which black hole particle in the simulation is swallowed by the other one in order to assure the resulting black hole is located in the centre of the merger remnant.
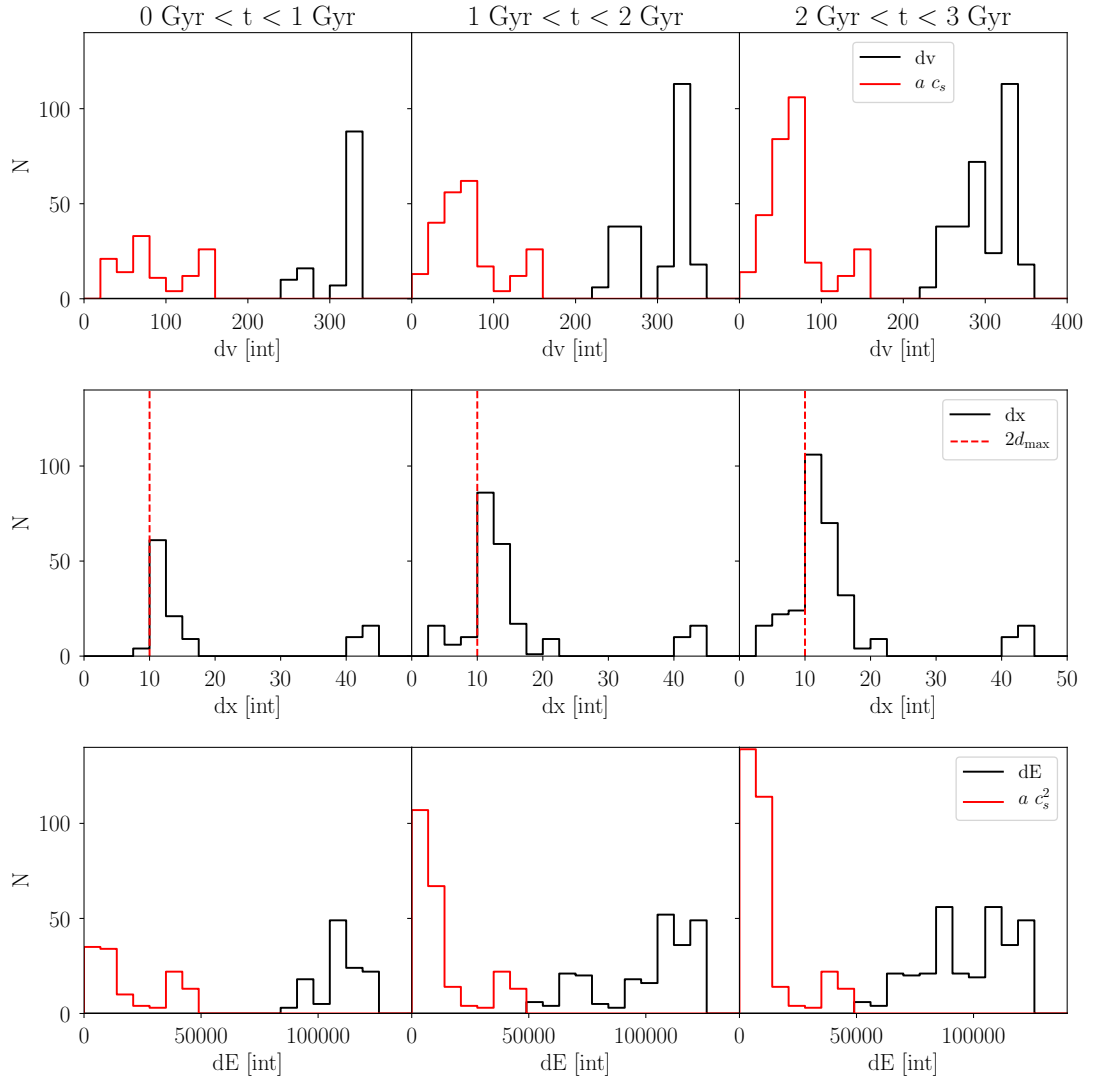
Figure 4.1.: Upper panels: Distributions of relative velocities (black) and `CSND_FRAC_BH_MERGE` · c_s (red). Central panels: Distributions of relative distances (black) and 2· `KD_BH_MAX_DIST` (red). Lower panels: Distributions of relative binding energies (black) and `CSND_FRAC_BH_MERGE` · c_s^2 (red). In addition, the panels are horizontally splitted in three bins in time, measured from the first relevant close encounter between the two black holes.

In prior versions of GADGET the merging black hole has been swallowed by the black hole with the smaller particle ID. Naturally, this implementation does not have a physical justification. Subsequently, the implementation has been changed to account for the masses of the black holes so that the less massive black hole is swallowed by the more massive one.

As a massive BH is, in general, expected to sit deeper in the potential than a less massive one, it is sensible to merge the less massive black hole onto the more massive one. It is instructive to consider the case of a minor merger in which a small galaxy in accreted by a more massive, main galaxy. In this context, the more massive black hole is located at the centre of the main galaxy. As the small galaxy is disrupted and accreted onto the main galaxy, it makes perfect sense to have the merging black hole being swallowed by the massive black hole in the centre of the main galaxy.

However, this assumption is not always valid, in particular at large redshifts. This is displayed in Fig. 4.2 which shows three orthogonal projections of the main progenitor of galaxy *a* in the run *ThermalJetModeFeedback* (see Sect. 5.2.3). Black, magenta and cyan dots refer to stellar, hot gas and cold gas particles, respectively. Red crosses mark the positions of black holes which are annotated with the number of progenitor black holes ("PC =") as well as their masses ("MA =", in units of $\log \left(M / 1 \times 10^{10} \, \mathrm{M_\odot} \right)$). Snapshot number, scale factor and redshift are shown in the headers of the panels.

The upper two panels of Fig. 4.2 display a triple encounter at a redshift of ~ 3. All three galaxies and their black holes still have similar masses. In the course of this encounter, two black holes merge onto the most massive black hole. However, the most massive black hole and its host galaxy do not directly merge with the other galaxies. Instead, this galaxy keeps orbiting the merger remnant for a short period of time, before being disrupted and accreted onto the remnant. However, the black hole itself is now located significantly outside of its host galaxy and is not expected to sink to the centre of the galaxy at any reasonable timescale.

This displacement of the black hole results in various problems. Firstly, theoretical considerations as well as observations do not expect SMBHs to be located significantly outside of their host galaxy. Thus, the final configuration of remnant and black hole has to be considered unrealistic. Secondly, the orbiting black hole might introduce disturbances in the galactic disc and might eventually trigger spiral arms and bars in an unphysical way. Thirdly, the AGN feedback is not acting on the central regions of the disc galaxy. Instead, the AGN feedback is deposited in different parts of the galaxy outskirts, as the black hole orbits its host galaxy. It is widely accepted that black holes and their feedback processes play a dominant role in the formation and evolution of galaxies. Thus, the black hole displacement might have a unphysical influence on the development of the galaxy, the growth of bulge and black hole itself, as well as on establishing the fundamental scaling relations between galaxy and black hole properties. Finally, as the black hole orbits the galaxy at a compareably large distance, the code might decide to seed a new black hole in the centre of the galaxy. As this newly spawned black hole has a lower mass, it
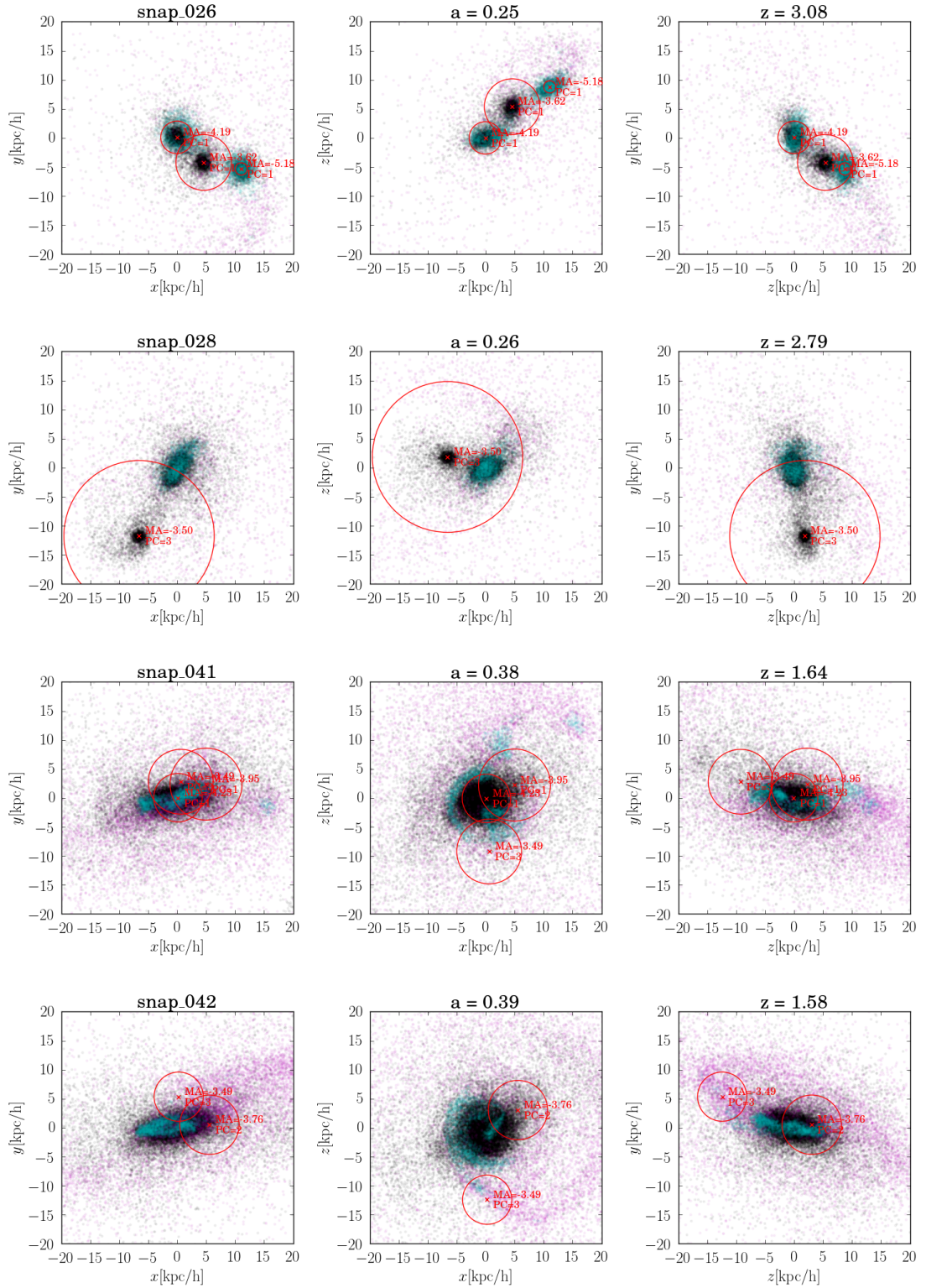
Figure 4.2.: Orthogonal projections of galaxy *a* in the run *ThermalJetModeFeedback*. Black, magenta and cyan dots refer to stellar, hot gas and cold gas particles, respectively. Red crosses mark the positions of black holes which are annotated with the number of progenitor black holes ("PC =") as well as their masses ("MA =", in units of $\log\left(M/1 \times 10^{10}\,\mathrm{M}_\odot\right)$). Snapshot number, scale factor and redshift are shown in the headers of the panels.

quickly merges onto the original black hole and is thus removed from the galaxy centre. This artificial process repeats multiple times through the evolution of this galaxy and is illustrated in the two lower panels of Fig. 4.2.

It is instructive to consider the position of the black holes in the potential of the galaxy which is displayed in Fig. 4.3. The upper left panel shows a projection of the galaxy, the other panels show the gravitational potential projected on the x and y axis, respectively. Colours and markers are chosen as above. The upper group of panels clearly illustrate how the central black hole is located at the minimum of the potential. Other black holes are orbiting the galaxy at larger separations, as a result of the process discussed above. Due to the fact that the orbiting black hole is more massive than the central black hole, the central black hole is swallowed and thus removed from the centre of the galaxy (see lower group of panels).

Therefore, it seems more reasonable to use the potential of the black holes to determine which black hole should be swallowed. This option has been implemented in the code through the switch `LS_SAVE_POTMIN_ID` and tested in both *25x* and *250x* runs. In the resulting simulations, black holes reliably merge towards the centre of the remnant galaxy. Thus, the problems discussed above are avoided and we yield a merged galaxy with a realistic location of the SMBH.

4.4. Black Hole Drag

Above I discussed the necessity of merging two black hole particles in the correct manner in order to assure that the black holes stay self-consistently in the centre of the galaxies. This is especially important as we do not fix the black hole particles to the potential minima of their host galaxies, but allow them to move around freely. This additional degree of freedom is in contrast to other cosmological simulations and is an advantage we also aim to adopt to simulations with higher resolutions. In this context, we consider a further possibility which might support the self-consistent positioning of black hole particles in the centres of galaxies, namely the drag of accreted gas onto the black holes.

The switch `BH_DRAG` enables the momentum transfer from accreted gas onto the accreting black hole. If the accreted gas itself stays in the galaxy persistently, its average momentum relative to the galaxy should be zero. Thus, the black hole should sink down to the centre of the galaxy as the different momentum components from the accreted gas cancel out. Further implementations allow to change the behaviour of the black hole drag. The switch `LS_USE_COLD_GAS_FOR_BH_DRAG` only accounts for cold gas in the drag whereas the switch `LS_VELOCITY_LIMIT_FOR_BH_DRAG` allows to set a limit on the maximum relative velocity of the gas to be considered for the computation of the drag.

We test the effect of this module on the positioning of the black hole particles by conducting three simulation runs at the *250x* resolution level. This includes one
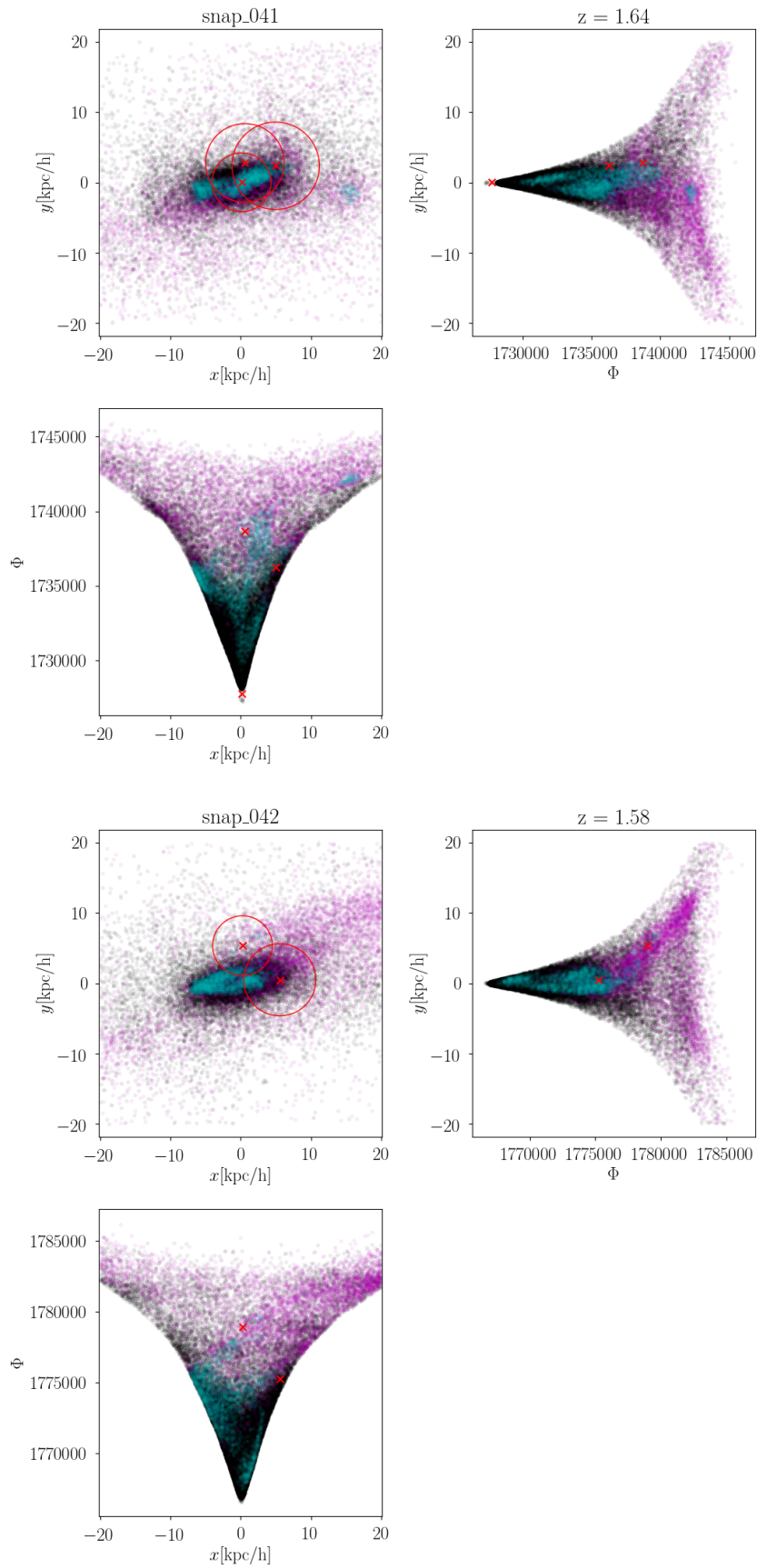
Figure 4.3.: The upper group of panels refers to snapshot 41 of galaxy *a* in the run *Thermal-JetModeFeedback*, the lower group to snapshot 42. Within each group, the upper left panel shows a projection of the galaxy, the other panels show the gravitational potential projected on the x and y axis. Colours and markers are chosen as above.

run without black hole drag, one run with drag and the cold gas constraint, and one run with drag and velocity limit of $50\,\mathrm{km\,s^{-1}}$.

Influence on the Black Hole Position   The left column of Fig. 4.4 displays the displacement of the black holes with respect to the galaxy centre, latter as determined by the halo finder Subfind. The right column shows the velocities of black hole, cold gas and hot gas relative to the galaxy centre. The first row refers to the run without black hole drag, the second row displays results from the run with drag and cold gas constraint, while the third row displays the run with drag and velocity limit. The different number of entries in the histograms, in particular in the left column of Fig. 4.4, is connected to a maximum considered displacement of $3\,\mathrm{kpc}$. Naturally, if the black hole has a displacement larger than $3\,\mathrm{kpc}$ in a snapshot, it cannot be displayed in the histogram anymore.

In the reference run without drag, the black holes are perfectly positioned in the galaxy centre. In no snapshot the displacement is larger than one smoothing length of $\epsilon = 0.24\,\mathrm{kpc\,h^{-1}}$. This further confirms the functionality of the black hole merger processes as discussed in Sect. 4.3. However, in both other runs the black hole is significantly displaced. The relative distances are widely spread, ranging up to deviations larger than $3\,\mathrm{kpc\,h^{-1}}$, as indicated by the lower number of items in these histograms. These findings are consistent with the distributions of relative velocities of the black holes. In the run without drag all relative velocities are below $50\,\mathrm{km\,s^{-1}}$, with a peak at approximately $20\,\mathrm{km\,s^{-1}}$. In contrast, the relative velocities in the other runs are significantly higher and have a considerable spread, although the relative velocities of both cold and hot gas are still low.

One might speculate that the increased displacement of the black holes with drag is connected to small blobs of gas which become resolved at high resolution levels. In this framework, the black hole is initially kicked by smalls blobs of gas which are accreted by the galaxy. During its subsequent orbit throughout the galaxy, the black hole might receive additional kicks from gas and, thus, is further disturbed. As a result, the black hole will not fall back to the galaxy centre within any reasonable timescale. Thus, it is not advantageous to use the black hole drag in this setup of Zoom-Simulations.

Influence on the Galaxy Morphology   In fact, the position of the black hole within the galaxy has a significant influence on the resulting morphology. Although this fact is related to problems with the AGN feedback mechanism discussed in Sect. 5, it is instructive to consider the corresponding effects here.

If the black hole is located in the galaxy centre, the black hole feedback acts constantly on the same gas particles and eventually generates a hole in the gas component in the centre of the galaxy. In the majority of the cases, the radius of this hole coincides well with the black hole interaction radius (see also Sect. 5). As a result of this, no realistic morphological features at small radii, such as bars and inner rings, can form (see upper panels of Fig. 4.5). In contrast, if the black hole
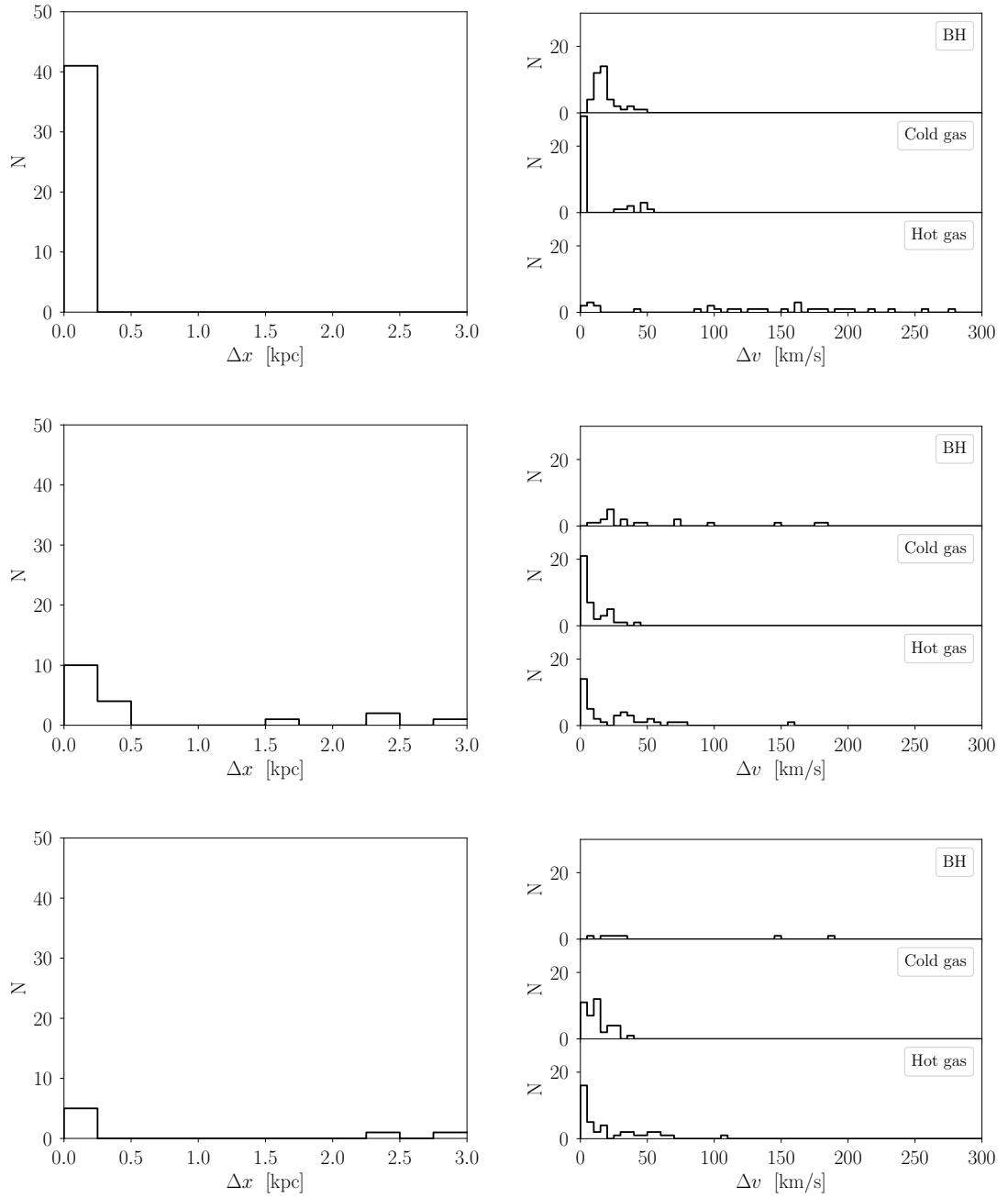
Figure 4.4.: Relative displacement of the black hole (left column) and relative velocities of black hole, cold gas and hot gas (right column) with respect to the galaxy centre, latter as determined by the halo finder `Subfind`. The first row refers to the run without black hole drag, the second row displays results from the run with drag and cold gas constraint, while the third row displays the run with drag and a velocity limit of $50\,\mathrm{km\,s^{-1}}$.

orbits throughout the galaxy, there is a large velocity difference between gas and black hole. Therefore, the black hole does accrete matter at very small accretion rates and the resulting feedback is weak. Thus, no significant holes in the discs are produced and a realistic morphology, including spiral arms and bars, can form and develop (see lower panels of Fig. 4.5). I further highlight that the different positioning of the black hole has no influence on the resulting $M_{\mathrm{BH}} - M_{\mathrm{stellar}}$ relation of the galaxy (see also Sect. 5).
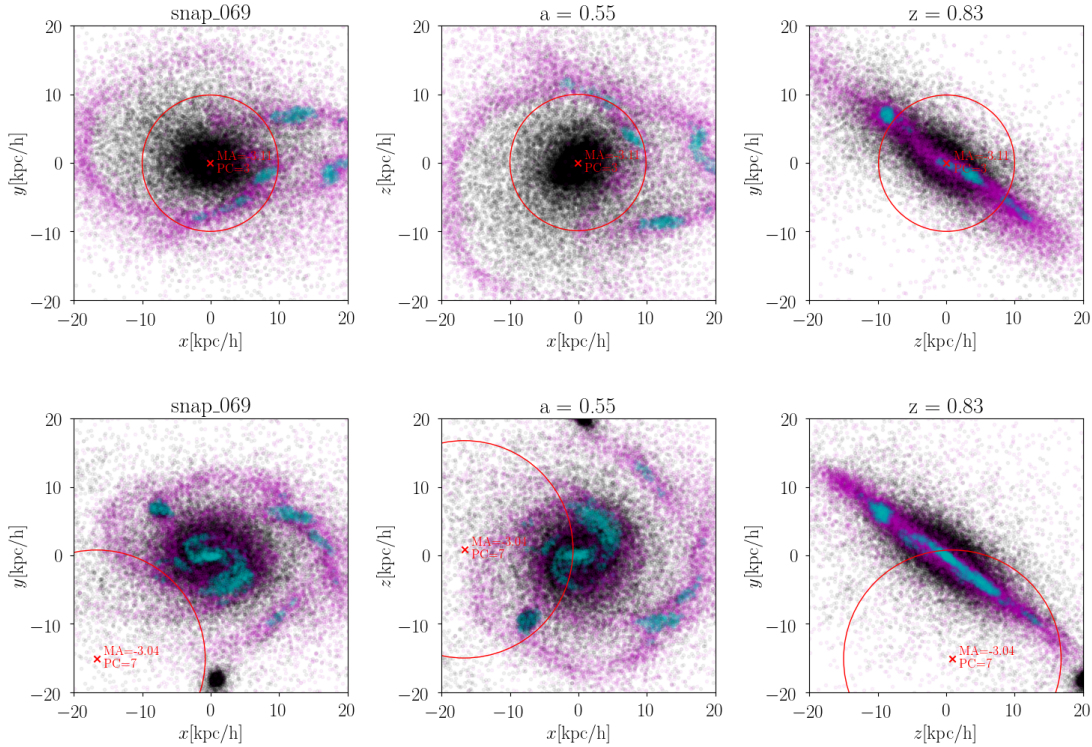

Figure 4.5.: Three orthogonal projections of the main galaxy SIN for the run without black hole drag (upper panels) and with the velocity limit (lower panels). Stars are displayed in black, hot gas in magenta, cold gas in cyan and black holes as red crosses. The upper panels illustrate how the black hole feedback generates a significant hole in the gas component within the black hole interaction radius. Due to the movement of the black hole in the lower panels, no considerable hole develops and morphological features, such as a weak bar, can also be seen at small radii.

4.5. Summary

The processes described in this chapter are suitable examples to illustrate the difficulties in implementing physical processes in numerical simulations, in particular when the processes in consideration are fairly below the resolution limit. Nonetheless, the chosen implementations should not only reproduce the expected results, but also account for the actual ongoing processes. For example, many cosmological simulations just tie black holes to the potential minima of their host galaxies. Although this nicely reproduces the observed results, the result itself is purely artificial. In contrast, we try to reproduce the actual mechanisms by allowing black

holes to move freely and to interact with other galaxies and black holes, so that the result is, to some extent, a self-consistent outcome of the simulation.

I highlight here that many of the real physical mechanisms that are responsible for black holes to sink to the centres of galaxies and finally to merge are significantly below the resolution limit and thus not included in this simulation.

5. Feedback from Active Galactic Nuclei

AGN feedback does have a significant impact on the evolution of structures on all scales. As we aim to advance the resolved mass range down to Milky-Way-like disc galaxies and beyond, it is of essential importance to conduct a in-depth investigation of the used AGN feedback model and its influences on the low-mass galaxies in consideration.

Testing the AGN feedback at the *25x* resolution level reveals that the fundamental scaling relations fit well with the expectations. However, this is not surprising as the *25x* resolution level coincides with the *UHR* resolution level in the Magneticum simulations, which are know to reproduce these relations well. While the AGN feedback works nicely in the *25x* resolution level, it needs to be tested and refined to meet the requirements at the *250x* resolution level and beyond. Thus, I will provide an overview about the problems which arise at higher resolution levels and present ideas to improve the implementation. To this end, I run various parameter tests which are presented in the following.

5.1. Properties in Consideration

When comparing the properties of resimulated galaxies in the context the AGN feedback model, we consider various properties and fundamental scaling relations. This includes the mass-size relation, the stellar-mass stellar-angular-momentum ($M_{\text{star}} - j_{\text{star}}$) relation together with the b-value, the mass accretion histories and evolution of star formation rates, the stellar-mass black-hole-mass ($M_{\text{BH}} - M_{\text{stellar}}$) relation, as well as a visual inspection of the galaxies. I shortly review the implications of these relations in the following.

The Mass-Size Relation   Early- as well as late-type galaxies are known to show a correlation between their mass and size, or equivalently between luminosity and surface brightness. This correlation behaves in such a way that more massive galaxies are larger in size. Lange et al. (2015) discusses that this correlation fundamentally arises from the scaling of angular momentum and halo mass (see also Fall and Efstathiou, 1980; Dalcanton et al., 1997; Mo et al., 1998; Obreschkow and Glazebrook, 2014). Thus, this relation contains valuable information about the history of the

galaxies and allows to test evolutionary models (Lange et al., 2015; Romanowsky and Fall, 2012; van der Wel et al., 2014). We use the mass-size relation to test the properties of the resimulated galaxies in this context. Thus, the upper left panel of each figure in Sect. 5.2 shows the evolution of the main galaxy in the mass-size parameter space. Redshifts are color-coded from in the range $z = 2$ to 0. For better comparison, I overplot lines of the mass-size relation of early- (red lines) and late-type galaxies (blue lines) from van der Wel et al. (2014) at different reference redshifts.

The Stellar-Mass Stellar-Angular-Momentum Plane We further consider the position of the galaxies in the stellar-mass stellar-angular-momentum plane. In fact, the position of the galaxies in this plane can be quantified by using the so called "b-value"

$$b = \log \left(\frac{j_{\text{star}}}{\text{kpc km s}^{-1}} \right) - \frac{2}{3} \log \left(\frac{M_{\text{star}}}{\text{M}_\odot} \right) \qquad (5.1)$$

with the stellar angular momentum j_{star} and stellar mass M_{star} (Teklu et al., 2015; Romanowsky and Fall, 2012). Romanowsky and Fall (2012) expect disc galaxies to have a b-value around -4, whereas pure spheroidals have a b-value around -5. Teklu et al. (2015) has identified galaxies with b-values as low as -6.25 within the Magneticum Pathfinder simulations. The upper right panel of each figure in Sect. 5.2 displays this stellar-mass stellar-angular-momentum plane. Redshifts are again color-coded in the range $z = 2$ to 0. To better illustrate the different b-values in the plot, I also plot lines following $j \propto M^\alpha$ with $\alpha = 2/3$. Hence, the solid blue line has $b = -4$ and the solid yellow line $b = -5$, while other lines are plotted in steps of $\Delta b = 0.25$.

Mass Accretion and Star Formation History Plots of the mass accretion and star formation history are displayed in the second row of each figure. Total masses of dark matter (black), stars (red), hot gas (magenta) and cold gas (blue) are measured within $3R_e$, respectively. The same is the case for the total star formation rates.

The Black-Hole-Mass Stellar-Mass Relation As discussed above, a black hole mainly grows in quasar mode during which it is fed by an accretion disc with accretion rates close to the Eddington accretion rate. Thus, the black holes grow to larger masses until the feedback is strong enough to balance the cooling. At this point, the accretion rate decreases, the radio-/jet-mode accretion takes over and the black hole reaches the $M_{\text{BH}} - \sigma$ and consequently the $M_{\text{BH}} - M_{\text{star}}$ relation (Churazov et al., 2005; Steinborn et al., 2015). This $M_{\text{BH}} - \sigma$ relation is usually given by

$$\log \left(\frac{M_{\text{BH}}}{\text{M}_\odot} \right) = a \cdot \log \left(\frac{\sigma}{200 \, \text{km s}^{-1}} \right) + b \qquad (5.2)$$

with $a = 4 \pm 0.3$ and $b = 8.2 \pm 0.1$ as observationally constrained by Binney and Tremaine (2008), whereas McConnell and Ma (2013) found $a = 5.64 \pm 0.32$ and $b = 8.32 \pm 0.05$.

This relation represents a fundamental property of black holes and their host galaxies and thus, should always be reproduced by simulations. In fact, this two-phase growth of black holes has been illustrated by cosmological simulations before (see e.g. Fig. 4 from Steinborn et al., 2015). To this end, black holes are usually seeded below the $M_{\mathrm{BH}} - M_{\mathrm{stellar}}$ relation, so that their subsequent growth to and then along the $M_{\mathrm{BH}} - M_{\mathrm{stellar}}$ relation can be reproduced. In the following, I will also investigate the influence of the different black hole seeding masses on the resimulated galaxies.

In the third row of each figure in the following subsections, I present all cleaned galaxies of the run SIN in the $M_{\mathrm{BH}} - M_{\mathrm{stellar}}$ parameter space. The main halo of this resimulation volume is marked with a red cross, other halos are marked by black crosses. The $M_{\mathrm{BH}} - M_{\mathrm{star}}$ relation is given by

$$\log\left(\frac{M_{\mathrm{BH}}}{\mathrm{M}_\odot}\right) = 1.05 \log\left(\frac{M_{\mathrm{bulge}}}{10^{11}\,\mathrm{M}_\odot}\right) + 8.46, \tag{5.3}$$

as taken from McConnell and Ma (2013) and displayed with a dotted line in the plots.

Visual Inspection I further present an image of the main resimulated galaxy for each of the following parameter tests (fourth row of the figures). These images display three orthogonal projections of the galaxy at redshift ~ 1. Star particles are displayed in black, hot gas in magenta and cold gas in cyan. The positions of black holes are marked by red crosses and their interaction radius displayed by a red circle. The masses ("MA =", in units of $\log\left(M/1 \times 10^{10}\,\mathrm{M}_\odot\right)$) and the number of progenitor black holes ("PC =") are denoted in the images.

5.2. Parameter Tests

5.2.1. Without Black Holes

As a starting point for this parameter study, we conduct a simulation run *without* black holes and the related physical processes. This serves as a reference run in order to quantify the general influence of AGN feedback on the resimulated galaxies. It further allows to compare the influence of the different parameters which are tested in the following subsections.

An overview about the general properties of the main galaxy is shown in Fig. 5.1. Displayed are the mass-size relation and $M_{\text{star}} - j_{\text{star}}$ plane (first row), mass accretion history and star formation rate (second row) as well as three orthogonal projections of the galaxy at $z \simeq 1$ (third row). Naturally, the $M_{\text{BH}} - M_{\text{stellar}}$ relation is omitted, as there are no black holes included in this run.

In general, the mass-size relation of the objects fit well with that of an elliptical galaxy, although the object tends to be too extended at large redshifts and too small at lower redshifts. Its position in the $M_{\text{star}} - j_{\text{star}}$ plane illustrates that the galaxy has a roughly constant b-value of -4.75 throughout cosmic history. This b-value indicates that the galaxy is, at least in the context of its stellar angular momentum, better modelled by a spheroidal galaxy than by a disc galaxy. This becomes further evident in the visual appearance of the galaxy. Although it is disc-shaped, the stellar disc is particularly thick. No prominent spiral structure is obvious. The mass accretion history indicates the presence of cold and hot gas throughout cosmic history and the continuous increase of stellar mass. Star formation rates are reasonable with a peak at a lookback time of 4 Gyr which is probably due to the major merger.

It is evident from this run that simulations without AGN feedback do not produce realistic disc galaxies. It further shows that AGN feedback is also important for low-mass galaxies, probably especially at higher redshifts. At high redshifts the galaxy undergoes frequent and significant merger events. If star formation at this time is not suppressed by AGN feedback, stars form in disturbed, "merger-like" orbits and it is not possible to form a thin disc. Instead, the result is a more early-type galaxy, as found here. Thus, AGN feedback at early times is necessary to allow the gas to settle in a disc before significant star formation sets in. This way a realistic, thin disc can be formed (see Sect. 5.2.2).
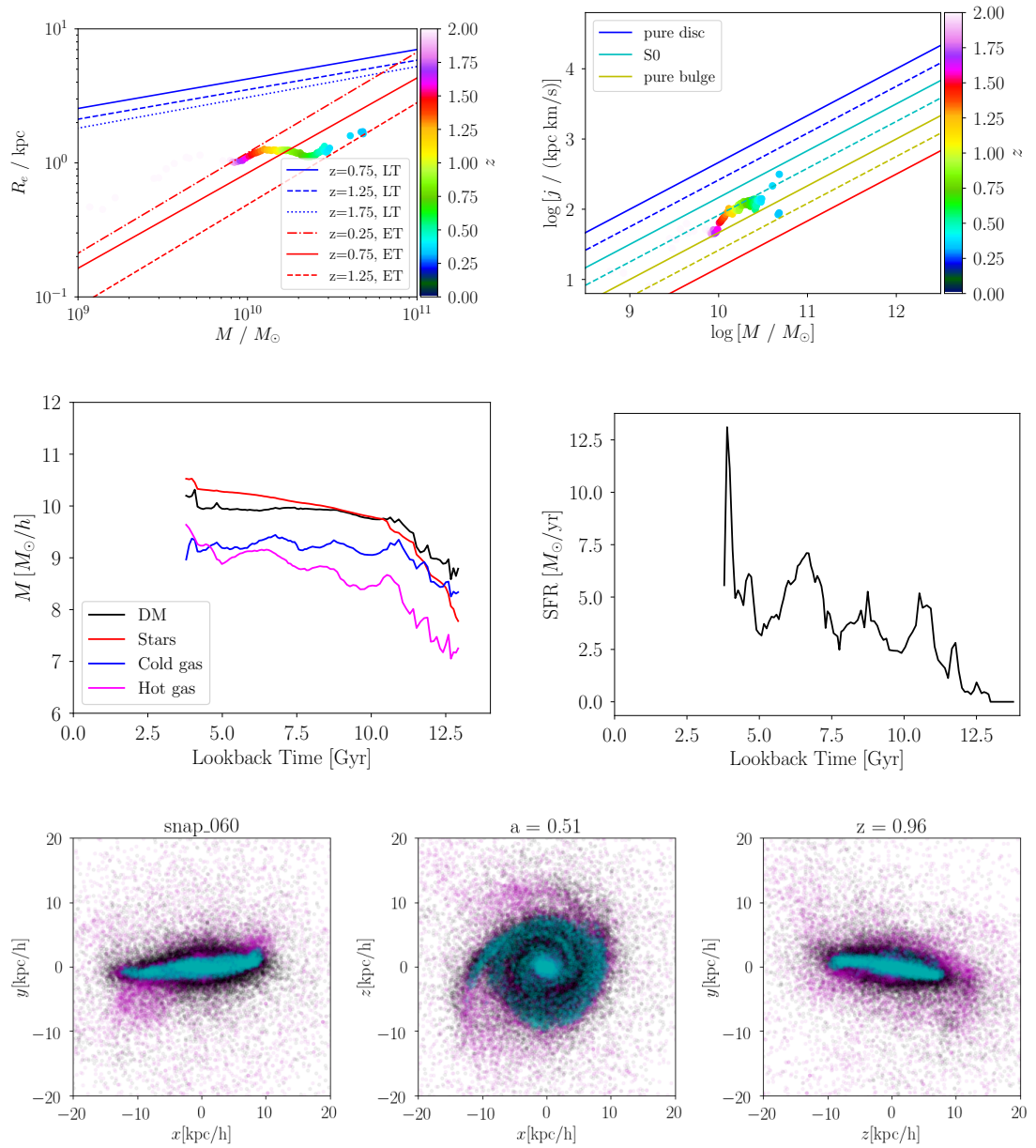
Figure 5.1.: Overview about the properties of the galaxy SIN in the reference run *without black holes*. Displayed are the mass-size and $M_{\mathrm{star}} - j_{\mathrm{star}}$ relation (first row), mass accretion history and star formation rate (second row), as well as three orthogonal projections of the galaxy at $z \simeq 1$ (third row).

5.2.2. With Black Holes

In this section, I conduct a simulation run with standard AGN feedback as reference run for the subsequent investigations. It further serves as a comparison with the run without AGN feedback. I emphasize that this run uses the implementations of black hole mergers as discussed in Sect. 4. In particular, I use here the black hole merger conditions and the merging onto the black hole which sits deeper in the potential well to assure the black hole is located in the centre of the galaxy. The black hole drag module is not used.

An overview about the general properties of the main galaxy is shown in Fig. 5.2. Displayed are the mass-size relation and $M_{\mathrm{star}} - j_{\mathrm{star}}$ plane (first row), mass accretion history and star formation rate (second row), $M_{\mathrm{BH}} - M_{\mathrm{stellar}}$ relation (third row), as well as three orthogonal projections of the galaxy at $z \simeq 1$ (fourth row).

The galaxy roughly fits the expected mass-size relation of late-type galaxies, although it tends to be too large in size. Its evolution towards the mass-size relation of early-type galaxies at higher redshifts can also be seen. The major merger can be identified as an abrupt jump in stellar mass and the subsequent evolution towards the mass-size relation of early-type galaxies. The behaviour in the $M_{\mathrm{star}} - j_{\mathrm{star}}$ plane is similar. The galaxy evolves from b-values which are consistent with a disc/S0 galaxies through the merger towards lower b-values. The merger at $\sim 5\,\mathrm{Gyr}$ is also clearly visible in the mass accretion history as well as in a peak in the star formation rate. I also highlight the low star formation rate in the period from 10 to $5\,\mathrm{Gyr}$, which is in agreement with the low amount of gas, in particular cold gas, in the galaxy. This is further illustrated in the visual image of the galaxy in the fourth row of the figure.

More importantly, this run does not reproduce the $M_{\mathrm{BH}} - M_{\mathrm{stellar}}$ relation well. The majority of the galaxies have significantly too low black hole masses and thus lie below the relation. This implies that the black holes did not accrete sufficient mass to reach this relation. However, state-of-the-art cosmological simulations do reproduce this relation well (see e.g. Steinborn et al., 2015). Nonetheless, one might argue that this position in the $M_{\mathrm{BH}} - M_{\mathrm{stellar}}$ plane is reasonable for late-type galaxies. I will address this problem in further parameter tests below.

I conclude that the implementation of standard AGN feedback already provides essential improvements on the general properties of disc galaxies in these Zoom-Simulations. In comparison with the run without black holes (see Sect. 5.2.1), the galaxies occupy a more realistic place in both the mass-size and $M_{\mathrm{star}} - j_{\mathrm{star}}$ planes. The disc is thinner and shows first morphological features such as spiral arms, although the AGN feedback generates a hole in the gas component in the galaxy centre.
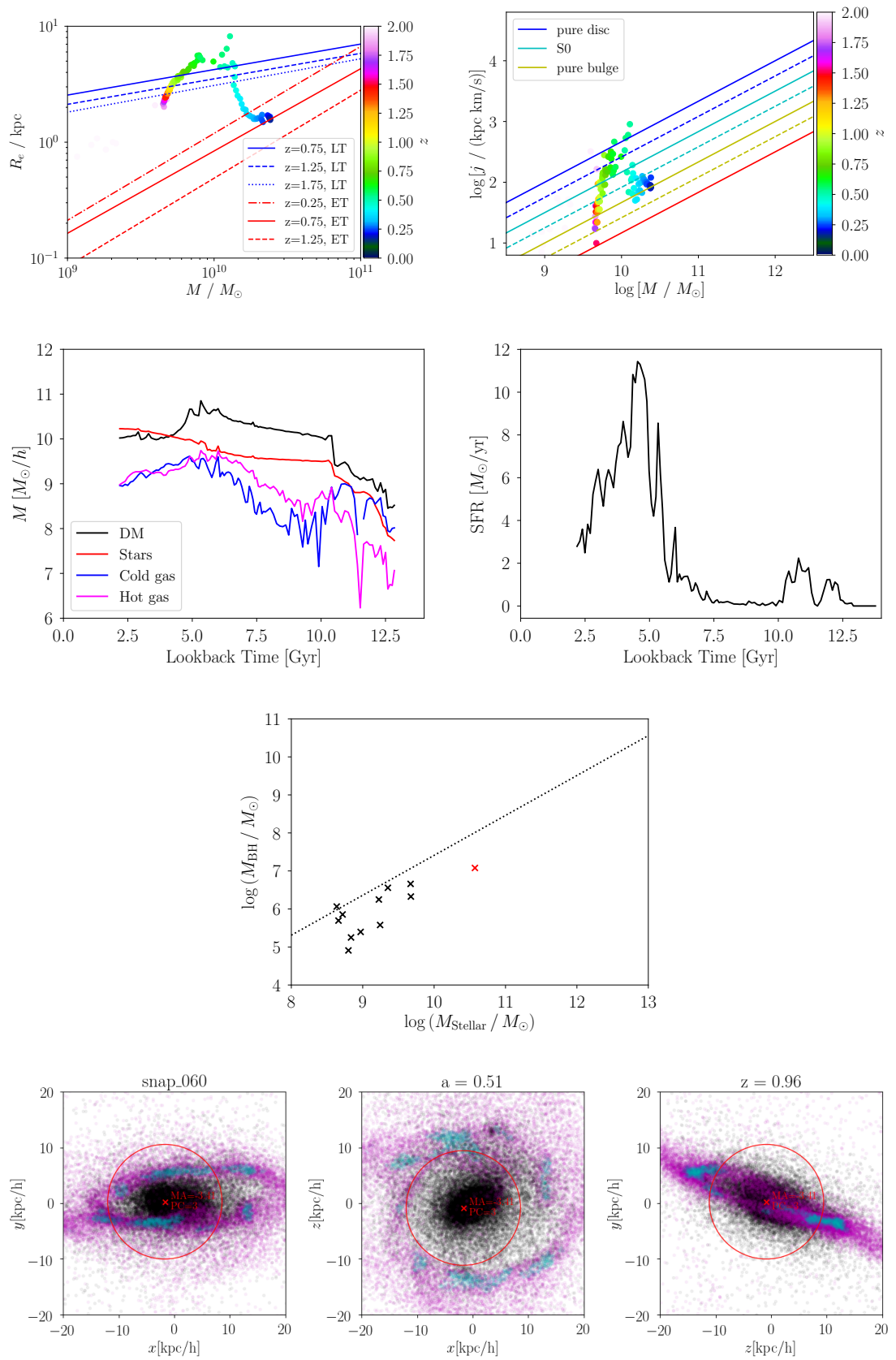
Figure 5.2.: Overview about the properties of the galaxy SIN in the reference run with AGN. Displayed are the mass-size and $M_{\text{star}} - j_{\text{star}}$ relation (first row), mass accretion history and star formation rate (second row), $M_{\text{star}} - M_{\text{BH}}$ relation (third row), as well as three orthogonal projections of the galaxy at $z \simeq 1$ (fourth row).

5.2.3. Thermal Jet Mode Feedback

In the previous test run I found that the AGN feedback generates significant holes in the gas component of the galaxies. Naturally, this affects the central parts of the galaxies so that central structures, for instance bars, cannot develop. The AGN feedback model of Steinborn et al. (2015) distinguishes between the accretion of cold and hot gas. In the same way, we will distinguish between the feedback on hot and cold gas in order to preserve a (cold) gas component at small radii. This has been implemented in the switch `LS_THERMAL_JET_MODE_FEEDBACK` which heats all gas during quasar mode and only hot gas during radio mode accretion. The effect on the resulting galaxies will be investigated in this section.

An overview about the general properties of the main galaxy is shown in Fig. 5.3. Displayed are the mass-size relation and $M_{\text{star}} - j_{\text{star}}$ plane (first row), mass accretion history and star formation rate (second row), $M_{\text{BH}} - M_{\text{stellar}}$ relation (third row), as well as three orthogonal projections of the galaxy at $z \simeq 1$ (fourth row).

The resulting galaxy occupies a reasonable position in both the mass-size and $M_{\text{star}} - j_{\text{star}}$ plane with the major merger being visible through a jump in mass. Also the star formation history is similar to the previous run without thermal jet mode feedback. In particular, the quiescent phase between 10 and 7.5 Gyr and the two peaks in star formation at ~ 11 and ~ 5 Gyr are reproduced well. The $M_{\text{BH}} - M_{\text{stellar}}$ relation is similar to the run without thermal jet mode feedback.

However, the mass accretion history nicely illustrates the effect of the thermal jet mode feedback. In contrast to the previous run of Sect. 5.2.2, the amount of gas is almost constant throughout cosmic history. In particular from 10 to 5 Gyr, the total gas mass is nearly one order of magnitude higher and a similar amount of hot and cold gas is available. I further highlight the nice morphology of the galaxy in this run, although a significant hole in the centre is still evident.

We conclude that the thermal jet mode feedback helps to preserve a larger gas component in the galaxy and, in particular, to yield similar amounts of hot and cold gas. However, the effect is not sufficient to maintain a gas component in the centre of the galaxy, especially within the interaction radius of the black hole. This might be due to a too strong feedback on too few gas particles, and/or a efficient transport of heat from the hot in the cold component of the gas.
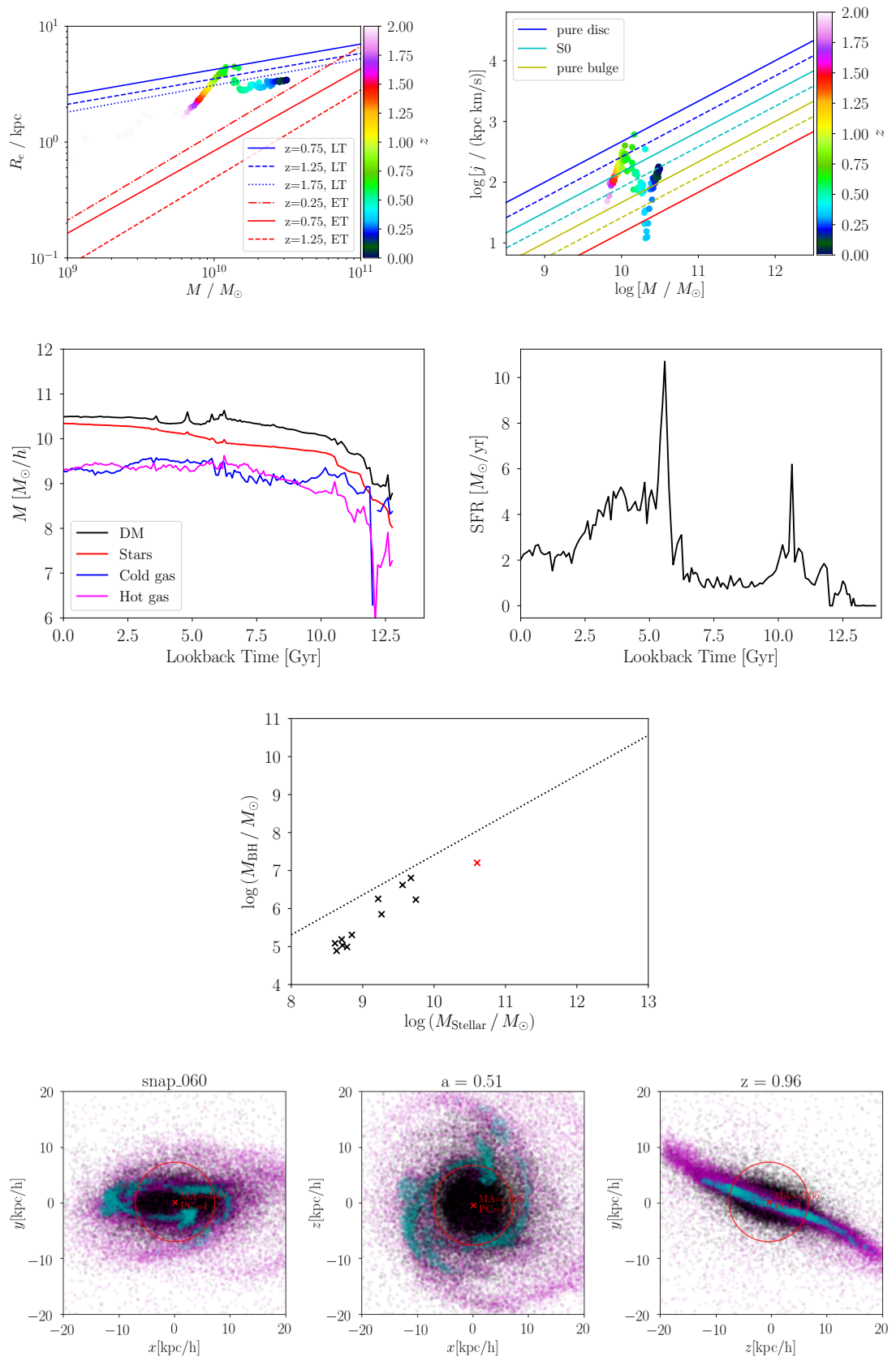
Figure 5.3.: Overview about the properties of the galaxy SIN in the thermal jet mode feedback run. Displayed are the mass-size and $M_{\mathrm{star}} - j_{\mathrm{star}}$ relation (first row), mass accretion history and star formation rate (second row), $M_{\mathrm{star}} - M_{\mathrm{BH}}$ relation (third row), as well as three orthogonal projections of the galaxy at $z \simeq 1$ (fourth row).

5.2.4. Hot Gas Heating Only

In the previous section we constrained the feedback in radio-mode to heat only hot gas, in order to maintain a larger amount of cold gas, especially at small radii. In this run we aim at advancing the improvements of the previous setup and heat *only* hot gas, regardless if black holes accrete in quasar- or radio-mode. This might arguably help to obtain a galaxy with a significant amount of gas, even in the central parts.

An overview about the general properties of the main galaxy is shown in Fig. 5.4. Displayed are the mass-size relation and $M_{star} - j_{star}$ plane (first row), mass accretion history and star formation rate (second row), $M_{BH} - M_{stellar}$ relation (third row), as well as three orthogonal projections of the galaxy at $z \simeq 1$ (fourth row).

In fact, most of the results are similar to the previous run of Sect. 5.2.3. The evolution of the galaxy in the mass-size and $M_{star} - j_{star}$ plane nicely illustrates its evolution from a disc galaxy, through major merger to a typical elliptical. It both fits the expected values for late- and early-type galaxies reasonably well. Similarly, the mass accretion history and evolution of the star formation rate are consistent with those of the previous run. In particular, a significant amount of gas is maintained in the galaxy and likewise a similar amount of hot and cold gas.

More importantly, we find that in a significant portion of the snapshots the interaction radius is very small compared to the previous runs, especially earlier in cosmic history. At lower lookback times, the interaction radius increases but remains small compared to the galaxy itself. Moreover, a considerable amount of cold gas is found within the interaction radius. In fact, this poses a essential improvement to the previous runs. This is further highlighted by the resulting thin disc, remarkable spiral structure, and especially by the formation of a weak, non-persistent bar at higher redshifts.

Nonetheless, I emphasize that this run does not fully resolve the previous problems, as the feedback still tears a small hole in the gas component that might influence developing bars. However, with the present run this issue has been strongly improved. Regardless of these improvements, we continue this parameter study with other tests to better understand the affect of the AGN model on high-resolution galaxies. These studies include methods for variable accretion and feedback factors, as well as the seed black hole mass.
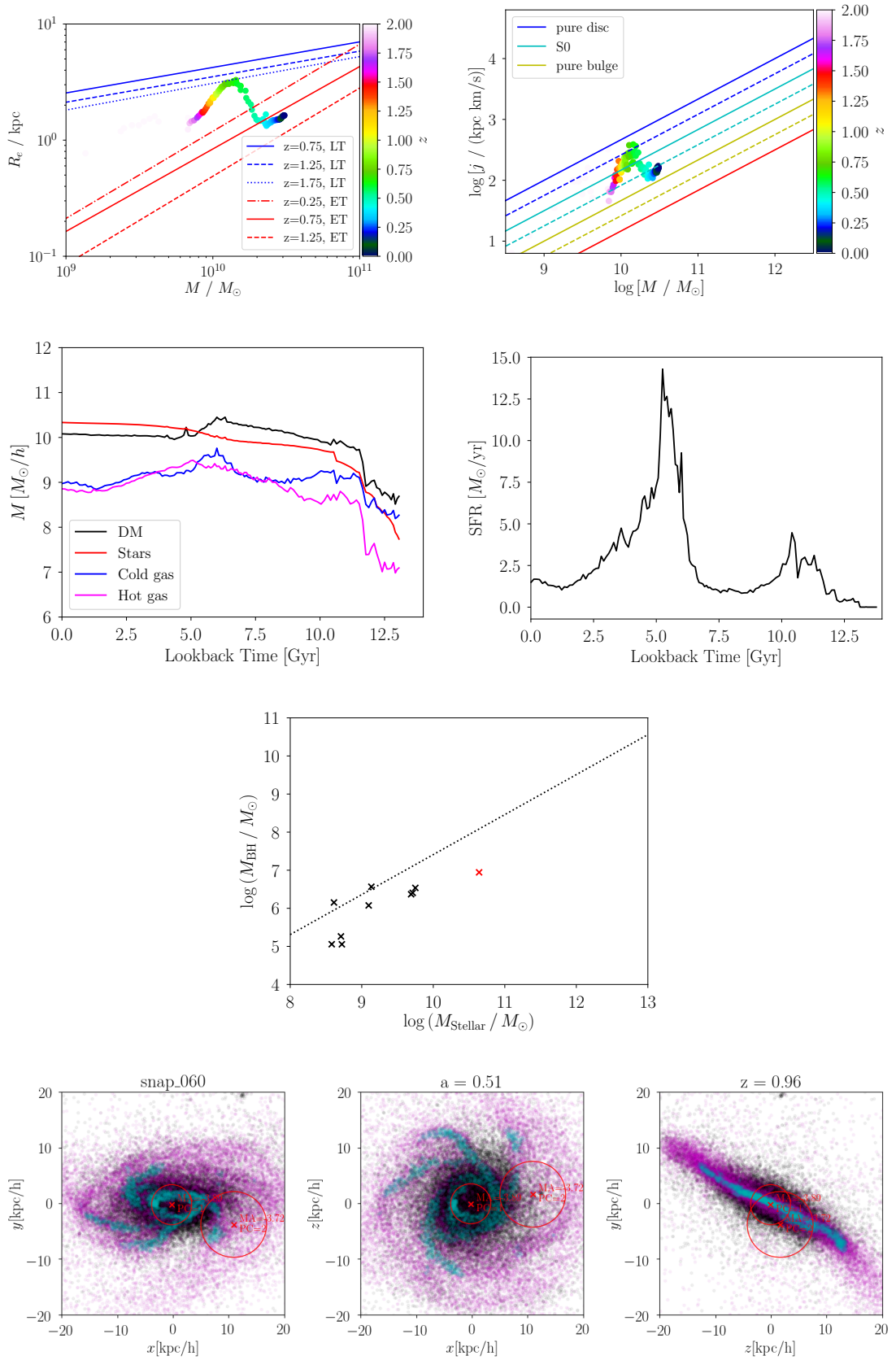
Figure 5.4.: Overview about the properties of the galaxy SIN in the run in which *only* hot gas is heated by AGN feedback. Displayed are the mass-size and $M_{star} - j_{star}$ relation (first row), mass accretion history and star formation rate (second row), $M_{star} - M_{BH}$ relation (third row), as well as three orthogonal projections of the galaxy at $z \simeq 1$ (fourth row).

5.2.5. Variable Accretion Factor

State-of-the-art AGN models typically assume Bondi accretion. To account for the limited resolution of numerical simulations, the resulting Bondi accretion rate is usually multiplied by a constant boost factor α. For instance, Springel (2005) use $\alpha = 100$, whereas Steinborn et al. (2015) use $\alpha = 100$ for cold and $\alpha = 10$ for hot gas. Other authors try to parametrize the boost factor based on density (Booth and Schaye, 2009) or an equilibrium between feedback and cooling (Vogelsberger et al., 2013, see Sect. 5.2.6). With this run, we investigate the effect of the switch `BH_VARIABLE_ACCRETION_FACTOR` which allows a variable boost factor α in GADGET.

An overview about the general properties of the main galaxy is shown in Fig. 5.5. Displayed are the mass-size relation and $M_{\mathrm{star}} - j_{\mathrm{star}}$ plane (first row), mass accretion history and star formation rate (second row), $M_{\mathrm{BH}} - M_{\mathrm{stellar}}$ relation (third row), as well as three orthogonal projections of the galaxy at $z \simeq 1$ (fourth row).

The galaxy in this run lies slightly below the expected mass-size relation for disc galaxies. A similar result is found for the $M_{\mathrm{star}} - j_{\mathrm{star}}$ plane in which the galaxies occupies b-values more similar to S0/spheroidal galaxies. The mass accretion history shows that the entire gas component of the galaxies is removed at $10\,\mathrm{Gyr}$ and cannot be recovered till the end of the simlation run at $5\,\mathrm{Gyr}$. Consequently, the stellar mass is constant at $\sim 6 \times 10^9\,\mathrm{M_\odot}$ throughout this range in time. This is consistent with a star formation rate of $0\,\mathrm{M_\odot/\,yr}$. However, the galaxies in this run follow the $M_{\mathrm{BH}} - M_{\mathrm{stellar}}$ relation well.

The interaction radius of a black hole particle refers to the radius within the black hole interacts with the surrounding particles through accretion and feedback. In this run, the interaction radius becomes unreasonably large compared to the size of the galaxy. As the interaction radius increases, the gas is pushed outwards and once the interaction radius exceeds the size of the galaxy, the entire gas content of the galaxy is removed. Therefore the star formation rate is suppressed, the stellar mass of the galaxy constant, and no significant morphological features form. This effect is an extreme case of the holes in the gas component observed in the previous runs (see e.g. Sect. 5.2.2).

The resulting galaxy is unrealistic and I point out that too large interaction radii have to be avoided or the AGN model needs to be suitably adapted. Thus, the switch `BH_VARIABLE_ACCRETION_FACTOR` is not used in the following parameter tests.
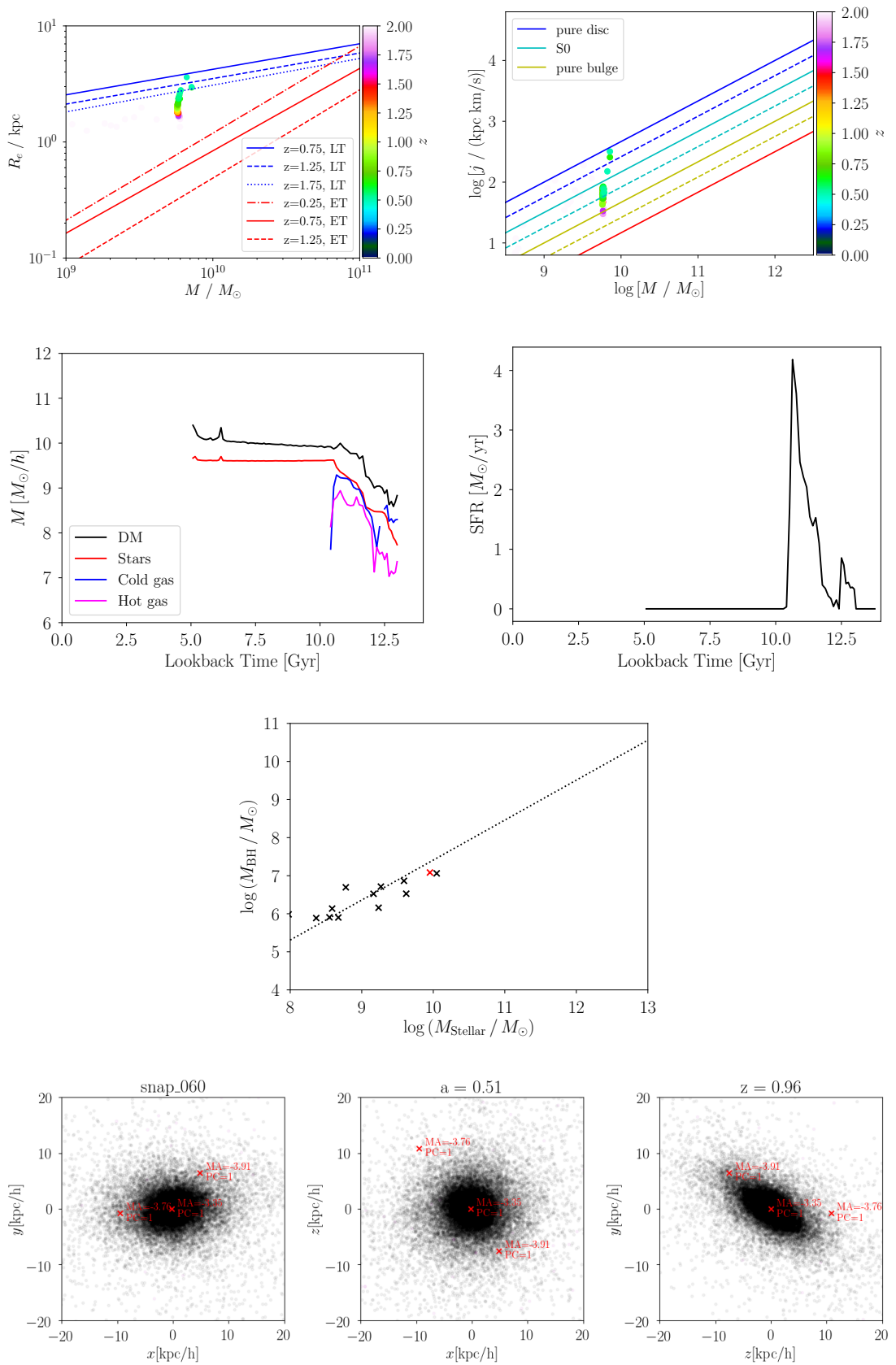
Figure 5.5.: Overview about the properties of the galaxy SIN in the run with a variable accretion factor. Displayed are the mass-size and $M_{star} - j_{star}$ relation (first row), mass accretion history and star formation rate (second row), $M_{star} - M_{BH}$ relation (third row), as well as three orthogonal projections of the galaxy at $z \simeq 1$ (fourth row).

5.2.6. Pressure Dependent Accretion

Vogelsberger et al. (2013) argues that the black hole accretion model might significantly overestimate the accretion rate if the black hole is not embedded in cold, star-forming gas. More specifically, this is the case if the black hole has a large mass and is surrounded by low-density gas. As a result of this, a hot bubble with unphysically low density can be generated around the black hole. To avoid this, Vogelsberger et al. (2013) introduce a correction for pressure dependent accretion. The following explanation follows his discussion.

If the AGN feedback energy balances the cooling losses in the bubble, the bubble is in a quasi-stationary state. Thus, one can define an equilibrium thermal energy per unit mass u_{eq} and thereby a reference pressure

$$P_{\mathrm{ref}} = (\gamma - 1)\rho_{\mathrm{sfr}} u_{\mathrm{eq}} \qquad (5.4)$$

with the star formation threshold ρ_{sfr}. If the external gas pressure P_{ext} is lower than the reference gas pressure P_{ref}, the accretion rate is lowered by a factor of $(P_{\mathrm{ext}}/P_{\mathrm{ref}})^2$. For very hot gas, the temperature in the bubble will be reduced by $(P_{\mathrm{ext}}/P_{\mathrm{ref}})$ and the density increased by $(P_{\mathrm{ref}}/P_{\mathrm{ext}})$. However, the accretion rate experiences only marginal changes. Vogelsberger et al. (2013) conclude that this scheme does not influence the self-regulated growth of black holes while suppressing the generation of large bubbles around black holes.

This scheme for pressure dependent accretion (implemented in the switch `LB_PRESSURE_DEPENDENT_ACCRETION`) has been applied to the Zoom-Simulations with and without the advanced AGN feedback model from Steinborn et al. (2015). In both the *25x* and *250x* resolution levels, the pressure threshold was only exceeded in a few timesteps. I conclude that the pressure dependent accretion scheme has no influence on the galaxies in the Zoom-Simulations. Thus, the scheme is not used for the rest of this study.

5.2.7. Black Hole Feedback Factor

The black hole feedback factor (parameter `BlackHoleFeedbackFactor`) defines what fraction of radiation from the AGN is coupled to the surrounding matter (Steinborn et al., 2015). Thus, this factor serves, to some extent, as a regulator for the strength of the feedback. Therefore, I have conducted multiple runs with feedback factors of 0.050, 0.010, 0.005 and 0.001. Interestingly, no significant differences in the properties of the resulting galaxies could be found. Eventually, we choose a feedback factor of 0.005 for all simulation runs in this study, unless stated otherwise.

5.2.8. Seed Black Hole Mass

In previous runs of this parameter study, it was not possible to reproduce the $M_{\mathrm{BH}} - M_{\mathrm{stellar}}$ relation very well. The black holes in theses simulations have systematically too low masses and thus, are lying below the $M_{\mathrm{BH}} - M_{\mathrm{stellar}}$ relation. In order to address this problem and properly reproduce this relation, I conduct a simulation run with an increased black hole seeding mass of $5 \times 10^5 \, \mathrm{M_\odot}$ instead of $5 \times 10^4 \, \mathrm{M_\odot}$ both with and without the thermal jet mode feedback module (see Sect. 5.2.3). This implies that black holes are created closer to the $M_{\mathrm{BH}} - M_{\mathrm{stellar}}$ relation and do not need to accrete as much mass to reach the $M_{\mathrm{BH}} - M_{\mathrm{stellar}}$ relation (see discussions above).

An overview about the general properties of the main galaxy is shown in Fig. 5.6. Displayed are the mass-size relation and $M_{\mathrm{star}} - j_{\mathrm{star}}$ plane (first row), mass accretion history and star formation rate (second row), $M_{\mathrm{BH}} - M_{\mathrm{stellar}}$ relation (third row), as well as three orthogonal projections of the galaxy at $z \simeq 1$ (fourth row).

The mass-size evolution of the galaxy is in reasonable agreement with the expected mass-size relation of disc galaxies. However, there is a large scatter in the b-value of this galaxy. The total stellar mass of the system is roughly constant from $10 \, \mathrm{Gyr}$ lookback time onwards. The cold gas content is decreasing from $10 \, \mathrm{Gyr}$ to $7.5 \, \mathrm{Gyr}$. At later times, neither hot nor cold gas is present in the galaxy anymore. This is consistent with a star formation rate of $\leq 1 \, \mathrm{M_\odot / \, yr}$ from $10 \, \mathrm{Gyr}$ onwards, and a star formation rate of $\simeq 0 \, \mathrm{M_\odot / \, yr}$ from $7.5 \, \mathrm{Gyr}$ on. Interestingly, the galaxies in this run fit the $M_{\mathrm{BH}} - M_{\mathrm{stellar}}$ relation very well, including the main halo marked by a red cross in Fig. 5.6.

In this simulation run the interaction radius becomes unreasonably large as compared to the size of the galaxy itself. It first expands to radii similar to the radius of the galaxy (see Fig. 5.6), before expanding to radii larger than the galaxy so that the entire gas content of the galaxy is removed (see Fig. 5.7). As a result of this, the star formation rate is suppressed to $\simeq 0 \, \mathrm{M_\odot / \, yr}$ and the stellar mass of the galaxy remains constant over most of the simulation. In addition, any typical morphological features, such as for instance spiral arms, cannot form anymore. Interestingly, the resulting galaxies fit the $M_{\mathrm{BH}} - M_{\mathrm{stellar}}$ relation very well, although their appearance is unrealistic.

When conducting this run together with the thermal jet mode feedback module (see Sect. 5.2.3), similar results are found. The increase of the black hole interaction radius is also observed, although this effect seems to occur earlier and more abrupt in cosmic history. This is for instance indicated by the mass accretion history which shows that the entire gas content of the galaxy is already removed at a lookback time of $10 \, \mathrm{Gyr}$ (see Fig. 5.8). The other relevant parameter look similar in the run with and without thermal jet mode feedback.
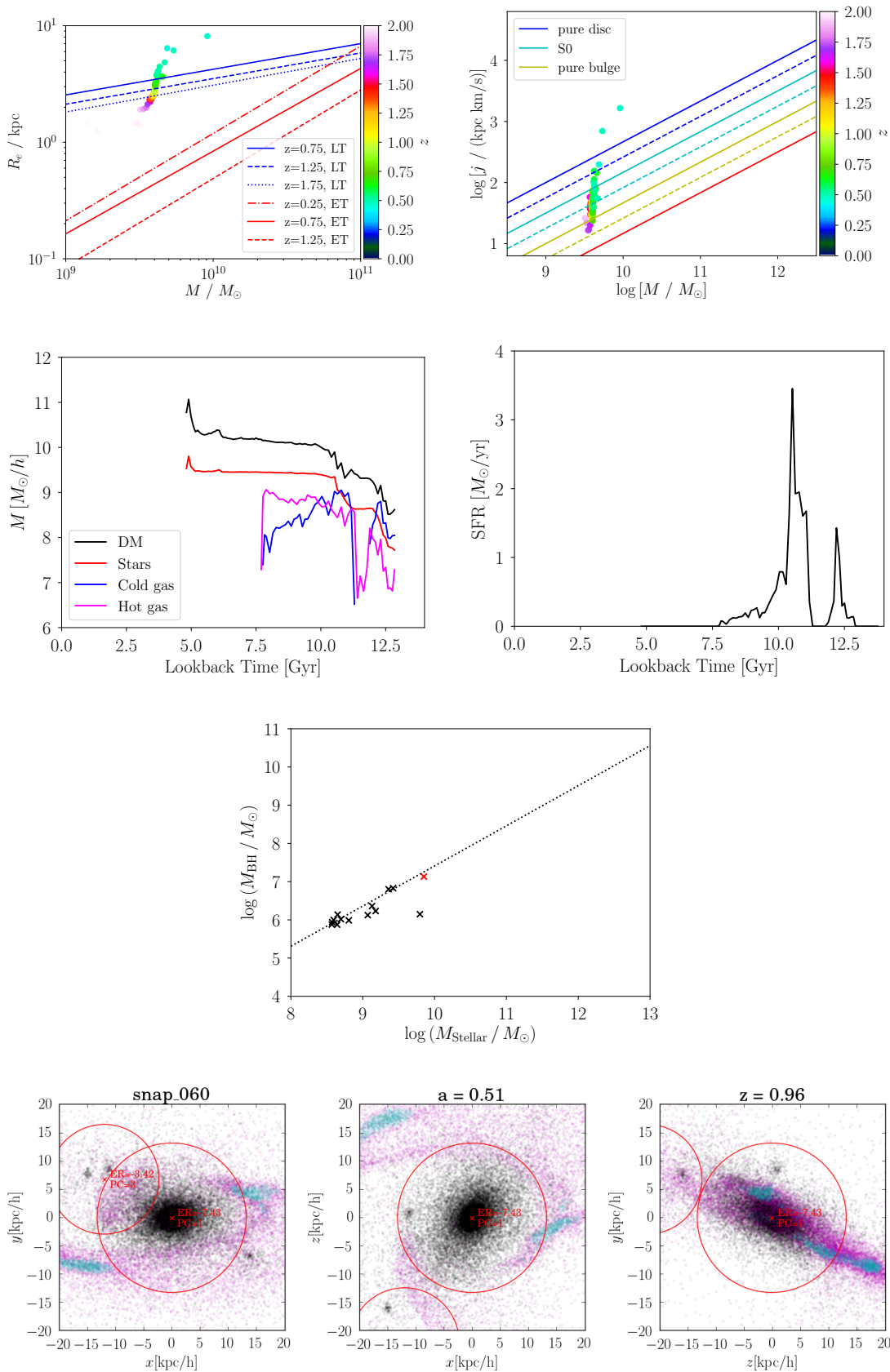
Figure 5.6.: Overview about the properties of the galaxy sin in the run with a seed black hole mass of $5 \times 10^5 \, M_\odot$ and without thermal jet mode feedback. Displayed are the mass-size and $M_{star} - j_{star}$ relation (first row), mass accretion history and star formation rate (second row), $M_{star} - M_{BH}$ relation (third row), as well as three orthogonal projections of the galaxy at $z \simeq 1$ (fourth row).
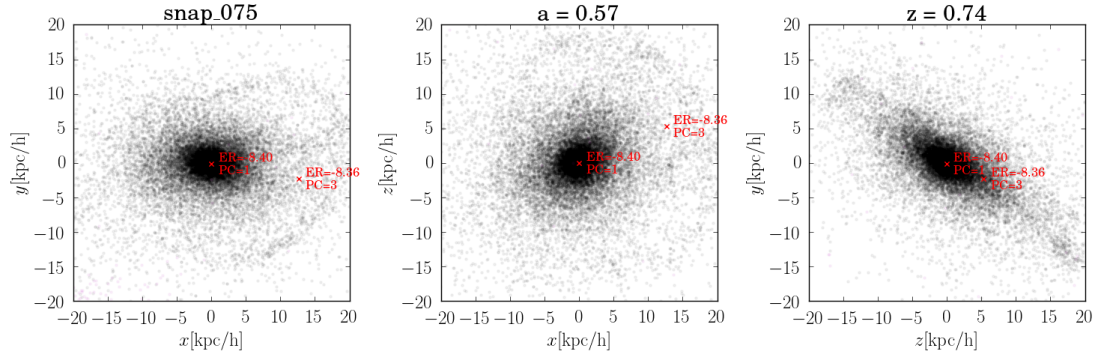
Figure 5.7.: Three orthogonal projections of the galaxy at $z = 0.74$. The black hole interaction radius is larger than the field-of-view. The entire gas content of the galaxy has been removed by the AGN feedback.
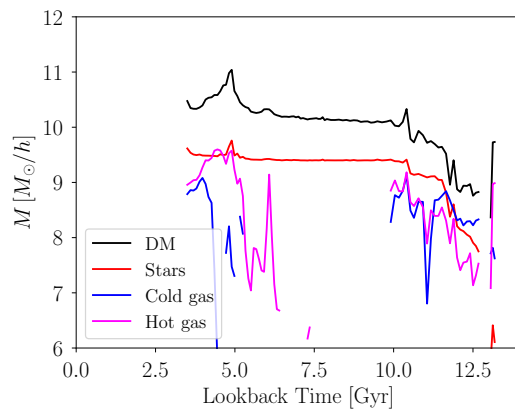

Figure 5.8.: Mass accretion history for in the run with a black hole seed mass of $5 \times 10^5 \, \mathrm{M}_\odot$ and the thermal jet mode feedback model.

5.2.9. Black Hole Neighbour Factor

The `BlackHoleNgbFactor` influences the number of neighbouring SPH particles that are considered for accretion onto the black hole and the deposition of feedback energy. Thus, the `BlackHoleNgbFactor` has crucial influence on the calculation of the black hole interaction radius. At higher resolutions more particles are in the direct vicinity of the black hole and thus the AGN model considers only smaller interaction radii as compared to lower resolution levels. Therefore, more particles leave/enter this radius per timestep and particles arguably receive the energy feedback only once. In contrast, if a larger interaction radius would be used, a lower number of particles leave/enters this volume and particles are expected to receive feedback multiple times. Thus, an increase of the `BlackHoleNgbFactor` might increase the influence of the black hole and its accretion and therefore result in galaxies with a realistic $M_{\mathrm{BH}} - M_{\mathrm{stellar}}$ relation. In this parameter test we conduct a simulation run with a `BlackHoleNgbFactor` of 10 instead of 1.

An overview about the general properties of the main galaxy is shown in Fig. 5.9. Displayed are the mass-size relation and $M_{\mathrm{star}} - j_{\mathrm{star}}$ plane (first row), mass accretion history and star formation rate (second row), $M_{\mathrm{BH}} - M_{\mathrm{stellar}}$ relation (third row), as well as three orthogonal projections of the galaxy at $z \simeq 1$ (fourth row).

From a visual inspection of the galaxies in all snapshots it is obvious that the black hole interaction radius becomes significantly larger than the size of the galaxy as soon as the black hole is seeded. Similarity to the previous run (see Sect. 5.2.8) the entire gas content of the galaxy is removed and no striking morphological features are formed. Consistent with this finding, the star formation rate is suppressed to $0 \, \mathrm{M_\odot / \, yr}$ throughout cosmic history with a short peak of $1.2 \, \mathrm{M_\odot / \, yr}$ at $\sim 12 \, \mathrm{Gyr}$. As a result of this, the stellar mass is constant in the merger-free phase from 10 to $5 \, \mathrm{Gyr}$. However, the main galaxies fits the $M_{\mathrm{BH}} - M_{\mathrm{stellar}}$ relation perfectly, although other galaxies in this run seem to be slightly to massive to fit the sequence.

Although an increased `BlackHoleNgbFactor` and thus an increased interaction radius do produce galaxies that fit the $M_{\mathrm{BH}} - M_{\mathrm{stellar}}$ relation better, the resulting galaxies are not realistic. Any gaseous component is removed, star formation suppressed and no morphological features are observable. Therefore I conclude to continue this study with a `BlackHoleNgbFactor` of 1.

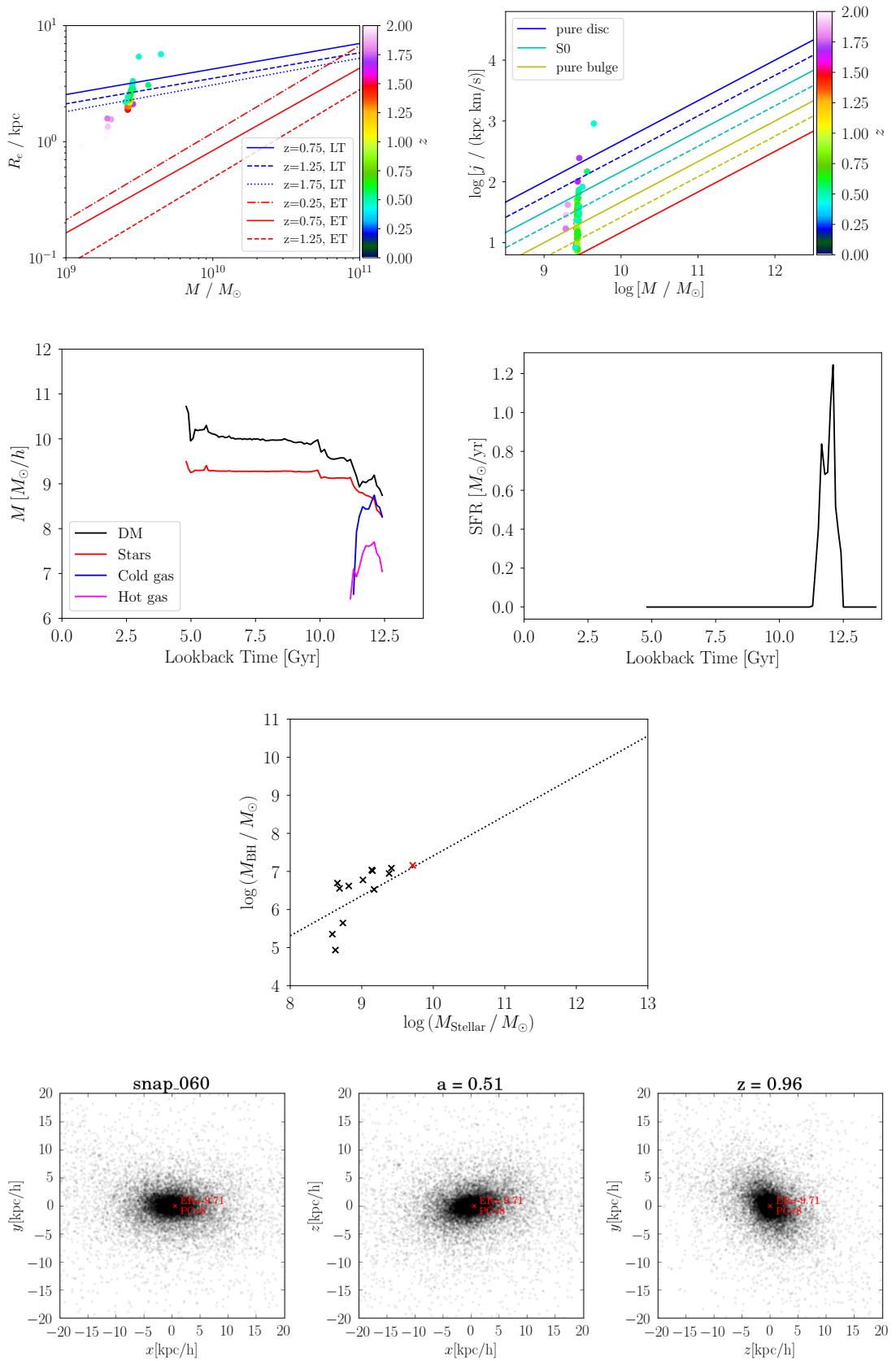**Figure 5.9.:** Overview about the properties of the galaxy SIN in the run with a `BlackHoleNgbFactor` of 10. Displayed are the mass-size and $M_{\mathrm{star}} - j_{\mathrm{star}}$ relation (first row), mass accretion history and star formation rate (second row), $M_{\mathrm{star}} - M_{\mathrm{BH}}$ relation (third row), as well as three orthogonal projections of the galaxy at $z \simeq 1$ (fourth row).

5.3. Summary of Parameter Tests

The comprehensive parameter study presented in this chapter does highlight the importance of feedback processes, in particular AGN feedback, for galaxies. I have tested various different options and demonstrated their influence on the resulting galaxies in the Zoom-Simulations.

In general, we obtain disc galaxies which occupy realistic locations in both the mass-size and $M_{\mathrm{star}} - j_{\mathrm{star}}$ plane. In addition, these galaxies have notably thin discs and various morphological components. This includes bulges, bars, discs, and also spirals arms of distinct spiral arm classes.

However, most galaxies lie slightly below the $M_{\mathrm{BH}} - M_{\mathrm{stellar}}$ relation, which is justifiable for the late-type galaxies on hand. Nonetheless, in most runs the AGN feedback does generate holes in the gas component at small radii. The radius of these holes coincides with the interaction radius. Thus, it seems that the feedback does exert a too large pressure on the gas so that it is removed from the centre of the galaxy. In fact, this is a significant problem as it suppresses the formation of structures, such as bars, in these regions of the galaxies.

However, this issue could mostly be resolved in the run in which the AGN feedback does only heat hot gas (see Sect. 5.2.4). In this run a notably small interaction radius and an essential amount of cold gas within the interaction radius is found while other galaxy properties could be successfully reproduced. This represents an essential improvement and is further illustrated by the formation of a weak, non-persistent bar in this simulation run. We conclude that this AGN setup, together with the black hole merger treatment discussed in Sect. 4, does produce the most realistic disc galaxies and will be denoted as final configuration.

One approach to further improve the feedback processes may be connected to a more detailed investigation of the stellar feedback processes. Another approach may be the development of a new AGN model, which does not depend on an accretion radius but calculates accretion/feedback that depends on the properties of each individual gas particle. However, these investigations are beyond the scope of this study.

6. Summary and Conclusions

Numerical simulations are an invaluable tool in astrophysics, in particular when investigating structure and evolution of disc galaxies. However, cosmological simulations cannot properly resolve the internal structure of disc galaxies, while simulations of individual galaxies suffer from the absence of a realistic galaxy setup and environment.

Cosmological Zoom-Simulations can avoid these disadvantages and have thus been used to resimulate structures at all scales, ranging from superclusters, clusters and groups down to large elliptical galaxies. In this study, we aim at extending this resolvable mass range down to and even beyond Milky-Way-like disc galaxies. This way we finalize the existing set of Zoom-Simulations which then spans a range in mass from 10^{11} to $10^{15}\,\mathrm{M_\odot}$.

In contrast to other studies, our simulations are based on a $1\,\mathrm{Gpc\,h^{-1}}$ sized cosmological box. Although this increases the complexity of resolving low-mass galaxies due to the low resolution of the parent simulation, it allows to choose objects from a large variety of cosmological environments that are not contained in smaller boxes. In fact, this permits the resimulation of objects that have very specific configurations but formed self-consistently within their cosmological ecosystem.

To this end, significant improvements of previous simulation setups are necessary, not only due to the very high resolutions of our Zoom-Simulations but also because of the small masses of the galaxies themselves. This includes the generation of zoomed initial conditions at increasingly high resolutions and redshifts, the readjustment of AGN feedback models as well improvements of the black hole merger processes.

Latter implementations are discussed in Chapter 4. We review the preconditions for black hole mergers and adapt the corresponding parameters in such a way that a realistic black hole merger timescale is obtained. In contrast to other simulations, the black holes are not tied to the potential minimum of the individual galaxies. This makes it necessary to merge black holes in such a way that they stay in the centre of the merger remnant self-consistently. We conclude that this is best achievable by merging all black holes onto the black hole that is most bound within the potential. Previous implementations, such as swallowing by mass or particle ID, have been proven inoperable in the context of Zoom-Simulations. Furthermore, we point out that if the momentum transfer from accreted gas onto the accreting black hole is taken into account, the black hole is significantly displaced from the galaxy centre.

In Chapter 5 I conduct a comprehensive parameter study to investigate the behaviour of the AGN model, in particular to quantify the influence of various additional modules. We find that runs without AGN feedback do not result in realistic disc galaxies. Runs with AGN feedback do result in galaxies which occupy plausible locations in the mass-size and $M_{star} - j_{star}$ plane, although these galaxies lie slightly below the $M_{BH} - M_{stellar}$ relation. Latter fact might be justifiable, as we consider only late-type galaxies in this study. The best results were obtained by constraining the feedback in such a way that only hot gas is heated, regardless if black holes accrete in quasar- or radio-mode. I further highlight the thin structure of their discs and various morphological features, including bulges, bars, discs, and spiral arms of different spiral arm classes.

In summary, we have extended the existing set of Zoom-Simulations even beyond Milky-Way-like disc galaxies and proven that it is possible to resolve galaxies with masses as low as $10^{11}\,M_{\odot}$ from a $1\,Gpc\,h^{-1}$ sized cosmological box. Our results will allow detailed studies of galactic structure and its interplay with the cosmological environment. This will include the formation and evolution of bars and spiral structure, the spatial distribution of metals in galaxies, and we further expect to resolve globular star clusters. These efforts will strongly profit from the *2500x* resolution level which will be used in the next production runs.

Finally, in the Appendix I present the results of two observational endeavours. I review the main results of a study conducted at the European Southern Observatory in Santiago de Chile under the supervision of Dr. Dimitri Gadotti. In this study we investigate how fundamental galaxy properties relate to the properties of their spiral arms. In addition, I show the main features of an IFU data analysis pipeline which I developed at the Instituto de Astrofísica de Canarias under the supervision of Dr. Jesus Falcon-Barroso. This pipeline extracts stellar and gas kinematics as well as stellar population properties and will be the main analysis pipeline of various collaborations.

A. Observational Results

From April to September 2016 I conducted a research internship at the European Southern Observatory (ESO) in Santiago de Chile under supervision of Dr. Dimitri A. Gadotti. We made use of infrared images from the Spitzer Survey of Stellar Structure in Galaxies (S^{4}G) and other previously published measurements to investigate the relation of spiral arm classes with other fundamental galaxy properties. The results of this study have already been published in the Monthly Notices of the Royal Astronomical Society, Volume 471, Issue 1, 11 October 2017, Pages 1070–1087. In this appendix I present abstract and conclusion of this publication. Naturally, references herein refer to the paper itself.

The results presented below should be understood as complementary approach to the simulations presented in the main part of this thesis. For instance, this allows an extensive comparison of spiral structure, its amplitudes, geometrical properties and levels of symmetry found in our Zoom-Simulations with observations.

How do spiral arm contrasts relate to bars, disc breaks and other fundamental galaxy properties?

Adrian Bittner,[1,2] Dimitri A. Gadotti,[1] Bruce G. Elmegreen,[3] Evangelie Athanassoula,[4] Debra M. Elmegreen,[5] Albert Bosma,[4] Juan-Carlos Muñoz-Mateos[1]

[1]European Southern Observatory, Casilla 19001, Santiago 19, Chile
[2]University Observatory Munich, Scheinerstr. 1, 81679 Munich, Germany
[3]IBM Research Division, T.J. Watson Research Center, Yorktown Heights, NY 10598, USA
[4]Aix Marseille Univ, CNRS, LAM, Laboratoire d'Astrophysique de Marseille, Marseille, France
[5]Vassar College, Dept. of Physics and Astronomy, Poughkeepsie, NY 12604, USA

ABSTRACT

We investigate how the properties of spiral arms relate to other fundamental galaxy properties, including bars and disc breaks. We use previously published measurements of those properties, and our own measurements of arm and bar contrasts

for a large sample of galaxies, using 3.6μm images from the Spitzer Survey of Stellar Structure in Galaxies (S^{4}G). Flocculent galaxies are clearly distinguished from other spiral arm classes, especially by their lower stellar mass and surface density. Multi-armed and grand-design galaxies are similar in most of their fundamental parameters, excluding some bar properties and the bulge-to-total ratio. Based on these results, we revisit the sequence of spiral arm classes, and discuss classical bulges as a necessary condition for standing spiral wave modes in grand-design galaxies. We find a strong correlation between bulge-to-total ratio and bar contrast, and a weaker correlation between arm and bar contrasts. Barred and unbarred galaxies exhibit similar arm contrasts, but the highest arm contrasts are found exclusively in barred galaxies. Interestingly, the bar contrast, and its increase from flocculent to grand-design galaxies, is systematically more significant than that of the arm contrast. We corroborate previous findings concerning a connection between bars and disc breaks. In particular, in grand-design galaxies the bar contrast correlates with the normalised disc break radius. This does not hold for other spiral arm classes or the arm contrast. Our measurements of arm and bar contrast and radial contrast profiles are publicly available.

Summary and Conclusions

We investigated how fundamental galaxy properties, including the properties of bars and disc breaks, are related to the properties of spiral arms. Using 3.6μm images from the Spitzer Survey of Stellar Structure in Galaxies (S^{4}G), we performed measurements of arm-interarm and bar-interbar contrasts and also considered previously published measurements of fundamental galaxy parameters, including visual classification into the three different arm classes (flocculent, multi-armed and grand-design). The main results from this study can be summarised as follows:

(i) Our measurements of the arm-interarm contrast compare well with the results of a previous study, with typical differences of approximately 25%. We discuss differences in the measurement methods and point out striking similarities in the resulting radial contrast profiles. Thus we conclude that the measurements of both studies are in reasonable agreement (see Sect. 4.2).

(ii) The arm contrasts of flocculent galaxies are significantly lower as compared to the other spiral arm classes. However, the arm contrasts of multi-armed and grand-design galaxies are more similar than expected from a visual classification. Interestingly, the bar contrast, and its increase from flocculent to grand-design galaxies, is systematically more significant as compared to the arm contrast (see Fig. 11).

(iii) Flocculent galaxies are clearly distinguished from the other spiral arm classes, in particular by their lower total stellar masses and surface densities. In contrast, multi-armed and grand-design galaxies share many fundamental parameters, excluding some bar properties and the bulge-to-total luminosity

ratio. In particular, almost all flocculent galaxies either have no bulge or have extended, less massive (possibly disc-like) bulges whereas grand-design and multi-armed galaxies tend to have more classical-type bulges with slightly more massive bulges in the grand-design spirals (see Sect. 3).

(iv) Considering multi-armed and grand-design galaxies, a strong correlation between the bulge-to-total ratio and the bar contrast is found and we conclude that the existence of a classical bulge could enhance bar evolution. In addition, a weaker correlation between arm and bar contrast is found which corroborates the findings of previous studies (see Fig. 12).

(v) Similar arm-interarm contrasts are detected in both barred and unbarred galaxies (see Fig. 13). This indicates that spiral arms have the capacity to reach similar arm contrasts regardless of which mechanism triggers the spiral structure. However, the highest arm contrasts are found exclusively in barred galaxies.

(vi) We show that the bar contrast of grand-design galaxies correlates with the disc break radius, reinforcing previous conclusions on the connection between bars and disc breaks. However, such correlation is absent for the arm contrast or the other spiral arm classes (see Sect. 5.2).

Our measurements of the arm and bar contrasts as well as the corresponding radial contrast profiles are available to the community at `http://homepages.physik.uni-muenchen.de/~a.bittner/projects/arm_contrasts/overview.html`.

B. IFU Data Analysis Pipeline

In this appendix, I describe the outcome of my scientific visit at the Instituto de Astrofísica de Canarias in Tenerife during which I was hosted by Dr. Jesus Falcon-Barroso. I review the preparation of IFU data (see Sect. B.2), the extraction of stellar kinematics (see Sect. B.3) as well as gas kinematics (see Sect. B.4), and stellar population properties (see Sect. B.5). Next, I introduce a sophisticated IFU data analysis pipeline which was developed during this scientific visit. Finally, I highlight advantages of this code such as a data visualization tool, and discuss its applications in future studies (see Sect. B.6). This subproject complements the conducted Zoom-Simulations, as it provides high resolution observations of stellar and gas kinematics as well as stellar population properties of Milky-Way-like disc galaxies in the local Universe.

B.1. Introduction

During the last decades, long-slit spectroscopy has proven to be an important tool to obtain spatially resolved spectroscopic observations and helped to understand the kinematics of galaxies. However, integral-field spectroscopic (IFU) observations provide a more efficient way to obtain these kinds of observations, as an IFU collects spectra over the entire field-of-view simultaneously. Even though the first IFUs were already developed in the 90's (e.g. Bacon et al., 1995), the first extensive project to make use of these instruments in the context of galaxies was the SAURON project (Bacon et al., 2001; de Zeeuw et al., 2002). While exploiting a representative sample of 72 galaxies, the SAURON project provides comprehensive studies on the stellar and gas kinematics (e.g. Emsellem et al., 2004; Sarzi et al., 2006; Falcón-Barroso et al., 2006; Ganda et al., 2006) as well as on stellar population properties (Kuntschner et al., 2010; Peletier et al., 2007) of galaxies. For instance, this project lead to the discovery of slow and fast rotating subgroups in early-type galaxies (Emsellem et al., 2007). (Falcón-Barroso et al., 2017)

Eventually, other IFU surveys continued these investigations: The ATLAS[3D] survey (Cappellari et al., 2011) further explored the properties of early-type galaxies, while the CALIFA survey (Sánchez et al., 2012) investigates a sample of 600 galaxies of all morphological types. In fact, the CALIFA projects provides a unique combination of spatial sampling ($\sim 1\,\mathrm{kpc}$) and coverage (1.8-3.7R$_e$) (Falcón-Barroso et al., 2017).

The MaNGA survey (Bundy et al., 2015) aims to conduct IFU observations for 10 000 galaxies in the local Universe (Falcón-Barroso et al., 2017).

Upcoming projects will profit from the revolutionary MUSE (Multi-Unit Spectroscopic Explorer) instrument, which is a second-generation instrument installed on ESO's Very Large Telescope (Bacon et al., 2010). The unique capabilities of MUSE, such as its large field-of-view, sensitivity, wavelength range as well as spectral and spatial resolution, together with the ground layer adaptive optics facility at Paranal Observatory will allow to study the formation and evolution of galaxies in unprecedented detail. The potential of MUSE has already been proven during its first years of operation (see e.g. Emsellem et al., 2014; Gadotti et al., 2015).

One of the projects using this instrument is TIMER ("Time Inference with MUSE in Extragalactic Rings"; see Gadotti et al., 2018, in prep.) which aims at studying the inner parts of disc galaxies. In particular, it aims at decomposing galaxies into their distinct structural components (such as discs, bars, spheroids and rings) and uncovering the processes that dominated their formation and evolution. The ultimate goal of this projects is to reconstruct the entire evolutionary history of the galaxies by connecting the histories of their structural components and the related secular evolution processes. The TIMER project e.g. aims at measuring the time in cosmic history when bars first started to form and therewith to put secular evolution in a larger cosmological context (see also Gadotti et al., 2015).

B.2. Preparatory Steps

This pipeline aims at extracting stellar and gas kinematics as well as stellar population properties from IFU-cubes. To this end, several preparatory steps are necessary to prepare the data for the actual measurements. The pipeline is equipped with a routine to read in data from the MUSE integral field spectrograph. Thanks to the modularised implementation of this read-in routine, it is easy to add additional routines for other IFU instruments which are automatically detected and used by the code. Thus, the software is capable of analysing data from any IFU instrument. The spectra are then logarithmically rebinned in order to convert the spectra from wavelength to velocity space. In addition, spectra can be shortened to the most useful spectral range. Although this reduces the available information in the spectra, it can save considerable computational costs in the subsequent analysis. Thus, depending on the properties of the galaxy in consideration and the objective of the study, a shortening of the spectra should be considered. (Falcón-Barroso et al., 2017)

We further implement a minimum signal-to-noise (S/N) threshold for every spectrum, as the consideration of low-quality spectra might introduce spurious effects in the analysis, especially in the measurement of the stellar kinematics. Naturally,

this S/N threshold is of particular importance in low surface brightness regions, e.g. the outskirts of galaxies. As these regions might still be of interest for the extraction of gas kinematics (due to the presence of e.g. planetary nebulae), the pipeline provides an option to consider all spatial pixels regardless of their S/N. (Falcón-Barroso et al., 2017)

The S/N ratio is not a limiting factor for the extraction of radial velocity and velocity dispersion from the line-of-sight velocity distribution. However, it was shown that the higher order moments require a high S/N ratio in order to be measured precisely (van der Marel and Franx, 1993; Gadotti and de Souza, 2005). Thus, we apply the Voronoi binning method of Cappellari and Copin (2003) to generate spatial bins with constant S/N throughout the field. This methods also allows pixels with particular high S/N ratio (e.g. in the central regions of galaxies) to remain unbinned. (Falcón-Barroso et al., 2017)

Spectral templates are prepared in a similar fashion. The templates are logarithmically rebinned, shortened to the same spectral range as the observed spectra, and their spectral resolution adapted to match the resolution of the observed spectra.

B.3. Stellar Kinematics

We extract the line-of-sight velocity distribution (hereafter LOSVD) by using the penalized pixel-fitting method (PPXF) as introduced in Cappellari and Emsellem (2004) and advanced in Cappellari (2017) (see also Emsellem et al., 2004; Gadotti et al., 2015, and references therein). The LOSVD is described by a Gauss-Hermite parametrization (Gerhard, 1993; van der Marel and Franx, 1993)

$$\mathcal{L}(v) = \frac{e^{-(1/2)y^2}}{\sigma\sqrt{2\pi}} \left[1 + \sum_{m=3}^{M} h_m H_m(y) \right] \tag{B.1}$$

with the Hermite polynomials H_m and $y = (v-V)/\sigma$ and provides a measure for the radial velocity v, velocity dispersion σ, and higher order moments h_m (Cappellari and Emsellem, 2004). The higher order moment h_3 describes asymmetric deviations from a pure Gaussian LOSVD (skewness of the distribution) whereas h_4 describes symmetric deviations (kurtosis of the distribution). In addition, these higher order moments contain valuable information about the orbital structure of the stellar system. For example, an anti-correlation between v and h_3 indicates circular motion while a superposition of multiple different LOSVD results in high values of h_4 (see Bender et al., 1994; Gadotti et al., 2015, and references therein).

In principle, the PPXF method convolves a template stellar spectrum with a LOSVD to generate the best possible fit to the observed galaxy spectrum. However, there are two critical issues in this procedure: The selection of optimal templates and the

reliable determination of the higher order moments (see Emsellem et al., 2004, for a more detailed discussion).

As PPXF is sensitive to a mismatch between the observed and template spectrum, it is necessary to use a comprehensive template library which covers a large range of metallicities and ages. For this pipeline we use the MILES single stellar population (SSP) model spectra (Vazdekis et al., 2010) by default. However, other template spectra can be inserted easily. Moreover, PPXF also uses an additive Legendre polynomial in order to adjust the shape of the templates and avoid unphysical large-scale deviations (Emsellem et al., 2004).

As discussed before, the S/N is not an important constraint for the extraction of v and σ. However, in order to determine the higher order moments, in particular at small velocity dispersions, the S/N becomes a limiting factor. In this undersampled regime the parameters cannot be derived simultaneously, at least not without introducing a large scatter. Thus it is advantageous to reduce the parametric description of the LOSVD to a pure Gaussian where necessary. This has been implemented in the *penalized* pixel-fitting routine by Cappellari and Emsellem (2004) in a statistically justified way (Emsellem et al., 2004).

B.4. Gas Kinematics

In order to measure gas kinematics, de Zeeuw et al. (2002) uses residual spectra which are calculated by subtracting the best-fit spectrum, as obtained through PPXF (see Sect. B.3), from the observed spectrum. However, the extraction of stellar kinematics with PPXF requires to mask spectral regions with emission features. In fact, for galaxies with significant emission features the information in the emission-free part of the spectrum might not be sufficient to confine the stellar population properties. This is particularly problematic if emission features are found near metallicity or age sensitive absorption features and thus included in the masked spectral region. This can result in significant errors in the fit, especially in the masked regions, and thus bias the measurement of the emission lines (Sarzi et al., 2006).

Thus, the method for extraction of gas kinematics was advanced by Sarzi et al. (2006) to measure emission lines without spectral masking. "The key ingredient is to treat the emission lines as additional Gaussian templates and, while iteratively searching for their best velocities and velocity dispersions, to solve linearly at each step for their amplitudes and the optimal combination of the stellar templates, which are convolved by the best stellar line-of-sight velocity distribution (LOSVD). In this way both the stellar continuum and the emission lines are fitted simultaneously." (Sarzi et al., 2006). This algorithm is implemented in the code GANDALF which is used in this pipeline.

B.5. Stellar Populations

In order to reconstruct the stellar population properties, we also make use of the PPXF routine by Cappellari and Emsellem (2004) and Cappellari (2017). For the extraction of stellar kinematics with PPXF, as described in Sect. B.3, the selection of spectral templates does not play an important role, as long as the templates do properly reproduce the observed spectra. This is due to the fact, that the information about the stellar kinematics is encoded in the convolution of spectrum with the LOSVD. However, a physically justified selection of spectral templates is a crucial factor for the reconstruction of the stellar population properties, as the entire relevant parameter space in age, metallicity and α-enhancement is only sampled by these spectral templates. For instance, star formation histories can be yield by reducing this parameter space to the age dimension.

Unfortunately, there is a strong degeneracy between age and metallicity within this parameter space. This problem is numerically described and implemented in PPXF through the equation

$$G_{\mathrm{mod}}(\lambda) = \int_{t=0}^{t=T} \mathrm{SSP}_\lambda(t, Z) \cdot \mathrm{SFR}(\mathrm{T} - \mathrm{t}) dt \qquad (\mathrm{B.2})$$

with the Single Stellar Population spectrum per unit mass SSP_λ, star formation rate SFR, age t, metallicity Z, and the age of the Universe T. I highlight that this equation is in PPXF also generalized to other relevant parameters, such as e.g. metallicity and α-enhancement (see Cappellari, 2017, and references therein).

In fact, equation B.2 describes an ill-conditioned inverse problem (e.g. Press et al., 2007). This implies that small variations in the input data are able to cause substantial variations the obtained solution. In other words, due to the existent degeneracy, it is not possible to obtain a unique solution without making further assumptions. (Cappellari, 2017)

A common mathematical technique to deal with this problem is regularization (e.g. Tikhonov and Arsenin, 1977; Hansen, 1998). This can be interpreted as the attenuation of high-frequency variations in the solution, beside those that are required by the input data. Thus, the regularization technique chooses the smoothest combination of stellar templates amongst all those combinations that are consistent with the data. I further highlight that the solution can be as irregular as necessary, as smoothness of the solution is not an assumption here (Cappellari, 2017).

B.6. Other Code Features and Future Development

In addition to the extraction of stellar and gas kinematics, as well as stellar population properties the pipeline provides further useful features. As already discussed in Sect. B.2, the pipeline executes all necessary preparatory steps. Thus, the only step that needs to be performed externally is the reduction of the data itself. I further highlight, that the pipeline is capable to analyse data from any given IFU instrument, if a appropriate read-in routine is provided. Eventually, the pipeline produces all available output products, including publication quality plots of the maps.

Runtime critical parts of the code, in particular the execution of ppxf and Gandalf, are parallelised. This is important as state-of-the-art IFU instruments provide a large number of spectra per pointing. For instance, the MUSE instrument provides approximately 90 000 spectra per pointing so that a typical TIMER observation contains 100 000 to 200 000 spectra.

Moreover, the code is equipped with an advanced data visualization tool (see Fig. B.1). The visualization tool has a graphical user interface and allows easy access to the output data. Maps of the extracted information can be displayed and by clicking on a particular bin in the map the tool displays the corresponding observed spectra and the relevant fits. This way a sanity-check of the procedures is possible. Further features, such as a plot of the star formation history will be implemented soon.

In fact, this pipeline is intended for use in multiple international collaborations, such as e.g. the TIMER project (see Gadotti et al., 2018) as well as the WEAVE-Apertif project (PI: Jesús Falcón-Barroso). In this context, the pipeline will be object of continuous development.
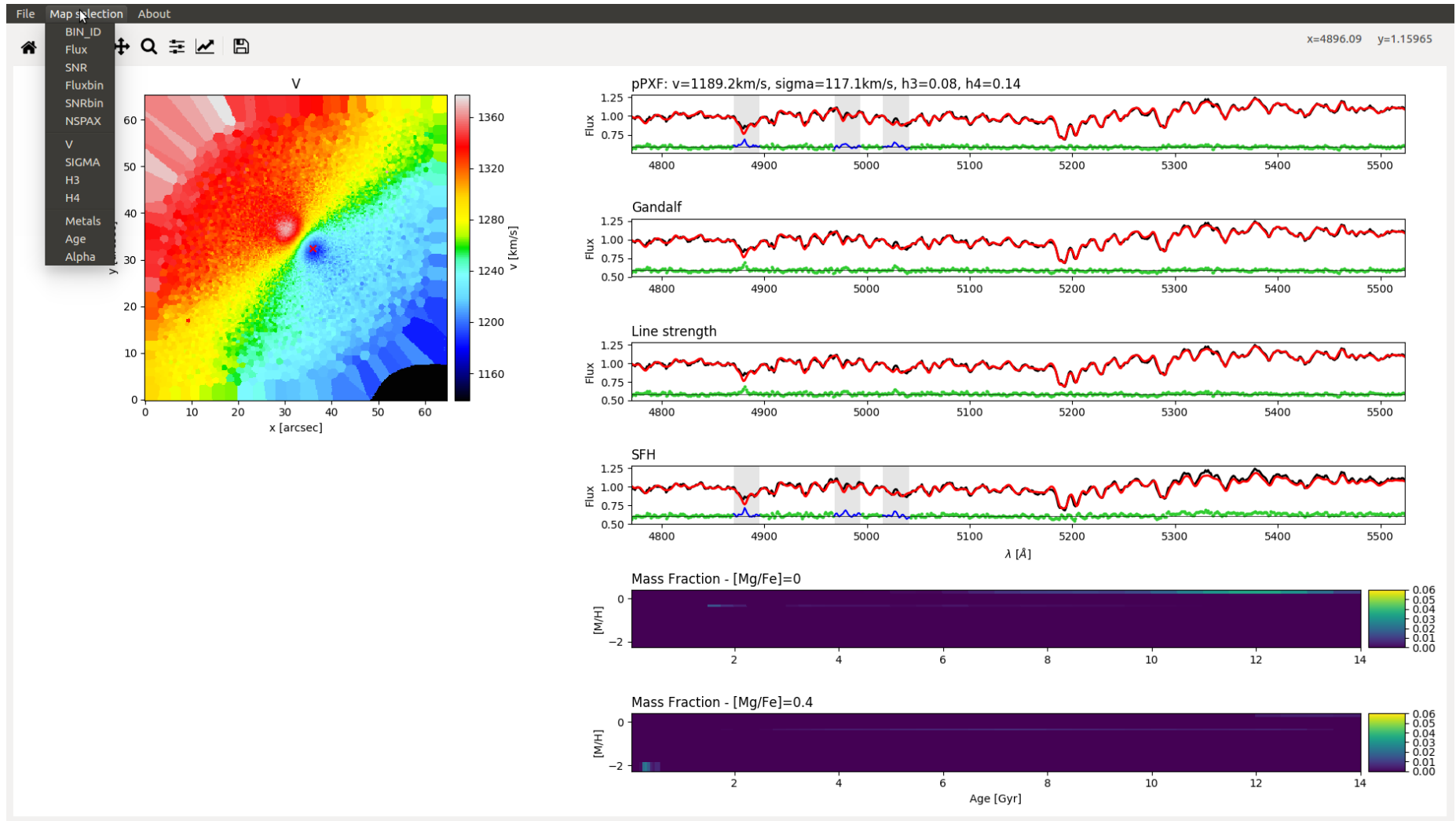
Figure B.1.: Screenshot of the visualization tool of the pipeline.

Bibliography

Athanassoula, E.: 1984, Phys. Rep. **114**, 319

Bacon, R., Accardo, M., Adjali, L., Anwand, H., Bauer, S., Biswas, I., Blaizot, J., Boudon, D., Brau-Nogue, S., Brinchmann, J., Caillier, P., Capoani, L., Carollo, C. M., Contini, T., Couderc, P., Daguisé, E., Deiries, S., Delabre, B., Dreizler, S., Dubois, J., Dupieux, M., Dupuy, C., Emsellem, E., Fechner, T., Fleischmann, A., François, M., Gallou, G., Gharsa, T., Glindemann, A., Gojak, D., Guiderdoni, B., Hansali, G., Hahn, T., Jarno, A., Kelz, A., Koehler, C., Kosmalski, J., Laurent, F., Le Floch, M., Lilly, S. J., Lizon, J.-L., Loupias, M., Manescau, A., Monstein, C., Nicklas, H., Olaya, J.-C., Pares, L., Pasquini, L., Pécontal-Rousset, A., Pelló, R., Petit, C., Popow, E., Reiss, R., Remillieux, A., Renault, E., Roth, M., Rupprecht, G., Serre, D., Schaye, J., Soucail, G., Steinmetz, M., Streicher, O., Stuik, R., Valentin, H., Vernet, J., Weilbacher, P., Wisotzki, L., and Yerle, N.: 2010, in *Ground-based and Airborne Instrumentation for Astronomy III*, Vol. 7735 of Proc. SPIE, p. 773508

Bacon, R., Adam, G., Baranne, A., Courtes, G., Dubet, D., Dubois, J. P., Emsellem, E., Ferruit, P., Georgelin, Y., Monnet, G., Pecontal, E., Rousset, A., and Say, F.: 1995, A&AS **113**, 347

Bacon, R., Copin, Y., Monnet, G., Miller, B. W., Allington-Smith, J. R., Bureau, M., Carollo, C. M., Davies, R. L., Emsellem, E., Kuntschner, H., Peletier, R. F., Verolme, E. K., and de Zeeuw, P. T.: 2001, MNRAS **326**, 23

Bender, R., Saglia, R. P., and Gerhard, O. E.: 1994, MNRAS **269**, 785

Binney, J. and Tremaine, S.: 2008, *Galactic Dynamics: Second Edition*, Princeton University Press

Bittner, A., Gadotti, D. A., Elmegreen, B. G., Athanassoula, E., Elmegreen, D. M., Bosma, A., and Muñoz-Mateos, J.-C.: 2017, MNRAS **471**, 1070

Bondi, H.: 1952, MNRAS **112**, 195

Booth, C. M. and Schaye, J.: 2009, MNRAS **398**, 53

Bundy, K., Bershady, M. A., Law, D. R., Yan, R., Drory, N., MacDonald, N., Wake, D. A., Cherinka, B., Sánchez-Gallego, J. R., Weijmans, A.-M., Thomas,

D., Tremonti, C., Masters, K., Coccato, L., Diamond-Stanic, A. M., Aragón-Salamanca, A., Avila-Reese, V., Badenes, C., Falcón-Barroso, J., Belfiore, F., Bizyaev, D., Blanc, G. A., Bland-Hawthorn, J., Blanton, M. R., Brownstein, J. R., Byler, N., Cappellari, M., Conroy, C., Dutton, A. A., Emsellem, E., Etherington, J., Frinchaboy, P. M., Fu, H., Gunn, J. E., Harding, P., Johnston, E. J., Kauffmann, G., Kinemuchi, K., Klaene, M. A., Knapen, J. H., Leauthaud, A., Li, C., Lin, L., Maiolino, R., Malanushenko, V., Malanushenko, E., Mao, S., Maraston, C., McDermid, R. M., Merrifield, M. R., Nichol, R. C., Oravetz, D., Pan, K., Parejko, J. K., Sanchez, S. F., Schlegel, D., Simmons, A., Steele, O., Steinmetz, M., Thanjavur, K., Thompson, B. A., Tinker, J. L., van den Bosch, R. C. E., Westfall, K. B., Wilkinson, D., Wright, S., Xiao, T., and Zhang, K.: 2015, ApJ **798**, 7

Buta, R. J.: 2013, *Galaxy Morphology*, p. 155

Buta, R. J., Sheth, K., Athanassoula, E., Bosma, A., Knapen, J. H., Laurikainen, E., Salo, H., Elmegreen, D., Ho, L. C., Zaritsky, D., Courtois, H., Hinz, J. L., Muñoz-Mateos, J.-C., Kim, T., Regan, M. W., Gadotti, D. A., Gil de Paz, A., Laine, J., Menéndez-Delmestre, K., Comerón, S., Erroz Ferrer, S., Seibert, M., Mizusawa, T., Holwerda, B., and Madore, B. F.: 2015, ApJS **217**, 32

Cappellari, M.: 2017, MNRAS **466**, 798

Cappellari, M. and Copin, Y.: 2003, MNRAS **342**, 345

Cappellari, M. and Emsellem, E.: 2004, PASP **116**, 138

Cappellari, M., Emsellem, E., Krajnović, D., McDermid, R. M., Scott, N., Verdoes Kleijn, G. A., Young, L. M., Alatalo, K., Bacon, R., Blitz, L., Bois, M., Bournaud, F., Bureau, M., Davies, R. L., Davis, T. A., de Zeeuw, P. T., Duc, P.-A., Khochfar, S., Kuntschner, H., Lablanche, P.-Y., Morganti, R., Naab, T., Oosterloo, T., Sarzi, M., Serra, P., and Weijmans, A.-M.: 2011, MNRAS **413**, 813

Choi, E., Ostriker, J. P., Naab, T., and Johansson, P. H.: 2012, ApJ **754**, 125

Churazov, E., Sazonov, S., Sunyaev, R., Forman, W., Jones, C., and Böhringer, H.: 2005, MNRAS **363**, L91

Dalcanton, J. J., Spergel, D. N., Gunn, J. E., Schmidt, M., and Schneider, D. P.: 1997, AJ **114**, 635

de Zeeuw, P. T., Bureau, M., Emsellem, E., Bacon, R., Carollo, C. M., Copin, Y., Davies, R. L., Kuntschner, H., Miller, B. W., Monnet, G., Peletier, R. F., and Verolme, E. K.: 2002, MNRAS **329**, 513

Dehnen, W. and Aly, H.: 2012, MNRAS **425**, 1068

Dobbs, C. and Baba, J.: 2014, PASA **31**, e035

Dolag, K., Borgani, S., Murante, G., and Springel, V.: 2009, MNRAS **399**, 497

Dolag, K., Borgani, S., Schindler, S., Diaferio, A., and Bykov, A. M.: 2008, Space Sci. Rev. **134**, 229

Dolag, K., Jubelgas, M., Springel, V., Borgani, S., and Rasia, E.: 2004, ApJ **606**, L97

Dolag, K., Vazza, F., Brunetti, G., and Tormen, G.: 2005, MNRAS **364**, 753

Donnert, J., Dolag, K., Brunetti, G., and Cassano, R.: 2013, MNRAS **429**, 3564

Elmegreen, D. M. and Elmegreen, B. G.: 1984, ApJS **54**, 127

Elmegreen, D. M., Elmegreen, B. G., and Dressler, A.: 1982, MNRAS **201**, 1035

Elmegreen, D. M., Elmegreen, B. G., Yau, A., Athanassoula, E., Bosma, A., Buta, R. J., Helou, G., Ho, L. C., Gadotti, D. A., Knapen, J. H., Laurikainen, E., Madore, B. F., Masters, K. L., Meidt, S. E., Menéndez-Delmestre, K., Regan, M. W., Salo, H., Sheth, K., Zaritsky, D., Aravena, M., Skibba, R., Hinz, J. L., Laine, J., Gil de Paz, A., Muñoz-Mateos, J.-C., Seibert, M., Mizusawa, T., Kim, T., and Erroz Ferrer, S.: 2011, ApJ **737**, 32

Elvis, M., Wilkes, B. J., McDowell, J. C., Green, R. F., Bechtold, J., Willner, S. P., Oey, M. S., Polomski, E., and Cutri, R.: 1994, ApJS **95**, 1

Emsellem, E., Cappellari, M., Krajnović, D., van de Ven, G., Bacon, R., Bureau, M., Davies, R. L., de Zeeuw, P. T., Falcón-Barroso, J., Kuntschner, H., McDermid, R., Peletier, R. F., and Sarzi, M.: 2007, MNRAS **379**, 401

Emsellem, E., Cappellari, M., Peletier, R. F., McDermid, R. M., Bacon, R., Bureau, M., Copin, Y., Davies, R. L., Krajnović, D., Kuntschner, H., Miller, B. W., and de Zeeuw, P. T.: 2004, MNRAS **352**, 721

Emsellem, E., Krajnović, D., and Sarzi, M.: 2014, MNRAS **445**, L79

Fabian, A. C., Sanders, J. S., Allen, S. W., Crawford, C. S., Iwasawa, K., Johnstone, R. M., Schmidt, R. W., and Taylor, G. B.: 2003, MNRAS **344**, L43

Fabjan, D., Borgani, S., Tornatore, L., Saro, A., Murante, G., and Dolag, K.: 2010, MNRAS **401**, 1670

Falcón-Barroso, J., Bacon, R., Bureau, M., Cappellari, M., Davies, R. L., de Zeeuw, P. T., Emsellem, E., Fathi, K., Krajnović, D., Kuntschner, H., McDermid, R. M., Peletier, R. F., and Sarzi, M.: 2006, MNRAS **369**, 529

Falcón-Barroso, J., Lyubenova, M., van de Ven, G., Mendez-Abreu, J., Aguerri, J. A. L., García-Lorenzo, B., Bekeraité, S., Sánchez, S. F., Husemann, B., García-Benito, R., Mast, D., Walcher, C. J., Zibetti, S., Barrera-Ballesteros, J. K., Galbany, L., Sánchez-Blázquez, P., Singh, R., van den Bosch, R. C. E., Wild, V., Zhu, L., Bland-Hawthorn, J., Cid Fernandes, R., de Lorenzo-Cáceres, A., Gallazzi, A., González Delgado, R. M., Marino, R. A., Márquez, I., Pérez, E., Pérez, I., Roth, M. M., Rosales-Ortega, F. F., Ruiz-Lara, T., Wisotzki, L., Ziegler, B., and Califa Collaboration: 2017, A&A **597**, A48

Fall, S. M. and Efstathiou, G.: 1980, MNRAS **193**, 189

Gadotti, D. A. and de Souza, R. E.: 2005, ApJ **629**, 797

Gadotti, D. A., Seidel, M. K., Sánchez-Blázquez, P., Falcón-Barroso, J., Husemann, B., Coelho, P., and Pérez, I.: 2015, A&A **584**, A90

Ganda, K., Falcón-Barroso, J., Peletier, R. F., Cappellari, M., Emsellem, E., Mc-Dermid, R. M., de Zeeuw, P. T., and Carollo, C. M.: 2006, MNRAS **367**, 46

Gerhard, O. E.: 1993, MNRAS **265**, 213

Hansen, P. C.: 1998, *Rank-deficient and discrete ill-posed problems: numerical aspects of linear inversion*, Vol. 4, Mathematical Modeling and Computation, Siam, Philadelphia

Hirschmann, M., Dolag, K., Saro, A., Bachmann, L., Borgani, S., and Burkert, A.: 2014, MNRAS **442**, 2304

Hubble, E. P.: 1926a, ApJ 63

Hubble, E. P.: 1926b, ApJ 64

Hubble, E. P.: 1927, *The Observatory* **50**, 276

Hubble, E. P.: 1929, ApJ 69

Kaiser, C. R. and Binney, J.: 2003, MNRAS **338**, 837

Kuntschner, H., Emsellem, E., Bacon, R., Cappellari, M., Davies, R. L., de Zeeuw, P. T., Falcón-Barroso, J., Krajnović, D., McDermid, R. M., Peletier, R. F., Sarzi, M., Shapiro, K. L., van den Bosch, R. C. E., and van de Ven, G.: 2010, MNRAS **408**, 97

Lange, R., Driver, S. P., Robotham, A. S. G., Kelvin, L. S., Graham, A. W., Alpaslan, M., Andrews, S. K., Baldry, I. K., Bamford, S., Bland-Hawthorn, J., Brough, S., Cluver, M. E., Conselice, C. J., Davies, L. J. M., Haeussler, B., Konstantopoulos, I. S., Loveday, J., Moffett, A. J., Norberg, P., Phillipps, S.,

Taylor, E. N., López-Sánchez, Á. R., and Wilkins, S. M.: 2015, MNRAS **447**, 2603

Lin, C. C. and Shu, F. H.: 1964, ApJ **140**, 646

Lindblad, B.: 1959, *Handbuch der Physik* **53**, 21

McConnell, N. J. and Ma, C.-P.: 2013, ApJ **764**, 184

McMillan, P. J.: 2011, MNRAS **414**, 2446

Mezcua, M. and Prieto, M. A.: 2014, ApJ **787**, 62

Mo, H. J., Mao, S., and White, S. D. M.: 1998, MNRAS **295**, 319

Monaghan, J. J.: 1992, ARA&A **30**, 543

Narayan, R. and Quataert, E.: 2005, *Science* **307**, 77

Obreschkow, D. and Glazebrook, K.: 2014, ApJ **784**, 26

Peebles, P. J. E.: 1969, ApJ **155**, 393

Peebles, P. J. E.: 1971, A&A **11**, 377

Peletier, R. F., Falcón-Barroso, J., Bacon, R., Cappellari, M., Davies, R. L., de Zeeuw, P. T., Emsellem, E., Ganda, K., Krajnović, D., Kuntschner, H., McDermid, R. M., Sarzi, M., and van de Ven, G.: 2007, MNRAS **379**, 445

Press, W. H., Teukolsky, S. A., Vetterling, W. T., and Flannery, B. P.: 2007, *Numerical recipes: The art of scientific computing*, Cambridge Univ. Press, Cambridge, 3rd edition

Price, D. J.: 2012, *Journal of Computational Physics* **231**, 759

Prieto, M. A., Reunanen, J., Tristram, K. R. W., Neumayer, N., Fernandez-Ontiveros, J. A., Orienti, M., and Meisenheimer, K.: 2010, MNRAS **402**, 724

Romanowsky, A. J. and Fall, S. M.: 2012, ApJS **203**, 17

Rosse, T. E. O.: 1850, *Philosophical Transactions of the Royal Society of London Series I* **140**, 499

Russell, H. R., McNamara, B. R., Edge, A. C., Hogan, M. T., Main, R. A., and Vantyghem, A. N.: 2013, MNRAS **432**, 530

Saha, K. and Elmegreen, B.: 2016, ApJ **826**, L21

Sánchez, S. F., Kennicutt, R. C., Gil de Paz, A., van de Ven, G., Vílchez, J. M., Wisotzki, L., Walcher, C. J., Mast, D., Aguerri, J. A. L., Albiol-Pérez, S., Alonso-Herrero, A., Alves, J., Bakos, J., Bartáková, T., Bland-Hawthorn, J., Boselli, A., Bomans, D. J., Castillo-Morales, A., Cortijo-Ferrero, C., de Lorenzo-Cáceres, A., Del Olmo, A., Dettmar, R.-J., Díaz, A., Ellis, S., Falcón-Barroso, J., Flores, H., Gallazzi, A., García-Lorenzo, B., González Delgado, R., Gruel, N., Haines, T., Hao, C., Husemann, B., Iglésias-Páramo, J., Jahnke, K., Johnson, B., Jungwiert, B., Kalinova, V., Kehrig, C., Kupko, D., López-Sánchez, Á. R., Lyubenova, M., Marino, R. A., Mármol-Queraltó, E., Márquez, I., Masegosa, J., Meidt, S., Mendez-Abreu, J., Monreal-Ibero, A., Montijo, C., Mourão, A. M., Palacios-Navarro, G., Papaderos, P., Pasquali, A., Peletier, R., Pérez, E., Pérez, I., Quirrenbach, A., Relaño, M., Rosales-Ortega, F. F., Roth, M. M., Ruiz-Lara, T., Sánchez-Blázquez, P., Sengupta, C., Singh, R., Stanishev, V., Trager, S. C., Vazdekis, A., Viironen, K., Wild, V., Zibetti, S., and Ziegler, B.: 2012, A&A **538**, A8

Sarzi, M., Falcón-Barroso, J., Davies, R. L., Bacon, R., Bureau, M., Cappellari, M., de Zeeuw, P. T., Emsellem, E., Fathi, K., Krajnović, D., Kuntschner, H., McDermid, R. M., and Peletier, R. F.: 2006, MNRAS **366**, 1151

Schlachtberger, D. P.: 2014, *Master's thesis*, Ludwig-Maximilians-Universität München

Sheth, K., Regan, M., Hinz, J. L., Gil de Paz, A., Menéndez-Delmestre, K., Muñoz-Mateos, J.-C., Seibert, M., Kim, T., Laurikainen, E., Salo, H., Gadotti, D. A., Laine, J., Mizusawa, T., Armus, L., Athanassoula, E., Bosma, A., Buta, R. J., Capak, P., Jarrett, T. H., Elmegreen, D. M., Elmegreen, B. G., Knapen, J. H., Koda, J., Helou, G., Ho, L. C., Madore, B. F., Masters, K. L., Mobasher, B., Ogle, P., Peng, C. Y., Schinnerer, E., Surace, J. A., Zaritsky, D., Comerón, S., de Swardt, B., Meidt, S. E., Kasliwal, M., and Aravena, M.: 2010, PASP **122**, 1397

Shima, E., Matsuda, T., Takeda, H., and Sawada, K.: 1985, MNRAS **217**, 367

Springel, V.: 2005, MNRAS **364**, 1105

Springel, V. and Hernquist, L.: 2002, MNRAS **333**, 649

Springel, V. and Hernquist, L.: 2003, MNRAS **339**, 289

Springel, V., Yoshida, N., and White, S. D. M.: 2001, New A **6**, 79

Steinborn, L. K., Dolag, K., Hirschmann, M., Prieto, M. A., and Remus, R.-S.: 2015, MNRAS **448**, 1504

Teklu, A. F., Remus, R.-S., Dolag, K., Beck, A. M., Burkert, A., Schmidt, A. S., Schulze, F., and Steinborn, L. K.: 2015, ApJ **812**, 29

Teyssier, R.: 2002, A&A **385**, 337

Tikhonov, A. N. and Arsenin, V. Y.: 1977, *Solutions of ill-posed problems*, Wiley, New York

Toomre, A.: 1969, ApJ **158**, 899

Tormen, G., Bouchet, F. R., and White, S. D. M.: 1997, MNRAS **286**, 865

Tornatore, L., Borgani, S., Dolag, K., and Matteucci, F.: 2007, MNRAS **382**, 1050

Tornatore, L., Borgani, S., Springel, V., Matteucci, F., Menci, N., and Murante, G.: 2003, MNRAS **342**, 1025

van der Marel, R. P. and Franx, M.: 1993, ApJ **407**, 525

van der Wel, A., Franx, M., van Dokkum, P. G., Skelton, R. E., Momcheva, I. G., Whitaker, K. E., Brammer, G. B., Bell, E. F., Rix, H.-W., Wuyts, S., Ferguson, H. C., Holden, B. P., Barro, G., Koekemoer, A. M., Chang, Y.-Y., McGrath, E. J., Häussler, B., Dekel, A., Behroozi, P., Fumagalli, M., Leja, J., Lundgren, B. F., Maseda, M. V., Nelson, E. J., Wake, D. A., Patel, S. G., Labbé, I., Faber, S. M., Grogin, N. A., and Kocevski, D. D.: 2014, ApJ **788**, 28

Vazdekis, A., Sánchez-Blázquez, P., Falcón-Barroso, J., Cenarro, A. J., Beasley, M. A., Cardiel, N., Gorgas, J., and Peletier, R. F.: 2010, MNRAS **404**, 1639

Vogelsberger, M., Genel, S., Sijacki, D., Torrey, P., Springel, V., and Hernquist, L.: 2013, MNRAS **436**, 3031

Wiersma, R. P. C., Schaye, J., and Smith, B. D.: 2009, MNRAS **393**, 99

Acknowledgements

First of all, I wish to wholeheartedly thank my supervisor Klaus Dolag for offering me this project, for all his help with the code, his patience, countless discussions and the good coffee. Thanks for always having time for my questions. This thesis would not have been possible without you!

I also want to thank Andreas Burkert and Rhea-Silvia Remus for their support, many fruitful discussions and all the input throughout the time of my thesis work. I always enjoyed working with you.

Many thanks to Lisa Steinborn for her help with the black hole model, for explaining it to me and putting a lot of effort into changing the implementations. Furthermore, thanks to all my fellow students for the enjoyable time in the group.

Special thanks also to Stephan Ströbl, especially for never being teetotal!!

Finally, I would like to thank my family for their support, help, advice and everything throughout the last 24 years.

Erklärung

Hiermit erkläre ich, die vorliegende Arbeit selbständig verfasst zu haben und keine anderen als die in der Arbeit angegebenen Quellen und Hilfsmittel benutzt zu haben.

_____

Adrian Bittner
München, 09. März 2018